

THE COSMIC VELOCITY FIELD
– LOCAL VARIATIONS IN THE
HUBBLE CONSTANT AND THE
POWER SPECTRUM FROM
FUTURE SKY SURVEYS

PHD THESIS

IO SANDBERG HESS ODDERSKOV

SEPTEMBER 2016

DEPARTMENT OF PHYSICS AND ASTRONOMY
AARHUS UNIVERSITY

This thesis is submitted to the Faculty of Science at Aarhus University, Denmark, in order to fulfill the requirements for obtaining the PhD degree in Physics.

The studies have been carried out under the supervision of Prof. Steen Hannestad in the Cosmology Group at the Department of Physics and Astronomy at Aarhus University from September 2012 to September 2016.

Layout and typography by Io Odderskov with L^AT_EX. Figures are made in Inkscape, MATLAB, and matplotlib.

© Io Odderskov 2016

io.odderskov@gmail.com

Preface and acknowledgements

This report presents the research that I have been engaged in during my PhD studies. Most of the first year was spent reading about the genus statistic of large scale structure of the Universe. However, this topic was set aside in 2013, when the Planck collaboration published the results from an analysis of the most precise measurements ever obtained of the cosmic microwave background. Their analysis gave a value for the Hubble parameter significantly lower than the one found by direct measurements in our local universe. This inspired us to investigate how much the local Hubble constant could be expected to vary as a consequence of the ongoing processes of structure formation. The first part of this research was carried out in collaboration with Steen Hannestad and Troels Haugbølle, and the results appear in [1].

Shortly after finishing this, I went to Heidelberg for a research stay in the group of Luca Amendola at the University of Heidelberg. Here, I conducted a study in collaboration with Luca Amendola and Marco Baldi from the University of Bologna, regarding the additional variance in the Hubble parameter that arises in models of interacting dark energy, also including a test of the corrections that can be made by using linear perturbation theory. The results of this study were presented in [2].

After returning from Heidelberg, yet another study of these effects was carried out, this time in collaboration with Sofie Kocsbang, regarding the effect of the peculiar velocities on the luminosity distances used for the determination of the Hubble constant. The results were presented in [3].

Meanwhile, another project was initiated, regarding the possibility for using the peculiar velocities obtained from observations of type Ia supernovae as a probe of cosmological parameters. Our first objective was to assess how well the velocity field obtained from the supernovae can be described by expanding in spherical harmonics, despite the fact that we cannot measure the field at every point of the sky – partly because of the geometry of upcoming sky surveys, and partly because of the distribution of supernovae in the universe. The results of this study has been submitted to JCAP, and can be found on arXiv at [4].

I would like to thank Steen Hannestad and Luca Amendola for their guidance, for creating great research environments, and for their flexibility in letting their students try out their own ideas and work in whatever way suits them best. I am also grateful to Troels Haugbølle, Marco Baldi, and Sofie Kocsbang, for their efforts and thoroughness in our collaboration. I would like to thank the large group of cosmologists at Heidelberg University for making me feel as part of the group. Furthermore, I would like to thank Thomas Tram and Christian Schultz for help with

numerical tools, Brigitte Henderson for help with practical stuff, and Maria Archidiacono, Tobias Basse, Ole Bjælde, Jacob Brandbyge, Jeppe Dakin, Ian Hamann, Sofie Kocsbang, Rasmus Sloth Lundkvist, and Yvonne Wong for company during trips, schools and conferences, as well as many nice dinners and coffee breaks.

Thank you to my friends for great company at home, during lunch breaks, workouts, and trips abroad, and for being there when I really needed you. And lastly, thank you to Poul, Zeth, Per, Maria, Kirstine, and Hans for your great support – technical and moral – during the last four years.

Io Odderskov, September 2016

- [1] Io Odderskov, Steen Hannestad, and Troels Haugbølle, *On the local variation of the Hubble constant*, JCAP **2014** 10 028.
- [2] Io Odderskov, Marco Baldi, and Luca Amendola, *The effect of interacting dark energy on local measurements of the Hubble constant*, JCAP **2016** 05 035.
- [3] Io Odderskov, Sofie Kocsbang, and Steen Hannestad, *The local value of H_0 in an inhomogeneous universe*, JCAP **2016** 02 001.
- [4] Io Odderskov and Steen Hannestad, *Measuring the velocity field from type Ia supernovae in an LSST-like sky survey*, e-print arXiv:1608.04446.
Submitted to JCAP.

Summary

Nearly a hundred years ago, observations started to show that almost all the galaxies we can see are moving away from us. This was interpreted as evidence that the universe is expanding, a discovery supporting the theory that it had originated in what came to be known as a *Big Bang*. The violent birth of the universe left a trace in the form of heat radiation, which is measured with exquisite precision today, allowing for an extremely precise determination of the initial conditions of the universe.

Meanwhile, ongoing observations of galaxies are improving our knowledge of the later stages of the history of the universe. A specific kind of star explosions – type Ia supernovae – enables precise measurements of the distances and velocities of distant galaxies. This makes it possible to obtain precise constraints on the present day conditions of the universe.

Recently, the predictions for the expansion rate of the universe from the initial conditions have begun to come into conflict with the actual rate measured in the local universe. This conflict is one of the main subjects of this thesis. The gravitational attraction of small overdensities in the early universe caused matter to fall towards them; this is the process responsible for forming all the galaxies, clusters, and super clusters of galaxies we see in the universe, and it is still going on today. The motion of matter generated by this process is called *peculiar* motion, and it is a source of uncertainty in local measurements of the expansion rate of the universe. How large this uncertainty is is the subject of three studies presented in this thesis, in which we have used computer simulations to imitate the formation of structure in the universe, and analyzed the observations that could be carried out by imaginary observers spread out through the simulations.

Measurements of the peculiar velocities also carry the possibility for constraining cosmological parameters, a crucial ingredient in identifying the best cosmological model for our universe. A great candidate for measuring the peculiar velocities of galaxies are the type Ia supernovae, which will be measured in large quantities in upcoming sky surveys. The second major topic for this thesis is the determination of how well the peculiar velocity field of the local universe can be measured in the imminent survey with the *Large Synoptic Sky Telescope*, in spite of large unobserved parts of the sky and regions in which no supernovae happen to occur. Again the studies are based on simulations of the structures in the universe, but this time we have used semi-analytical methods to follow the processes of galaxy and star formation within the simulations, to get realistic predictions for where in the cosmic web type Ia supernovae occur.

Resumé

For nær ved hundrede år siden begyndte observationer at vise, at næsten alle de galakser vi kan se bevæger sig væk fra os. Dette blev tolket som evidens for at universet udvider sig, en opdagelse der støtter teorien om universets begyndelse i et såkaldt *Big Bang*. Universets voldsomme fødsel efterlod et spor i form af varmemstråling, som i dag måles med udsøgt præcision, hvilket tillader en ekstremt præcis bestemmelse af universets begyndelsesbetingelser.

Sideløbende har observationer af galakser forbedret vores viden om de senere stadier af universets historie. En bestemt type stjerneeksplosioner – type Ia supernovaer – tillader præcise målinger af fjerne galaksers afstande og hastigheder. Dette muliggør nøjagtige bestemmelser af universets nuværende tilstand.

For nyligt er forudsigelser om universets udvidelseshastighed baseret på begyndelsesbetingelserne begyndt at komme i konflikt med den faktisk målte udvidelseshastighed i det lokale univers. Denne konflikt er et af de centrale emner for denne afhandling. Den gravitationelle tiltrækning af små overtyætheder i det tidlige univers resulterede i at stof faldt imod disse; det er denne proces, som stadig foregår, der har givet anledning til skabelsen af alle de galakser, hobe og superhobe af galakser vi ser i universet. Den bevægelse der skabes i denne proces kaldes *egenbevægelse*, og er en kilde til usikkerhed i de lokale målinger af universets udvidelseshastighed. Hvor stor denne usikkerhed er, er emnet for tre studier præsenteret i denne afhandling, hvor vi har anvendt computersimuleringer til at imitere strukturdannelsen i universet, og analyseret de observationer der kunne udføres af imaginære observatører spredt omkring i simuleringerne.

Målinger af egenhastigheder giver også mulighed for at bestemme kosmologiske parametre, en afgørende ingrediens i at identificere den bedste kosmologiske model for vores univers. En oplagt kandidat til målinger af galaksers egenhastigheder er type Ia supernovaer, som vil blive observeret i massevis i nært forestående projekter, der har til formål at kortlægge universet. Det andet centrale emne for denne afhandling er bestemmelsen af hvor godt egenhastighedsfeltet vil kunne måles med snarlige observationer foretaget med *Large Synoptic Sky Telescope* (LSST), på trods af store, uobserverede områder af himmelen og regioner hvor der tilfældigvis ikke optræder nogen supernovaer. Igen er studierne baseret på simuleringer af strukturer i universet, men denne gang har vi brugt semi-analytiske metoder til at følge galakse- og stjerne-dannelsesprocesser i simuleringerne, for at opnå realistiske forudsigelser for hvor i det kosmiske væv type Ia supernovaer forekommer.

Contents

Preface and acknowledgements	i
Summary	iii
Resumé	iv
Contents	v
1 Introduction	1
1.1 This thesis	2
I Formation and identification of structures in cosmology	4
2 The expanding universe	5
2.1 The Einstein equation	5
2.2 Time, space, and the cosmological principle	6
2.3 The Friedmann equation and the fluid equation	7
2.4 Hubble's law	8
2.5 Distances in a homogeneous and isotropic expanding universe	8
2.6 Redshifts and velocities in a homogeneous and isotropic expanding universe	11
2.6.1 Low z approximations	11
2.7 Distances and redshifts in an inhomogeneous universe	13
2.7.1 Peculiar velocity and measured redshift	13
2.7.2 Peculiar velocity and measured distance	14
3 Evolution of structure	16
3.1 The two point correlation function and the power spectrum	16
3.1.1 The variance of the density field and the amplitude of the power spectrum .	18
3.2 Inflation and the Harrison-Zel'dovich spectrum	19
3.3 Linear structure formation	20
3.3.1 Evolution of density perturbations	20

4	Non-linear structure formation: N-body simulations	25
4.1	CAMB	25
4.2	Initial Conditions	26
4.3	GADGET-2	26
4.3.1	The gravitational field	26
4.3.2	Time integration	27
4.3.3	Output	28
5	Characterisation of structure	29
5.1	Spherical collapse	29
5.2	ROCKSTAR	30
II	Local variations in the Hubble constant	33
6	The Hubble constant discrepancy	34
6.1	Measurements of the CMB: Analysis and results from the Planck collaboration	34
6.2	Measuring the expansion rate of the local universe	35
6.3	Studies of the local variation in the Hubble constant	36
7	On the local variation of the Hubble constant	38
7.1	Introduction	38
7.2	Method	39
7.2.1	Simulations	39
7.2.2	Identifying halos	40
7.3	Analysis	40
7.3.1	Objectives	41
7.4	Results	44
7.5	Discussion	49
8	The local value of H_0 in an inhomogeneous universe	51
8.1	Introduction	51
8.2	Method for computing redshift-distance relations in N-body simulations at low redshift	53
8.3	Mock observations	55
8.3.1	Redshift distribution of sources	55
8.3.2	Observers	57
8.3.3	Lightcone snapshots	57
8.3.4	Summary	58
8.4	Results and discussion	59
8.4.1	The local value of H_0 in an inhomogeneous universe based on observations in the redshift range $0.0233 < z < 0.15$	62
8.5	Summary	63

9	The effect of interacting dark energy on local measurements of the Hubble constant	64
9.1	Introduction	64
9.2	Coupled dark energy cosmologies	65
9.3	Simulations and halo catalogs	67
9.4	Method	68
9.5	Results and discussion	71
9.6	Conclusions	76
III	Realistic forecasts of SNe Ia observations for measurements of the peculiar velocity field	77
10	Imprints of the velocity field on type Ia supernova observations	78
10.1	The power spectrum of the peculiar velocity field	78
11	Semi-analytical galaxy formation	81
11.1	The two stages of galaxy formation	81
11.2	Stage 1: Merger trees	82
11.3	Stage 2: Galaxy formation	84
11.3.1	The basic scheme of Galacticus	84
11.3.2	Evolution of hot and cold gas	86
11.3.3	Star formation and feedback	88
11.3.4	Mergers	90
11.4	Summary	91
12	Type Ia supernovae	92
12.1	The progenitor problem	93
12.1.1	Single Degenerate ("SD") model	93
12.1.2	Double Degenerate ("DD") model	93
12.2	Type Ia supernovae in Galacticus	94
12.3	Star formation and the type Ia supernova rate	94
12.3.1	Predictions about the DTD	95
12.3.2	From star formation histories to supernova rates	95
12.3.3	The observed DTD	97
12.4	Construction of SNe Ia catalogs	98
13	Measuring the velocity field from type Ia supernovae in an LSST-like sky survey	100
13.1	Introduction	100
13.2	Mock supernova catalogs	101
13.2.1	Simulations	101

<i>CONTENTS</i>	viii
13.2.2 Mock galaxy and supernova catalogs	102
13.3 Mock observers and observations	105
13.4 The angular velocity power spectrum	107
13.4.1 Smoothing of the velocity field	109
13.4.2 Correcting for mode-coupling due to incomplete sky coverage	109
13.5 Results and discussion	112
13.6 Conclusions	118
IV Outlook and conclusions	119
14 Outlook and conclusions	120
14.1 Parameter forecast with the angular power spectrum of radial peculiar velocities .	120
14.2 Summary and conclusions	121
Bibliography	122

Chapter 1

Introduction

For many years, the heavens were seen as the place of the unchanging, eternal, and stable. The discoveries of Copernicus, Tycho Brahe, Galileo, Kepler, and Newton made it clear that the universe was neither perfect, unchanging, nor unearthly. But the most devastating blow to the illusion of a stable and eternal universe might have come with the theory of general relativity. When Einstein applied the equations of this theory to the entire universe in 1917, he realized that due to the gravity of matter, the universe would collapse. In order to restore a static universe, he famously introduced the cosmological constant, which would counter-balance the gravity of matter. However, within a few years it became clear that this balance was highly unstable. The best way to protect the universe against collapse was to have it rapidly expanding [5].

This hypothesis was confirmed by observations, when in the 1920s it was observed that the redshifts of galaxies were proportional to their distance, implying that they were all moving away from us. This suggested that several billion years ago, the universe had been in an extremely hot and dense state. Based on this theory, it was conjectured in the 1940s that the conditions of the early universe allowed nuclear synthesis of a few, light elements. Furthermore, the universe should be permeated by a trace of the heat radiation from its early, hot stages, which today would have cooled to a temperature of just a few degrees above the absolute zero [6, 7].

This background radiation was measured by Penzias and Wilson at Bell Labs in 1964 [8]. However, it was soon noted that this cosmic microwave background (CMB) looked suspiciously uniform, when considering that photons from opposite patches of the CMB are just reaching us now, and therefore have supposedly never been in contact with each other. A possible solution was proposed by Alan Guth in 1981 [9]: If a short time after its creation, the universe underwent a sudden, rapid expansion, regions which had previously been in contact with each other, and obtained a homogeneous temperature, would subsequently be separated, thereby explaining the homogeneity of the CMB. This early *inflation* would also, among other things, explain why the universe seems to be flat.

In addition to solving these problems, inflation was also expected to magnify small quantum fluctuations in the background, thereby creating inhomogeneities in the density of the early uni-

verse. And even though the expansion of space prevented the entire universe from collapsing under its gravity, the expansion was not sufficiently rapid to prevent the collapse of small, overdense regions. This was expected to account for the structures we see in the universe today such as galaxies, clusters, and super clusters. In the beginning of the 1990s, such inhomogeneities were observed by the COBE satellite [10] as small scale fluctuations in the temperature of the CMB.

The measured fluctuations were not large enough, though, to explain the rich structures we observe today, if the universe only contains the matter – such as galaxies, stars, and dust – that is visible to our telescopes. Luckily, another substance, which does not interact with light, had been discovered in galaxies and galaxy clusters by Zwicky in the 1930s [11]. The large amounts of this *dark matter* and its indifference to light allowed it to cluster in the early universe, in contrast to the visible matter, which was being dragged along by the photons. Consequently, gravity wells to fall into were available to the visible matter, as soon as the photons loosened their tight grip, when the universe became cold enough for electrons and protons to form neutral atoms in the so-called *recombination* about 400 000 years after the Big Bang. In the 1990s, everything looked great for the *cold dark matter* (CDM) model of the universe.

Until 1998, when two different research groups measured the expansion rate of the distant universe, and from these observations deduced that the rate with which the universe is expanding accelerates [12–14]. Until then, the expansion had been assumed to be slowing down due to the gravitational pull of matter. The acceleration was most easily explained if there was some constituent of the universe which was not thinned by the expansion. This was exactly the property of the cosmological constant, Λ , that Einstein had introduced into the equations of general relativity in order to explain why the universe did not collapse. And so, the CDM model of the universe was replaced by our current best theory, Λ CDM.

1.1 This thesis

Despite its simplicity, the Λ CDM model continues to be impressively successful, even as more and more precise observations of the universe over many different scales and ages are being made. However, recently, a significant discrepancy has emerged between the local measurements of the expansion rate, and predictions for this rate based on observations of the CMB.

As mentioned above, structures grow as regions more dense than the average attract matter. This process gives rise to peculiar velocities, which make some places experience a smaller expansion rate than average, while other regions experience a larger expansion rate, as matter flows out of underdense regions. The imprint of the matter distribution on the velocities of galaxies can also be used as a means to measure the density and clumpiness of the matter. The variations of the expansion rate due to peculiar velocities, and the possibility for using the same velocities as a probe of cosmological parameters, are the two main subjects of this thesis.

In part I, simple models for the evolution of the universe as well as numerical tools for following this evolution are introduced: Chapter 2 introduces the background universe, and first order perturbation theory is presented in chapter 3. In the following chapters, some of the tools that have

been used for the research presented in this thesis are introduced, specifically, N-body simulations are introduced in chapter 4, and a code for identifying structures in these simulations in chapter 5.

In part II, the observational discrepancy between the Hubble constant determined in the local universe and the value predicted by observations of the CMB is presented in chapter 6. This is followed by the presentation of three studies we have carried out on this subject, in chapters 7, 8, and 9.

Chapter 10 in part III introduces the subject of the local velocity field as a probe of the matter distribution of the universe. We then introduce tools for creating realistic mock catalogs of type Ia supernovae: In chapter 11 we explain the theory behind semi-analytical models for galaxy formation and introduce a code based on these principles. In chapter 12, we present the theory for type Ia supernovae, and explain how the current knowledge is used to estimate the type Ia supernova rate in N-body simulations. Finally, in chapter 13 we present the results for the supernova distribution, and mock observations of the velocity field based on these results; this is a modified version of a recent paper we have written on this subject.

At last, chapter 14 in part IV briefly discusses our plans for carrying out a parameter forecast based on the angular velocity power spectrum measured from type Ia supernovae, before we summarize and conclude.

Part I

Formation and identification of structures in cosmology

Chapter 2

The expanding universe

The best description of how gravity works comes from the general theory of relativity, which replaced Newton's theory as the most complete description early in the 20th century. For most of the subjects covered in this thesis, however, relativistic effects are negligible. The biggest exception to this concerns the overall expansion of the universe, which is fundamentally relativistic in nature. In this chapter, we will introduce the equations governing the expansion of space, and explain how this affects the observables which are relevant for the studies presented in this thesis.

2.1 The Einstein equation

General relativity gives a geometric description of how the presence of energy produces curvature of space and time, and how this curvature in turn determines the movement of mass and energy moves [15]. The majority of the theory is contained in the Einstein equation, which expresses how the curvature of space-time is related to the energy-momentum tensor, $T_{\mu\nu}$, which contains information about the energy density, ρ , and pressure, P , in the universe. Space and time are described by the metric-tensor, $g_{\mu\nu}$, which dictates how to measure distances in a curved time-space, with μ and ν being indices that takes the values (t, x, y, z) , corresponding to the time and the three spatial dimensions of the universe. The Einstein equation contains ten independent components, one for each pair of the space-time coordinates. The strength of the coupling between the metric and the energy-momentum tensor is determined by the gravitational constant, $G = 6.67 \times 10^{-11} \text{ N/kg}^2/\text{m}^2$, which is familiar from Newtonian gravity. All this is contained in the Einstein equation,

$$R_{\mu\nu} - \frac{1}{2}g_{\mu\nu}R = 8\pi GT_{\mu\nu}. \quad (2.1)$$

The left hand side of this equation describes the curvature of space-time, through the metric as well as the Ricci tensor $R_{\mu\nu}$, which depends on the metric and its derivatives, and the Ricci scalar $R \equiv g^{\mu\nu}R_{\mu\nu}$. The right hand side describes the content of the universe through the energy-

momentum tensor, $T_{\mu\nu}$, which contain the energy-density, ρ , and pressure, P , of all the different types of mass and energy in the universe.

2.2 Time, space, and the cosmological principle

One of the fundamental differences between the theories of Newton and Einstein is that in Einstein's theory, gravity not only distorts the path of an object through space, but also the time measured along that path. Therefore, time is treated on an equal footing with space in the general theory of relativity. Thus, the metric that describes distances in general relativity includes a time component as well as the usual three space components.

When we are only concerned with the overall evolution of the universe, we can (to a good approximation) ignore the inhomogeneities arising from the clumping of matter, and a few fundamental assumptions allow us to write a very simple equation for the metric of space-time-distances. These fundamental assumptions can be thought of as a generalization of the Copernican principle: That there is nothing special about our place in the universe. In the context of cosmology, this is known as the *cosmological principle*, and it states that the universe is homogeneous and isotropic, i.e., all places and directions look the same. The metric for a universe obeying this principle is the Friedmann-Lemaître-Robertson-Walker (FLRW) metric. As required by the cosmological principle, it does not vary as a function of spatial coordinates, only as a function of time. The time dependence can be contained in a function $a(t)$, which is called the scale factor of the universe, and is set such that $a(t_0) = 1$ with t_0 being the present age of the universe. The space coordinates, (r, θ, ϕ) , are then so-called *comoving* coordinates, and they can be thought of as the coordinates measured on a coordinate system which expands with the universe as dictated by the function $a(t)$. Expressed in these coordinates, infinitesimal space-time distances, ds , can be calculated from infinitesimal distances in time, dt , and space, $(dr, d\theta, d\phi)$, as,

$$ds^2 = -c^2 dt^2 + a^2(t) \left[dr^2 + S_\kappa^2(r) (d\theta^2 + \sin^2 \theta d\phi^2) \right]. \quad (2.2)$$

S_κ is a function which depends on the overall curvature of the universe. There are three possibilities for this, which are labeled by the *curvature parameter* κ . κ can take on the values 0 or ± 1 , corresponding to a flat, positively, or negatively curved space. For a spatially flat universe, we have $S_\kappa = r$, and the metric can be written as

$$ds^2 = -c^2 dt^2 + a^2(t) \left[dr^2 + r^2 (d\theta^2 + \sin^2 \theta d\phi^2) \right]. \quad (2.3)$$

This metric specifies the quantities on the left hand side of the Einstein equation, 2.1 in a homogeneous on isotropic universe. By also considering the energy and momentum associated with the constituents of the universe, described by $T_{\mu\nu}$, a set of equations for how the homogeneous and isotropic universe evolves as a function of time can be derived.

2.3 The Friedmann equation and the fluid equation

The dominant substances in our universe are matter, radiation, and the cosmological constant, with energy densities described by ρ_m , ρ_r , and ρ_Λ , respectively. As the universe expands, matter gets diluted, radiation gets diluted and redshifted, and the density of the cosmological constant stays constant. This implies that the energy densities depend on the scale factor introduced in the last section as

$$\rho_m \propto a^{-3} \quad (2.4)$$

$$\rho_r \propto a^{-4} \quad (2.5)$$

$$\rho_\Lambda \propto a^0 = 1. \quad (2.6)$$

As a consequence of this, different substances dominate the overall energy density at different times, dividing the history of the universe into different regimes. At very early times, until $a_{rm} \sim 3 \times 10^{-4}$, the energy density of radiation dominated the total energy of the universe. At a_{rm} , matter came to dominate over radiation. And lately, around $a_{m\Lambda} \sim 0.7$, the cosmological constant began dominating.

By considering a universe containing substances with a total density of $\rho = \sum_{i=\{m,r,\Lambda\}} \rho_i$, Friedmann and Lemaître independently derived a set of equations describing how the evolution of the Universe is determined by its overall curvature and the density of its contents, i.e. mass, radiation, and dark energy [5]. By evaluating the time-time component of the Einstein equations, the evolution of the scale factor as a function of the energy density can be found [15] as

$$\left(\frac{\dot{a}}{a}\right)^2 = \frac{8\pi G}{3}\rho - \frac{\kappa}{a^2}. \quad (2.7)$$

The *critical density*, ρ_c is defined as the density that corresponds to a universe with no overall curvature ($\kappa = 0$). By defining the *Hubble parameter* $H \equiv \frac{\dot{a}}{a}$, which we will return to shortly, the critical density can be seen from equation 2.7 to be $\rho_c = \frac{3H^2}{8\pi G}$. One usually expresses densities as fractions of the critical density, using the density parameter, $\Omega = \frac{\rho}{\rho_c}$.

In order to give a full description of the evolution of a universe of known content, one more equation is needed, namely a conservation law for the energy contained in the universe. In Newtonian mechanics, energy density and pressure evolves according to the *fluid equations*, i.e. the continuity and Euler equation [15], which we will return to in chapter 3. In general relativity, this is generalized to the statement that the covariant derivative of the energy-momentum tensor is zero, covariant derivatives being the generalization of normal derivatives in a curved space-time. Evaluating this statement reveals the conservation law

$$\frac{\partial \rho}{\partial t} + 3\frac{\dot{a}}{a}[\rho + P] = 0. \quad (2.8)$$

Equation (2.7) is known as the Friedmann equation and equation (2.8) as the fluid equation. Together, they determine the evolution of the scale factor and density with time in a homogeneous and isotropic universe.

2.4 Hubble's law

From the perspective of an observer somewhere in the universe, the expansion of space means that he will see objects move away from him. And the further away the objects are, i.e. the more space there is between the observer and the observed object, the faster they will recede. In the case of observers on Earth, this observation was first presented by Edwin Hubble in 1929 [16]. By observing a class of pulsating stars, *Cepheids*, whose luminosity is proportional to their pulsation period [17], astronomers were able to determine the distances to a small number of galaxies. By comparing the spectra of the light received from these galaxies with known atomic spectra, the amount by which the wavelength of the light had been stretched, the *redshift*, could be measured, which allowed calculating the radial velocities of the galaxies. These observations showed a strong tendency for galaxies to recede, and based on the observations, Hubble presented "Hubble's law", which states that the recession velocity, v_r , of a given galaxy as a function of its distance, r , from us can be described as [5, 16]

$$v_r = H_0 r. \quad (2.9)$$

As we will see later, this turns out to be an approximation to a more complete description of the relationship between the recession velocities and redshifts of objects in an expanding universe. From the full expression, it follows that Hubble's "constant" actually varies with time, and that it is related to the scale factor and its time derivative, $\dot{a} = \frac{da}{dt}$, as $H(t) = \frac{\dot{a}}{a}$. By applying equations 2.4–2.6 to the Friedmann equation, 2.7, for a flat universe, it is found that

$$H = H_0 \sqrt{\frac{\Omega_r}{a^4} + \frac{\Omega_m}{a^3} + \Omega_\Lambda}, \quad (2.10)$$

where $H_0 = H(t_0)$ is Hubble's constant. Since radiation only contributes a minute part of the overall energy density in the universe today, this can safely be ignored, as will be done for most of this thesis.

2.5 Distances in a homogeneous and isotropic expanding universe

Speaking about distances in an expanding universe can be rather ambiguous [18]. Maybe the most intuitive distance measure is the **proper distance**, $d_p(t)$, which is the length of the spatial geodesic between two objects when the scale factor is held fixed at $a(t)$, i.e. the distance one would measure by stopping the expansion of the universe and measuring the distance with a measuring rod. The relation to the distance in comoving coordinates, the so-called **comoving distance**, r , which appear in the metric, is found by setting $dt = d\theta = d\phi = 0$ in the metric. This gives

$ds = a(t)dr$, and integrating this with respect to the radial comoving coordinate r one finds

$$d_p(t) = a(t) \cdot r. \quad (2.11)$$

Since $a(t_0) = 1$, the comoving distance to an object today is the same as its proper distance, $r = d_p(t_0)$.

The proper distance cannot be determined directly, as we can only observe a given object when the light the object emits have had time to reach us. Hence, each object in the universe is observed as it was at some earlier time, t_e , when it emitted the light we are receiving today. The wavelength of the light we receive from these objects carries information about when the light was emitted, since the amount by which the light has been redshifted, z , is determined by how much the universe has expanded while the light was traveling through the universe. If the light was emitted with wavelength λ_e , and is observed with wavelength λ_0 , the redshift is given by $z = (\lambda_0 - \lambda_e)/\lambda_e$. This is related to the scale factor at the time of emission, a_e , and the scale factor now (when the light is observed), $a_0 = 1$, as $z = (a_0 - a_e)/a_e = 1/a_e - 1$.

The proper distance to an object, which emitted light at time t_e that is being received at time t_0 , can be obtained by integrating the path that the light has traveled. Since light moves at speed c , the distance that it travels in a time interval dt is given by $c dt$. And since it is moving along a straight line, $d\theta = d\phi = 0$, so the distance is given in the comoving coordinates as $a(t)dr$. This means that along the path of the light, $ds = 0$ and $c^2 dt^2 = a(t)^2 dr^2$, and hence the proper distance can be calculated as

$$d_p(t_0) = a(t_0) \cdot r = c \int_{t_e}^{t_0} \frac{dt}{a(t)}. \quad (2.12)$$

By substitution, and using $H = \dot{a}/a$ and $a = 1/(1+z)$, this can be converted to an integral over a or z instead:

$$d_p(t_0) = c \int_{a_e}^1 \frac{da}{a^2 H(a)} = c \int_0^z \frac{dz}{H(z)}. \quad (2.13)$$

Hence, if we can measure the redshift of an object in an entirely homogeneous and isotropic universe, and we know exactly how much matter, radiation, and dark energy the universe contains so that we know how H evolves via equation 2.10, we can determine the proper distances to objects in the universe from this equation. However, it is difficult to learn about the contents of the universe without being able to measure distances. Therefore, we need some measure of distance that depends on something other than the redshift of light. In the next section, two such measures will be introduced, which can be measured if we know the size or brightness of an object.

The luminosity distance and the angular diameter distance

From everyday experience, we have a sense of the distance to a familiar object from how bright it is (see figure 2.1). This is measured by the flux, i.e. the number of photons we receive per unit time and per unit area, multiplied by the energy of each photon. In a flat and stationary universe,

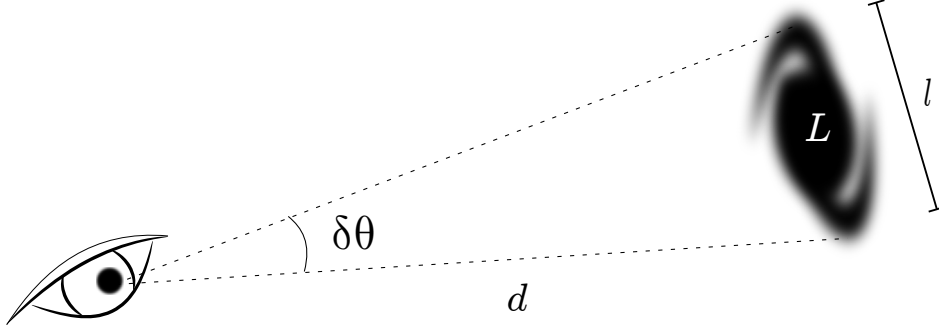


Figure 2.1: If either the physical size, l , or the intrinsic luminosity, L , of a light source is known, the angular diameter distance or the luminosity distance to the source can be determined.

the flux of an object which emits radiation with a luminosity L at a distance of d is given by the inverse square law, $f = L/(4\pi d^2)$, as the light from the object is spread over a sphere of area $4\pi d^2$. This inspires a definition of distance based on the apparent brightness of an object, the **luminosity distance**, which only depends on the observed flux and the intrinsic luminosity of the object,

$$d_L \equiv \left(\frac{L}{4\pi f} \right)^{1/2}. \quad (2.14)$$

When space is expanding, however, the luminosity is not only reduced according to the inverse square law. The expansion causes both a redshift of the individual photons and lowers the frequency with which they are received. Therefore, the object will appear further away than in a non-expanding universe. Specifically, consider an object at a proper distance of $d_p(t_0)$, which emitted the light we are now receiving at time t_e , when the scale factor of the universe was a_e . The radius of the sphere over which the photons are spread today is $d_p(t_0)$, the wavelengths of the individual photons are stretched by a factor of $1/a_e = (1+z)$, and the time interval between their reception is increased by the same factor. Therefore, the received flux is given by $f = \frac{L}{4\pi d_p(t_0)^2 (1+z)^2}$, and the relation between the luminosity distance and the proper distance in the expanding universe is

$$d_L = d_p(t_0)(1+z). \quad (2.15)$$

Another way of estimating the distance to a familiar object is from its apparent size. In a flat and stationary space, the (small) angle $\delta\theta$ subtended by an object can be approximated as $\delta\theta \approx l/d$, where l is the physical size of the object perpendicular to the line of sight, and d is again the distance, as illustrated in figure 2.1. This inspires yet another measure of the distance to the object, the **angular diameter distance**,

$$d_A \equiv \frac{l}{\delta\theta}. \quad (2.16)$$

In an expanding universe, however, the *image* of the object – and thereby its apparent size – expands with the universe in the time that passes between the emission and reception of light, even though the actual object does not change its size. That means that an object will appear closer than in a non-expanding universe. Specifically, let l be the physical size of the object, which is held together with forces (such as gravity) so that it does not expand with the universe. Since the light from the edges of the object moves along a path which has $d\theta = d\phi = 0$, the angular separation between the edges of the object at the time of emission is the same as today, $\delta\theta$. Given the measured angular size $\delta\theta$, the physical separation between the edges of the object at the time of emission must be $\delta\theta \cdot d_p(t_e) = \delta\theta \cdot d_p(t_0)/(1+z)$, and since this is equal to the physical size of the object, l , it is found that the angular diameter distance is related to the proper distance via

$$d_A = \frac{d_p(t_0)}{1+z}. \quad (2.17)$$

Objects with a known luminosity or a known physical size are known as standard candles and standard yardsticks, respectively. Such objects provide us with a way of measuring distances in the universe, which can then be converted to proper distances by using the measured redshifts. If the recession of an object due to the expansion of space is interpreted as a radial velocity, this can also be calculated from the observed object. This is the topic of the next section.

2.6 Redshifts and velocities in a homogeneous and isotropic expanding universe

We can calculate the radial velocity due to the expansion of an object with redshift, z , by differentiating the proper distance, $d_p(t) = a(t) \cdot r$, with respect to time, and evaluating the expression at t_0 [19]. By definition, the comoving distance, r , does not change due to the expansion, so only the scale factor needs to be differentiated, and expressing this via $H = \dot{a}/a$ and $r = d_p(t_0)$ via equation 2.13, the radial velocity of an object at redshift z is found to be

$$v_r(t_0) = \dot{a}(t_0)r = H_0 \cdot r = c \int_0^z \frac{dz}{H(z)/H_0}. \quad (2.18)$$

Hence, we see that Hubble's law, equation 2.9, simply follows from the definition of the proper distance and the interpretation of the increasing proper distance between the observer and the observed object, which is actually caused by the expansion of space, as a radial velocity of the observed object [18]. Note that, since $H = H_0 \sqrt{\Omega_m(1+z)^3 + \Omega_\Lambda}$, the last expression relating this radial velocity to the measured redshift does not depend on H_0 [19].

2.6.1 Low z approximations

If we ignore the dependence of the Hubble parameter on redshift, i.e. make the approximation $H = H_0 \sqrt{\Omega_m(1+z)^3 + \Omega_\Lambda} \approx H_0$, equation 2.18 reduce to

$$v_r \approx cz. \quad (2.19)$$

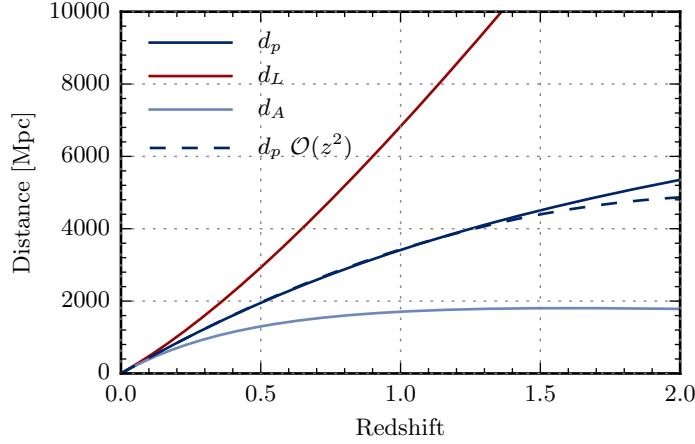


Figure 2.2: The dependence of the proper distance, the luminosity distance and the angular diameter distance on the cosmological redshift, for a model with $\Omega_m = 0.3$, $\Omega_\Lambda = 0.7$ and $H_0 = 67.8 \text{ km/s/Mpc}$. We also show the approximation for the proper distance from equation 2.20.

This is a useful approximation at redshifts sufficiently low that the Hubble constant has not changed appreciably in the time that has passed since the observed light was emitted. And since $v_r = H_0 \cdot r$, it can be used to estimate the Hubble constant from observations at low redshift, if the distances have been measured. This was the approach used by Edwin Hubble.

But today, objects are being observed at much higher redshifts than at Hubble's time. Furthermore, we have moved into an era of "precision cosmology", where cosmological parameters are being estimated with an accuracy of a few percent. Therefore, a better approximation than equation 2.19 is needed. The rate with which the Hubble parameter changes with time, to first order in z , is typically quantified by the *deceleration parameter*, defined by $q_0 \equiv -\left(\frac{\ddot{a}}{\dot{a}^2}\right)_{t=t_0}$. From the Friedmann equation it is found to be equal to $q_0 = \frac{3}{2}\Omega_m - 1$. By expanding $H(z)^{-1}$ to first order around $z = 0$ before carrying out the integral in equation 2.18, it is found that

$$H_0 \cdot r \approx cz \left[1 - \frac{1+q_0}{2}z \right]. \quad (2.20)$$

Of course, the distance-redshift relationship can be expanded to higher order to obtain any required precision. In figure 2.2, we plot the different types of distances we have discussed as a function of redshift, as well as the approximation for the comoving distance, $r = d_p(t_0)$, given in equation 2.20, to show when they start to deviate from each other, and when the approximation breaks down.

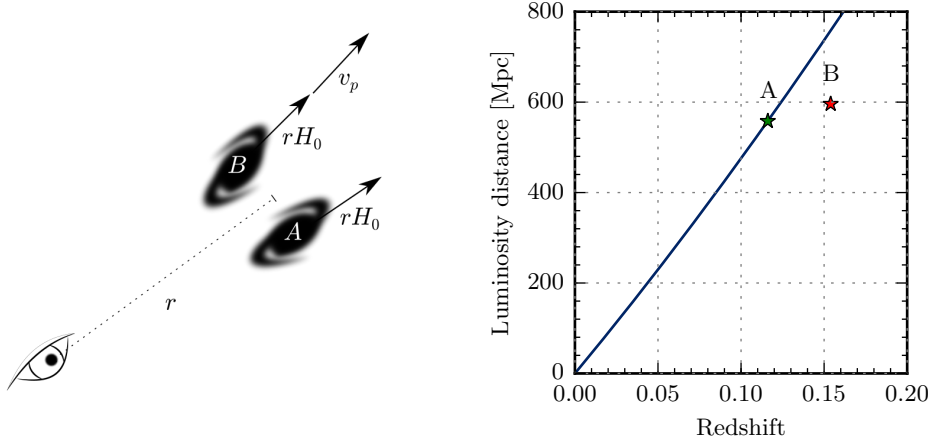


Figure 2.3: **Left:** Illustration of the galaxies A and B, relative to the observer. **Right:** The perturbation of the redshift and the luminosity distance due to the peculiar velocity. Both galaxies are placed at a proper distance of 500 Mpc, and galaxy B is given a (extreme large) peculiar velocity of 10 000 km/s (inspired by a similar figure in [20]).

2.7 Distances and redshifts in an inhomogeneous universe

Until now, distances and redshifts have been treated under the assumption of a perfectly homogeneous and isotropic universe. The actual universe, however, is not homogeneous and isotropic – there are large regions of the universe where the density is much higher than the average density, such as galaxies and galaxy clusters, and other regions where the density is much lower than average, such as voids. Inhomogeneities create an additional velocity component for galaxies, the so-called *peculiar* velocity, caused by the differences in the gravitational pull from different directions. Inhomogeneities also affect light as it propagates from the galaxies to us, perturbing both its redshift and its direction. To determine which consequences these effects have on the redshifts and distances we observe, we will consider two galaxies at a present day proper distance $d_p(t_0)$, as illustrated in figure 2.3. One of the galaxies – galaxy A – simply moves with the Hubble flow (no peculiar velocity), while the other galaxy – galaxy B – has an additional radial peculiar velocity v_p . The total radial velocity of galaxy B is found by differentiating the distance to the galaxy with respect to time,

$$v_{r,B}(t_0) = \dot{d}_{p,B}(t_0) = \dot{a}(t_0) \cdot r + a(t_0) \cdot \dot{r} = H_0 \cdot r + v_p, \quad (2.21)$$

that is, the total velocity is simply the sum of the two contributions.

2.7.1 Peculiar velocity and measured redshift

Let \bar{z} be the cosmological redshift, i.e. the redshift stemming from the expansion of space, which is common for the two galaxies A and B. If we are only considering the effects of peculiar velocities,

and ignore the additional effects on light caused by the inhomogeneities it passes through on its way from the galaxies to us, \bar{z} is equal to the measured redshift of galaxy A¹. The redshift measured for galaxy B, on the other hand, is different from \bar{z} due to the extra redshift caused by the peculiar velocity – the measured redshift for this galaxy will be denoted by z . The redshift caused by the radial component of the peculiar velocity can be calculated from the formula for the relativistic Doppler effect,

$$1 + z_p = \sqrt{\frac{1 + v_p/c}{1 - v_p/c}}, \quad (2.22)$$

whereas the cosmological component is related to the radial velocity due to the expansion of space as described in equation 2.18. Even though the total velocity of galaxy B is seen to be the sum of the cosmological and peculiar components, this is not the case for the redshifts. Denoting the wavelength of light emitted by galaxy B by λ_e , and the wavelength observed by us λ_0 , the redshift will be given as $1 + z = \lambda_0/\lambda_e$. The redshift caused by the peculiar motion alone is $1 + z_p = \lambda_p/\lambda_e$, where λ_p is the wavelength that would be observed by galaxy A, and the additional redshift caused by the expansion of space is $1 + \bar{z} = \lambda_0/\lambda_p$. So, the total redshift must be given by [19]

$$1 + z = \frac{\lambda_0}{\lambda_e} = \frac{\lambda_0}{\lambda_p} \frac{\lambda_p}{\lambda_e} = (1 + \bar{z})(1 + z_p). \quad (2.23)$$

2.7.2 Peculiar velocity and measured distance

The peculiar velocity of galaxy B does not only affect the measured redshift. As seen in section 2.5, in a homogeneous and isotropic universe, different types of distances are related to each other by factors of $(1+z)$. Here, we will consider how this needs to be adjusted when the measured redshifts are *not* purely cosmological. We only consider corrections to first order in v_p/c (the peculiar velocities are typically of order ~ 300 km/s). If we assume that the observer has no peculiar velocity, the angular diameter distance is unchanged [20] – that is, the angular diameter distance is the same to galaxy A and B. The luminosity distance to galaxy B can then be found from² $d_L = d_A(1+z)^2$ by inserting the total expression for the redshift of galaxy B from equation 2.23 [20],

$$d_L(z) = d_A[(1 + \bar{z})(1 + z_p)]^2 = d_A(1 + \bar{z})^2(1 + z_p)^2. \quad (2.24)$$

If we define $\bar{d}_L(\bar{z})$ as the luminosity distance in a homogeneous universe corresponding to a redshift \bar{z} , which is equal to the luminosity distance to galaxy A, we finally obtain

$$d_L(z) = \bar{d}_L(\bar{z})(1 + z_p)^2 \approx \bar{d}_L(\bar{z})(1 + 2z_p). \quad (2.25)$$

In the right panel of figure 2.3, the shift in luminosity distance and redshift due to a radial peculiar velocity of 10 000 km/s at a proper distance of $d_p(t_0) = 500$ Mpc is shown³.

¹We are also assuming that the observer does not have any peculiar velocity.

²This relation, which follows from the expressions for d_L and d_A in a homogeneous and isotropic universe, also holds in an inhomogeneous universe. See for example [21, chapter 14].

³Such a large peculiar velocity is extremely unlikely, and some of the approximations made in order to derive equation 2.25 are not very good when the peculiar velocity becomes relativistic. However, we are only showing the figure as an illustration of the effect of the peculiar velocities on the observed quantities.

In the next chapter, we will have a closer look at the inhomogeneities, and see how they evolve.

Chapter 3

Evolution of structure

In the previous chapter, we considered the overall evolution of the universe, governed by the theory of general relativity. For the majority of this treatment, we considered a universe that exactly obeyed the cosmological principle, i.e. a universe that was entirely homogeneous and isotropic. At the end of the chapter, however, we introduced inhomogeneities into the universe, and discussed some effects of these, most importantly peculiar velocities, and their effects on a few observables.

In this chapter, we will take a closer look at the inhomogeneities, and introduce a set of equations which can be used to predict how the perturbations in the density field evolve in a given cosmological model. A lot of complicated physics is relevant for this purpose, and analytical solutions to the equations governing these processes can only be found under constrained circumstances, where the density perturbations are very small. Fortunately, this is the case in the early universe, which implies that at early times, the evolution of density perturbations can be described accurately using linear perturbation theory.

In order to get a good description of the distribution of matter in the present day universe at scales below a few 10s of Mpc, the methods introduced in this chapter are insufficient. At some point, the density perturbations at these scales grow too large for the linear approximations to be accurate. To follow structure formation in the non-linear regime, numerical N-body simulations can be used. These will be discussed in the next chapter. But in order to initialize the simulations, it is necessary to produce some initial conditions. This chapter introduces the necessary formalism to understand how such initial conditions are created. Furthermore, the linear equations for the evolution of density perturbations still holds at large scales today, and will be used for some of the studies presented in this thesis. The derivations performed in this chapter are mostly based on [22, chapter 9].

3.1 The two point correlation function and the power spectrum

In order to describe how the density at each point of the universe deviates from the mean density, ρ_0 , we consider a point of comoving position \mathbf{x} and density $\rho(\mathbf{x})$, and define the *overdensity*

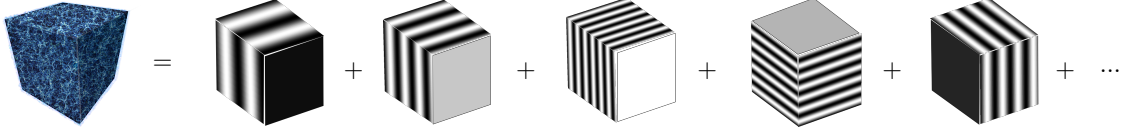


Figure 3.1: Illustration of the Fourier decomposition of the density field.

parameter as

$$\delta(\mathbf{x}) \equiv \frac{\rho(\mathbf{x}) - \rho_0}{\rho_0}. \quad (3.1)$$

It seems reasonable to require the density field, and hence δ , to be a continuous variable. In this case, the values that δ takes at two nearby points must be correlated. This is quantified by the correlation function,

$$\xi(\mathbf{x}) \equiv \langle \delta(\mathbf{x}') \delta(\mathbf{x}' + \mathbf{x}) \rangle, \quad (3.2)$$

where $\langle \rangle$ denotes the average over a volume sufficiently large that the universe can be taken to be homogeneous and isotropic, which are usually assumed to be the case on scales larger than a few 100s of Mpc. Because of isotropy, the correlation function cannot depend on the direction of \mathbf{x} , only on its size, so $\xi(\mathbf{x}) = \xi(x)$. The correlation function expresses the tendency for fluctuations in the density field to occur with a separation of x , that is, it is a measure of how "clumpy" the universe is on this scale.

This can also be expressed in Fourier space, as a sum of density fluctuations with different wavelengths λ , or wavenumbers $k = \frac{2\pi}{\lambda}$, as illustrated in figure 3.1. Specifically, the Fourier expansion of the overdensity field in an arbitrarily large box of volume V with periodic boundary conditions can be written as

$$\delta(\mathbf{x}) = \frac{1}{V} \sum_{\mathbf{k}} \delta_{\mathbf{k}} e^{i\mathbf{k} \cdot \mathbf{x}}, \quad \text{with } \delta_{\mathbf{k}} = \int_V d^3\mathbf{x} \delta(\mathbf{x}) e^{-i\mathbf{k} \cdot \mathbf{x}}, \quad (3.3)$$

where $\mathbf{k} = \frac{2\pi\mathbf{n}}{V^{1/3}}$ and \mathbf{n} is a triple of integers. Using this expansion, the two-point correlation function can be written as

$$\xi(x) = \frac{1}{V^2} \sum_{\mathbf{k}, \mathbf{k}'} \langle \delta_{\mathbf{k}} \delta_{\mathbf{k}'} \rangle e^{i(\mathbf{k} + \mathbf{k}') \cdot \mathbf{x}'} e^{i\mathbf{k} \cdot \mathbf{x}}. \quad (3.4)$$

Since the left hand side does not depend on \mathbf{x}' , the right hand side cannot do so either, so it follows that $\langle \delta_{\mathbf{k}} \delta_{\mathbf{k}'} \rangle = 0$ if $\mathbf{k} \neq -\mathbf{k}'$, that is

$$\xi(x) = \frac{1}{V^2} \sum_{\mathbf{k}} \langle \delta_{\mathbf{k}} \delta_{-\mathbf{k}} \rangle e^{i\mathbf{k} \cdot \mathbf{x}}. \quad (3.5)$$

Furthermore, for $\delta(x)$ to be real, $\delta_{-\mathbf{k}} = \delta_{\mathbf{k}}^*$, so

$$\xi(x) = \frac{1}{V^2} \sum_{\mathbf{k}} \langle |\delta_{\mathbf{k}}|^2 \rangle e^{i\mathbf{k}\cdot\mathbf{x}} \quad (3.6)$$

$$\equiv \frac{1}{V} \sum_{\mathbf{k}} P(\mathbf{k}) e^{i\mathbf{k}\cdot\mathbf{x}}, \quad (3.7)$$

where the last equation contains the definition of the power spectrum, $P(\mathbf{k}) = \frac{1}{V} \langle |\delta_{\mathbf{k}}|^2 \rangle$. This shows that the power spectrum is a measure of the amplitudes of density perturbations of each wavelength, $\lambda = \frac{2\pi}{k}$.

3.1.1 The variance of the density field and the amplitude of the power spectrum

Later in this chapter, we are going to study the equations governing the evolution of density perturbations, which predict how clustering on each scale grows with time in linear theory. In addition to this, some way to quantify the initial size of the density perturbations, i.e. a normalization of the power spectrum, is needed. This cannot be predicted theoretically, and therefore has to be determined by observations. Note that all of this only concerns the power spectrum that can be predicted by linear theory, the so-called linear power spectrum.

The amplitude of the power spectrum is usually specified in terms of the root-mean-square variance of the density field, $\sigma^2 = \langle \delta^2(\mathbf{x}) \rangle - \langle \delta(\mathbf{x}) \rangle^2$. Since, per definition, $\langle \delta(\mathbf{x}) \rangle^2 = 0$, this can be obtained from the correlation function as $\sigma^2 = \xi(0)$, and hence from the power spectrum as $\sigma^2 = \frac{1}{V} \sum_{\mathbf{k}} P(k)$.

However, this variance depends on how small structures can be resolved, so the total variance of the density field is not a very good choice for the normalization. To mitigate this problem, the density field can be smoothed on some scale, to erase rapid fluctuations, before the variance is measured. In general, this is done by convolving the overdensity field with a window function, $W(\mathbf{x})$, in order to obtain a smoothed overdensity, δ_L , where the density fluctuations on scales less than the smoothing length, L , have been averaged out. The window function is chosen such that $\int d^3\mathbf{x} W(\mathbf{x}) = 1$ and $W(\mathbf{x}) \approx 0$ for $|\mathbf{x}| \gtrsim L$, and the smoothed density field is given by

$$\delta_L(\mathbf{x}) \equiv \int d^3\mathbf{x}' W(\mathbf{x} - \mathbf{x}') \delta(\mathbf{x}'). \quad (3.8)$$

Fourier transforming this expression, one finds that $\delta_{L,\mathbf{k}} = \tilde{W}(\mathbf{k})\delta_{\mathbf{k}}$, where \tilde{W} is the Fourier transform of W , which is equal to one for $k = 0$, and goes to zero when k exceeds $K \equiv \frac{2\pi}{L}$. The variance of the overdensity field that has been smoothed with W is

$$\sigma_K^2 = \frac{1}{V} \sum_{\mathbf{k}} \tilde{W}_K^2 P(k) = \frac{1}{V} \sum_{|k| < K} P(k) \quad (3.9)$$

Expressing the sum over power at scales $|k| < K$ as an integral over the power spectrum that has been smoothed as described above, gives us a simple expression for calculating the variance of the smoothed power spectrum,

$$\sigma_K^2 = \frac{1}{(2\pi)^3} \int_0^\infty d^3\mathbf{k} \tilde{W}^2(k) P(k) = \frac{1}{2\pi^2} \int_0^K dk k^2 P(k). \quad (3.10)$$

The amplitude of the power spectrum is normally parameterized by σ_8 , which is obtained by setting $K = \frac{2\pi}{8 \text{ Mpc}/h}$, and integrating over the linear power spectrum. As the smoothing ensures that density variations within spheres of 8 Mpc/h have been leveled out, σ_8 can be interpreted as the variance in density between spheres of radius 8 Mpc/h.

3.2 Inflation and the Harrison-Zel'dovich spectrum

Before studying how power on different scales evolve in the early universe, in this section we describe the origin and the form of the initial power spectrum. The simplest initial power spectra are of the form $P(k) \propto k^n$, for which the power on scale k only depends on k , implying that power on different scales are uncorrelated. By the central limit theorem, if $\delta_{\mathbf{k}}$ are independent random variables, then, according to equation (3.3), the overdensity field is a sum of a large number of independent random variables, and therefore it follows a Gaussian distribution. So it is seen that power spectra of this form give rise to a Gaussian density field. Since the variance of the density field is determined by $P(k)$, and the Gaussian distribution for δ is fully described by its mean and variance, a Gaussian density field is fully described by the power spectrum. By calculating the root mean square of the mass fluctuations and the corresponding fluctuations in the gravitational potential for a power spectrum of form $P(k) \propto k^n$, it can be shown that this is independent of scale if $n = 1$. Such a power spectrum is called a scale invariant or Harrison-Zel'dovich spectrum [22].

A scale invariant power spectrum is what is predicted by the inflation theory. Inflation was proposed as a combined solution to three major problems in cosmology in 1981 by Alan Guth [9]: The flatness problem, the horizon problem, and the monopole problem. According to this theory, the universe started out radiation dominated, but at some very early time, a scalar field (similar to the dark energy that is dominating the universe today) became dominant, and caused the universe to expand violently for a tiny fraction of a second. This smoothed out any curvature present at the time, decreased the density of magnetic monopoles, and expanded the horizon. It also magnified quantum fluctuations in the vacuum, giving rise to a Harrison-Zel'dovich power spectrum. The vacuum state of the scalar field evolved during this expansion, eventually causing the inflation to stop. At this point, the scalar field is supposed to have decayed into photons and other relativistic particles, thereby reheating the background [18].

3.3 Linear structure formation

In chapter 2, it was described how the energy density and the gravitational field are linked through the Einstein equation, and it was mentioned that the conservation law for the energy-momentum tensor is equivalent to the continuity and Euler equations describing the time evolution of a fluid. In this section, we will take a closer look at these equations, mostly in the context of Newtonian mechanics, and apply them to the perturbations in the density field in the early universe. At early times, matter had not had time to cluster appreciably, and therefore the variations in the density field were very small, $|\delta| \ll 1$. For this reason, linear perturbation theory provides a very good description of the evolution of the density perturbations at these times.

Before recombination, the evolution of density perturbations was dominated by dark matter and radiation. If dark matter was relativistic in the matter dominated period, i.e. if the dark matter particles were moving with a speed comparable to the speed of light, it would have erased structure on small scales (comparable to the horizon, the distance that light has been able to travel during the lifetime of the universe). No suppression on these scales is observed, indicating that dark matter consists of some heavy particle, which becomes non-relativistic at very early times. Therefore, dark matter can be treated as a non-relativistic fluid, as will be described in the next section. The radiation (photons and the known species of neutrinos) on the other hand is to be treated as a relativistic fluid. Following [22, chapter 9], after we have considered the non-relativistic case, we will explain which modifications are needed in order to generalize to a relativistic fluid, such as the photon gas in the early universe. At last, a few remarks are made about how the resulting equations are used to predict the power spectrum after recombination.

3.3.1 Evolution of density perturbations

Non-relativistic fluid

In this section, we describe the dynamics of a non-relativistic fluid, corresponding to e.g dark matter, with a density field $\rho(\mathbf{x})$ and a comoving velocity field¹ $\mathbf{v}(\mathbf{x}) = \dot{\mathbf{x}}$, where \mathbf{x} as before is a comoving coordinate. One of the fundamental equations determining the dynamics of such a fluid is the continuity equation, which says that the density in a given volume must decrease as fluid is flowing out of the volume as well as, in the case of the expanding universe, in response to the expansion of the volume. Denoting by ∇ the gradient in comoving coordinates, the continuity equation is

$$\frac{\partial \rho}{\partial t} + 3H\rho + \nabla \cdot (\rho \mathbf{v}) = 0. \quad (3.11)$$

A second equation comes from applying Newton's 2nd law to the elements of the fluid, thereby relating the acceleration of the fluid elements to both the internal forces, i.e. pressure p , and

¹The physical velocities are obtained from the comoving velocities just as the physical distances are obtained from the comoving distances, by multiplying with the scale factor.

external forces. Expressing the gravitational force in terms of the gravitational potential, Φ , this equation – known as the Euler equation – in the expanding universe is

$$\frac{\partial \mathbf{v}}{\partial t} + (\mathbf{v} \cdot \nabla) \mathbf{v} + 2H\mathbf{v} + \frac{\ddot{a}}{a} \mathbf{x} = -\frac{1}{a^2} \left[\frac{1}{\rho} \nabla p + \nabla \Phi \right]. \quad (3.12)$$

Lastly, the gravitational potential Φ , from which the gravitational field can be obtained as $\mathbf{g}(\mathbf{x}) = -\nabla \Phi(\mathbf{x})$, can be shown from Newton's law of gravity to be related to the density field as

$$a^{-2} \nabla^2 \Phi - 4\pi G \rho = 0. \quad (3.13)$$

In order to predict how the mass distribution evolves, the continuity and Euler equations are expanded to first order around the mean density, ρ_0 , pressure, p_0 , velocity $v_0 = 0$, and gravitational potential Φ_0 . The perturbations imposed on these values are ρ_1 , p_1 , v_1 , and Φ_1 . From the linearized Euler equation, it is found that any vorticity, $\nabla \times \mathbf{v}$, decays with time. Therefore it is assumed to be zero from the start. Since a vector field with vanishing curl can be written as the gradient of a scalar field, this allows the definition of a scalar field ψ such that $\mathbf{v} = \nabla \psi$. In terms of this scalar field, the first order Euler equation becomes

$$\nabla \left[\frac{\partial \psi}{\partial t} + 2H\psi + \frac{1}{a^2} \left(\frac{p_1}{\rho_0} + \Phi_1 \right) \right] = 0. \quad (3.14)$$

Since \mathbf{v} is determined from the spatial dependence of ψ alone, one can add to ψ any function that depends only on time. And since the expression in the square brackets depends only on t , this can be used to ensure that

$$\frac{\partial \psi}{\partial t} + 2H\psi + \frac{1}{a^2} \left(\frac{p_1}{\rho_0} + \Phi_1 \right) = 0. \quad (3.15)$$

In terms of ψ and the overdensity parameter $\delta = \rho_1 / \rho_0$, the linearized continuity equation becomes

$$\frac{\partial \delta}{\partial t} + \nabla^2 \psi = 0. \quad (3.16)$$

By taking the Fourier transform of these two equations, one gets

$$\frac{\partial \delta_{\mathbf{k}}}{\partial t} = k^2 \psi_{\mathbf{k}}, \quad (3.17)$$

$$\frac{\partial^2 \delta_{\mathbf{k}}}{\partial t^2} + 2H \frac{\partial \delta_{\mathbf{k}}}{\partial t} + \frac{k^2}{a^2} \left(\frac{p_{1\mathbf{k}}}{\rho_0} + \Phi_{1\mathbf{k}} \right) = 0. \quad (3.18)$$

The first order part of the gravitational potential, $\Phi_{1\mathbf{k}}$, can be eliminated from the equation using the Poisson equation, which in Fourier space gives

$$\Phi_{1\mathbf{k}} = -\frac{a^2}{k^2} 4\pi G \rho_0 \delta_{\mathbf{k}}. \quad (3.19)$$

And lastly, assuming an adiabatic evolution, the speed of sound is $v_s^2 = \frac{p_{1\mathbf{k}}}{\rho_0 \delta_{1\mathbf{k}}}$ [22]. Using this, an equation for the evolution of the overdensity as a function of scale \mathbf{k} is found:

$$\frac{\partial^2 \delta_{\mathbf{k}}}{\partial t^2} + 2H \frac{\partial \delta_{\mathbf{k}}}{\partial t} + \left(\frac{k^2}{a^2} v_s^2 - 4\pi G \rho_0 \right) \delta_{\mathbf{k}} = 0. \quad (3.20)$$

This equation for the evolution of overdensities, which has been derived assuming a non-relativistic fluid, first became valid at the time when matter came to dominate over radiation in the universe which, as we saw in chapter 2, happened around the time when the scale factor was $a \sim 3 \times 10^{-4}$. Let us consider solutions to this equation, following [21, chapter 5]. If we only consider dark matter, which is pressureless, the term involving sound waves disappears. In this case, the equation is found to have a simple analytical solution in the matter dominated era. Ignoring the contributions from everything but matter in the Friedmann equation from chapter 2, it can be shown that the scale factor evolves as $a(t) \propto t^{2/3}$, which can be used to calculate $H = \dot{a}/a$ and $\rho_0 = \rho_c = \frac{3H^2}{8\pi G}$ (since we are assuming the universe to be flat). Inserting the expressions for H and ρ_0 into the equation for the density perturbations, two independent solutions are found: $\delta_{\mathbf{k}} \propto t^{2/3}$ and $\delta_{\mathbf{k}} \propto t^{-1}$. Only the first of these solutions corresponds to structures that are growing larger with time, which is the interesting case when we are concerned with the growth of structures.

More generally, the time dependence of the growing (and thereby dominant) solution to equation 3.20 is called $D(t)$, such that to a good approximation, $\delta(\mathbf{x}) = A(\mathbf{x})D(t)$, where A is just some function containing the spatial dependence of δ . On this basis, the *growth rate* is defined as the logarithmic derivative of the growing solution with respect to the scale factor, i.e.

$$f \equiv \frac{a}{D} \frac{\dot{D}}{D}. \quad (3.21)$$

In terms of D and f , the continuity equation can be written as

$$\nabla \cdot \mathbf{v} = -\delta \frac{\dot{D}_1}{D_1} = -Hf\delta. \quad (3.22)$$

The growth rate, f , is a function of the matter and energy density of the Universe. It has been found that it can be approximated by

$$f(\Omega_m, \Omega_\Lambda) = \Omega_m^{0.6} + \frac{\Omega_\Lambda}{70} \left(1 + \frac{1}{2} \Omega_m \right), \quad (3.23)$$

as shown in [23], generalizing a result presented in [24]. Due to the factor of 70 in the denominator of the term involving Ω_Λ , this shows that the growth rate is almost completely specified by the matter density of the Universe.

Relativistic fluid

In this section we describe the evolution of a relativistic fluid, which is a suitable model for the radiation dominating the very early universe. As in the previous section, the continuity equation,

the Poisson equation, and the Euler equation describe the evolution of density perturbations. However, each of these need to be modified for the relativistic case: The continuity equation does not apply for the radiation density, because of the redshift caused by the expansion of space. But it does hold for entropy, and using the relation between entropy and density for a black-body at a given temperature, one gets a conservation law for density that does apply. According to general relativity, the pressure of the fluid needs to be included in the Poisson equation. And because of the high velocities of the particles, special relativity needs to be taken into account in the Euler equation². Linearizing the equations and taking the Fourier transform, one gets an equation that determines the evolution of overdensities as a function of scale and time, equivalent to equation 3.20 for a non-relativistic fluid,

$$\frac{\partial^2 \delta_{\mathbf{k}}}{\partial t^2} + 2H \frac{\partial \delta_{\mathbf{k}}}{\partial t} + \left[\frac{k^2 c^2}{3a^2} - \frac{32}{3} \pi G \rho_0 \right] \delta_{\mathbf{k}} = 0. \quad (3.27)$$

From the Friedmann equation, it can be found how the Hubble constant and background density varies in the radiation dominated period. Using this and considering density perturbation with a wavelength smaller than the horizon, it can be shown that such perturbations are oscillating with respect to time. These short-wavelength fluctuations are in fact sound waves. Baryons, which are interacting with the radiation, are dragged along with the radiation fluid, and prevented from forming structures on scales smaller than the horizon. Dark matter, which only interacts with photons through the very weak force of gravity, cannot cluster on sub-horizon scales in this era either, as there are no growing solutions for modes within the horizon. On scales larger than the horizon, however, density perturbations in both matter and radiation are found to grow as $\delta_k \propto t$.

After the universe became matter dominated, dark matter began clustering on all scales, as we saw in the previous paragraph. However, the baryons were still being dragged along by the photons, and thereby prevented from clustering until recombination. Therefore, the way structures form is primarily determined by dark matter. Only after recombination, when electrons and protons formed neutral atoms and the strong interaction between baryons and photons ended, were the baryons free to cluster. At this point, potential wells already existed thanks to the clustering of dark matter, and the baryons fell into these potential wells.

The transfer function

Numerical calculations based on considerations analogous to the ones from the previous paragraphs can be performed for a realistic universe containing baryons, radiation, and dark matter, taking

² For future reference, the equations governing the evolution of a relativistic fluid turn out to be [22, chapter 9]

$$\frac{\partial \rho^{3/4}}{\partial t} + 3H \rho^{3/4} + \nabla \cdot (\rho^{3/4} \mathbf{v}) = 0, \quad (3.24)$$

$$\frac{\partial \rho}{\partial t} + (\mathbf{v} \cdot \nabla) \rho + \frac{1 - v^2/c^2}{\rho + p/c^2 \left(\nabla p + \frac{\mathbf{v}}{c^2} \frac{\partial p}{\partial t} \right)} = 0, \quad (3.25)$$

$$\nabla^2 \Phi - 4\pi G(\rho + 3p/c^2) = 0. \quad (3.26)$$

into account their mutual couplings. The results of such calculations can be expressed via the transfer function, $T(k)$, which describes how the primordial power spectrum, $P_0(k)$, i.e. the power spectrum generated by inflation, evolves over time,

$$P(k, t) = P_0(k) \cdot T^2(k, t). \quad (3.28)$$

For a particular model, this is calculated by following the linear evolution of the perturbations to the density fields of the various species of particles along with their interactions with each other [22].

Qualitatively, the value of the transfer function for perturbations of a given wavelength is determined by whether it became smaller than the horizon before or after matter came to dominate over radiation. As discussed above, modes within the horizon in the radiation dominated era were prevented from clustering, which means that power only grew at large scales in this period. When combined with the scale invariant initial power spectrum, $P_0(k) \propto k$, this creates a bend in the power spectrum around perturbations with a comoving wavelength of $\lambda \sim 125$ Mpc in the concordance model [22]. After matter began to dominate over radiation, dark matter could cluster on all scales. In this era, perturbations on all scales grow at the same rate, since equation 3.20 is independent of \mathbf{k} for dark matter. This implies that the shape of the power spectrum does not change after matter-radiation equality, it just scales [22, 25].

However, as mentioned in the introduction to this chapter, this description ceases to be a good approximation for the density perturbations on a given scale when they become too large. As the universe evolves and clustering grows, this happens for perturbations on larger and larger scales. In order to follow the evolution of the density field into the non-linear regime, N-body simulations are often employed. Such simulations are the topic for the next chapter.

Chapter 4

Non-linear structure formation: N-body simulations

In the previous chapter, we saw how small perturbations grow as a response to the effects of gravity and the expansion of space. When the perturbations have grown sufficiently, a small region might become substantially denser than the mean density of the universe. At this point, the linear theory from the last chapter breaks down, and the physics involved becomes much more complicated. The subsequent structure formation can be obtained using numerical calculations. In the very early universe, linear perturbation theory as described in the previous section is extremely accurate, and this is used to construct initial conditions for numerical simulations. These are subsequently fed to an N-body simulator, in this case GADGET-2 [26], which evolves the positions and velocities of particles according to the laws of non-relativistic gravity. In this chapter, a short description is given of the codes used to generate initial conditions, and the algorithm used by GADGET-2 is outlined.

4.1 CAMB

CAMB (Code for Anisotropies in the Microwave Background) is a publicly available code, written by Antony Lewis and Anthony Challinor, for calculating the CMB spectrum for various cosmological models [27]. It was originally based on CMBFAST, described in [28]. The basic method of these codes is to use the Boltzmann equation, which describes the couplings between particles (see for example [15]), the Einstein equation and the conservation of the energy-momentum tensor to calculate the anisotropies in the CMB. In the previous chapter it was outlined how the Einstein and conservation equations can be solved for the evolution of the overdensity parameter for a single substance. The output of CAMB provides transfer functions, $T(k, z)$, which, as we saw in the previous chapter, describe how the initial power spectrum set up by inflation has evolved up to a given redshift, as a function of k ,

$$P(k, z) = T^2(k, z)P_0(k). \quad (4.1)$$

4.2 Initial Conditions

To perform N-body simulations, one must start with a set of initial conditions, specifying the background cosmological model and the perturbations imposed on this background. These are created from the power spectrum predicted by inflation and the subsequent evolution of the density fluctuations in the early universe in which the structure formation is well described by linear perturbation theory, as discussed in the previous chapter.

By using the transfer functions supplied by CAMB, the initial condition generator, written into GADGET-2 by Jacob Brandbyge [29], imposes position and velocity perturbations to particles placed on a grid. The rate with which the density perturbations grow can be determined as the change in the power spectrum. As can be seen from equation 4.1, this can be found by comparing transfer functions at adjacent times.

4.3 GADGET-2

GADGET-2 (GALaxies with Dark matter and Gas intEract-2) is a publicly available N-body simulator, written by Volker Springel [26]. Although GADGET-2 is capable of treating both baryons and dark matter, here it will only be described how dark matter particles are treated, as this is the only type of N-body simulations that have been used for the research presented in this thesis.

The Friedmann and the fluid equation from chapter 2 are used to find the time evolution of the scale factor. The matter distribution is traced by particles placed on a 3D grid, with initial positions and velocities found by the code described in the previous section. The dynamics of the particles are described by the Hamiltonian

$$H = \sum_i \frac{\mathbf{p}_i^2}{2m_i a(t)^2} + \frac{1}{2} \sum_{ij} \frac{m_i m_j \varphi(\mathbf{x}_i - \mathbf{x}_j)}{a(t)}, \quad (4.2)$$

where \mathbf{x}_i represents the comoving coordinates of particle i , p_i is the corresponding momentum and m_i is the particle mass. The gravitational interaction between particles is described by the *discrete peculiar potential*, φ , which is described in the next section.

4.3.1 The gravitational field

When calculating the gravitational force between point masses, numerical problems arise if they get too near each other. This problem is non-physical, since it is caused by neglecting the physical extension of the masses. It is avoided by representing each particle in the simulation by $\tilde{\delta}$, which is the Dirac δ -function convolved with a normalized gravitational softening kernel of comoving scale ϵ . This has the effect of smearing out the otherwise point-formed particles before the gravitational potential is calculated [26]. The softening length, ϵ , sets a lower limit for the resolving power of the given simulation.

In cosmological simulations, space is assumed to be of infinite extension, which is realized using periodic boundary conditions. This has the consequence that only the deviations from the mean gravitational field, described by the *peculiar* gravitational potential, are needed in the calculations.

The peculiar gravitational potential stemming from a continuous matter distribution with a density $\rho(\mathbf{x})$ and a mean density $\bar{\rho}$ is given by the Poisson equation: $\nabla^2\phi(\mathbf{x}) = 4\pi G[\rho(\mathbf{x}) - \bar{\rho}]$. The potential appearing in equation 4.2 does not include the particle masses; it is related to the actual potential, ϕ , through a sum over all the particle masses: $\phi(\mathbf{x}) = \sum_i m_i \varphi(\mathbf{x} - \mathbf{x}_i)$. The potential φ is found using a discrete version of the Poisson equation,

$$\nabla^2\varphi(\mathbf{x}) = 4\pi G \left[\sum_{\mathbf{n}} \tilde{\delta}(\mathbf{x} - \mathbf{n}L) - \frac{1}{L^3} \right]. \quad (4.3)$$

The first term in the parentheses is a sum over all periodic images of a particle at a point \mathbf{x} , each image is represented by triplets of integers, $\mathbf{n} = (n_1, n_2, n_3)$. The second term corresponds to the subtraction of the mean density.

The potential, ϕ , is calculated using a combination of two techniques. It is split in a long range and a short range part in Fourier space, $\phi_k = \phi_k^{long} + \phi_k^{short}$, and the Particle Mesh (PM) technique is used for computing long range forces, and the Tree algorithm for short range forces. The long range part is then calculated using the *Particle Mesh* method, and the short range part using the *Tree* method, as described below.

Particle Mesh The long range force can be computed efficiently in Fourier space. To do this, at first a value of the mass density on the particle mesh is calculated, using the "cloud-in-cells" assignment which weighs the contribution from each particle linearly as a function of its distance from the mesh grid points. Then, a discrete Fourier transform is carried out, calculating the potential in Fourier space. And finally, taking the inverse Fourier transform provides the potential on the mesh. The forces are then interpolated onto the particle positions.

Tree method The short-range part of the potential can be solved in real space, and is computed by the Tree algorithm. In this method, the gravitation on a given particle is calculated by grouping all other particles in cells encompassing more and more particles the more distant they are. The force from each cell is then calculated by a multipole expansion. GADGET-2 only uses the monopole contribution.

4.3.2 Time integration

The short range potential, found by use of the Tree method, varies much faster than the long-range. In order to allow individual time steps in different regions, the potential in the Hamiltonian is separated into the long- and short-range terms discussed in the previous section,

$$H = H_{kin} + H_{short-range} + H_{long-range}. \quad (4.4)$$

This enables taking shorter time steps in regions of high density, where structure formation is happening much faster than in less dense regions. To be more specific, for each time step the state of a given particle is updated by applying a succession of *Kick*- and *Drift*-operators, which updates the momentum and position of a particle, respectively. This is the so-called *leap-frog* time integration scheme. The kick-operator depends on the gravitational potential, the short-range part of which varies much faster than the long-range part. By using the time-evolution operator

$$\tilde{U} = K_{lr}\left(\frac{\Delta t}{2}\right) \left[K_{sr}\left(\frac{\Delta t}{2m}\right) D\left(\frac{\Delta t}{m}\right) K_{sr}\left(\frac{\Delta t}{2m}\right) \right]^m K_{lr}\left(\frac{\Delta t}{2}\right), \quad (4.5)$$

where *lr* and *sr* are short for "long-range" and "short-range", respectively, and *m* is an integer, the long-range force only has to be evaluated once per time step. Through several uses of the time-evolution operator, GADGET-2 evolves the particle positions and velocities from the small density perturbation specified in the initial conditions to the final time of the simulation.

4.3.3 Output

At specified times during the simulation, the states of all particles are written to a file. Such a file is known as a *snapshot*, and it contains information about all particle positions and velocities. In the next chapter, it will be described how a *halo finder* can be used to identify bound structures in such a snapshot.

Chapter 5

Characterisation of structure

The clumping of matter as a result of structure formation produces gravitationally bound objects such as galaxies, clusters of galaxies, and super clusters. In one word, these are known as halos. In this chapter, a simplified description of how bound structures form is provided. This helps justifying the definition of a halo. It is then described how the halo finder ROCKSTAR identifies halos in the output of N-body simulations.

5.1 Spherical collapse

The simplest model for the formation of bound structures is the case where a spherical overdensity collapses under its self-gravity. In order to gain an understanding of the physical quantities characterizing a halo, such a collapse is considered in this section, following [22]. The collapse can be described by considering a shell of material with a radius of $r(t)$. Initially, at $t = 0$, the radius is zero, corresponding to the Big Bang. The shell then expands with the universe, but if the matter has too little energy to escape the gravity of the total interior mass, at some point the shell stops expanding and starts to collapse. Assuming that there is no flow of material across $r(t)$, the total interior mass, M , is constant. So the acceleration of the shell of material is

$$\frac{d^2 r(t)}{dt^2} = -\frac{GM}{r^2(t)}. \quad (5.1)$$

Under the conditions specified above, the solution to this equation is

$$r = \frac{r_{max}}{2}(1 - \cos \eta), \quad (5.2)$$

where η is just introduced as a convenient parametrization of time, given by

$$t = \sqrt{\frac{r_{max}^3}{8GM}}(\eta - \sin \eta), \quad (5.3)$$

The quantity r_{max} in this solution is seen to be the maximal radius of the collapsing matter - it is the so-called *turn-around radius*, at which the expansion halts and the collapse begins. The time when this takes place is called t_{max} . If it is assumed that the density inside $r(t)$ is homogeneous at turn-around, the potential energy at this time can be found to be $W_{max} = -\frac{3}{5}GM^2/r_{max}$. If it is furthermore assumed that all material turns around at the same time, the kinetic energy is zero at this time, and therefore W_{max} is the total energy of the collapsing mass.

When the collapsing object has reached equilibrium, its radius can be estimated from the virial theorem, which states that the potential energy is equal to twice the total energy of the collapse material, $W = 2E$. From this, the radius containing half of the total mass of the object, the *half-mass radius*, can be determined, it is found to be $r_h = 0.375r_{max}$. Virialization of the halo happens around the time $t = 2t_{max}$. From the Friedmann equation, the density of the universe in the matter dominated period, in which structures form, is found to evolve according to $\rho_m(t) = \frac{1}{6\pi Gt^2}$, from which the mean density of the universe at the time of virialization can be determined. This allows estimating the ratio of the mean density inside the half-mass radius, ρ_h , to the mean density of the universe, ρ_m , at the time of virialization, which reveals [22]

$$\frac{\rho_h}{\rho_m(2t_{max})} \approx 200. \quad (5.4)$$

This relationship can be used to define the virial radius, r_{vir} , as the radius at which the density equals 200 times the mean density of the universe. The mass inside this virial radius is used as a measure of the total mass of the halo. These definitions of the halo radius and halo mass are used by the halo finder ROCKSTAR, which is described in the next section.

5.2 ROCKSTAR

The halo finder ROCKSTAR [30, 31] identifies halos in the snapshots of N-body simulations using the algorithm sketched in figure 5.1. The first step is to divide the particles into smaller groups. This is done using a variant of the Friends-of-Friends algorithm, in which particles are grouped together if they are within a specified (spatial) distance of one another.

Within each FOF-group, a measure of the phase-space distance between two particles p_1 and p_2 (with positions $\mathbf{x}_1, \mathbf{x}_2$ and velocities $\mathbf{v}_1, \mathbf{v}_2$, respectively) is defined as

$$d(p_1, p_2) = \sqrt{\frac{|\mathbf{x}_1 - \mathbf{x}_2|^2}{\sigma_x^2} + \frac{|\mathbf{v}_1 - \mathbf{v}_2|^2}{\sigma_v^2}},$$

where σ_x^2 and σ_v^2 are the variances of the particle positions and velocities within the FOF-group. This metric combines distance in position and velocity into a single measure, normalized by the intrinsic scatter in positions and velocities to yield a dimensionless quantity. The phase-space distances between all particles in a group are calculated, and a phase-space-linking length is chosen such that 70% of the particles are linked together with at least one other particle. For each of the

hereby constructed new particle-groups, the process is repeated. This continues until a minimum of for example 10 particles remain at the deepest level of the hierarchy. The deepest level of each branch of this hierarchy represents a maximum phase-space-density, and these maxima are now considered seed halos. Each particle in the group is then assigned to the seed halo that is closest in phase-space.

For each halo, the distances to all other halos containing a larger number of particles are calculated. Each of the halos are then considered to be a satellite halo of the nearest, larger halo within the same FOF group. When this is done, the mass of each halo is calculated, where particles within a sub-halo are counted as part of the mass of the host. When all halo masses have been calculated in this manner, sub-halo memberships are recalculated: sub-halos are within r_{vir} of more massive host halos. At last, unbound particles are removed.

For each halo, the position of the halo center is calculated as the mean of the positions of the central particles, and the halo velocity is calculated as the mean of the velocities of the innermost 10% of the halo's particles.

From ROCKSTAR, a catalog of all the halos identified in the output of an N-body simulation is obtained. As mentioned in the beginning of this chapter, these represent galaxies, clusters, and super clusters of galaxies. In the next chapter, measurements of the actual universe will be considered. These are primarily based on observations of supernovae, which are expected to occur in star formation regions. Although the simulations described in chapter 4 only contain dark matter, and stars consists of baryonic matter, the probability of supernovae is still expected to be strongly correlated with the dark matter mass distribution, since the baryonic matter is expected to form structures by falling into the potential wells created by dark matter after recombination. Therefore, the halos in the catalogs constructed by ROCKSTAR should give a reasonably accurate idea about where supernovae are expected to occur¹.

¹These assumptions will be tested later in this thesis, when we use semi-analytical models of galaxy formation to get more accurate distributions of supernovae.

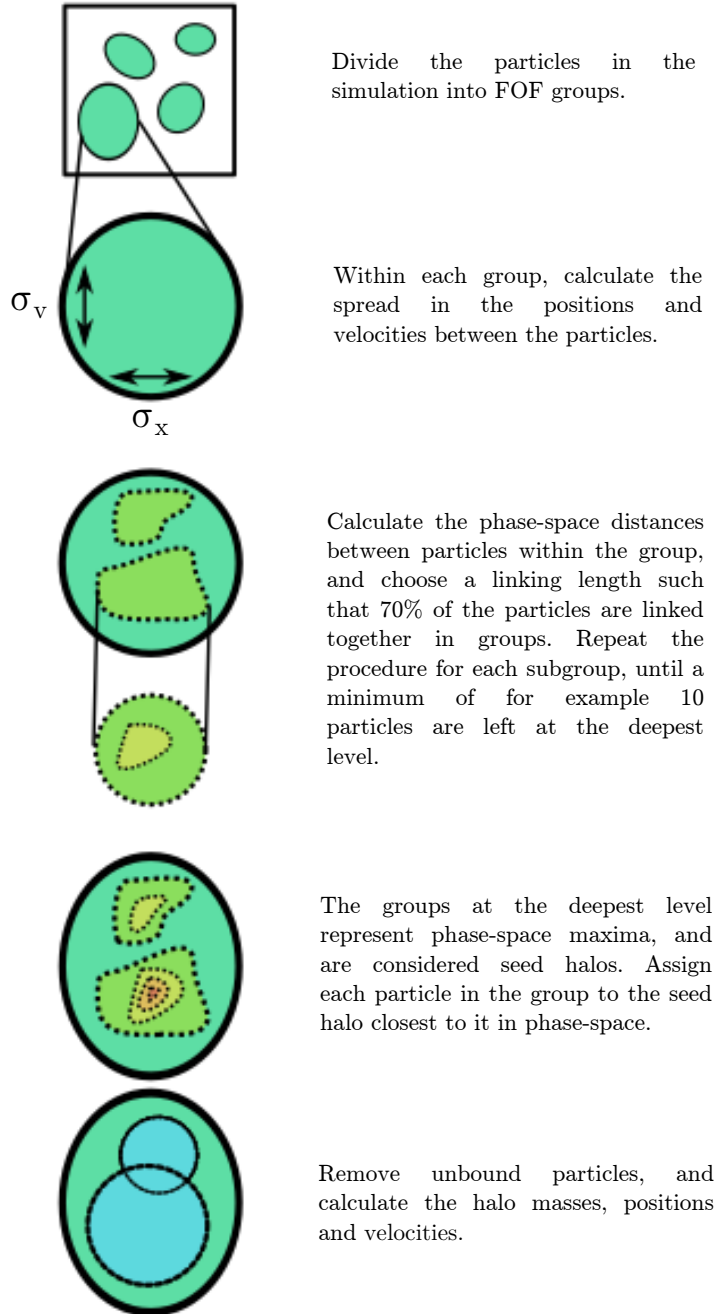


Figure 5.1: The ROCKSTAR halo finder algorithm, illustration from [30]. © The Astrophysical Journal. Reproduced with permission from the journal and the authors. The explanations for what happens at each step are my own.

Part II

Local variations in the Hubble constant

Chapter 6

The Hubble constant discrepancy

At the end of the first year of my PhD studies, the Planck collaboration revealed that measurements of the cosmic microwave background (CMB) points to a present day value of the Hubble constant, $H_0 = (67.80 \pm 0.77) \text{ km/s/Mpc}$ [32, table 5], much lower than the one observed in the local universe, which was at that time $H_0 = (73.8 \pm 2.4) \text{ km/s/Mpc}$ [33]. This inspired three studies of the local variations in the expansion rate of the universe, using different methods for estimating the Hubble constant in N-body simulations in both standard Λ CDM and in alternative cosmological models. In this chapter, the observations that motivated these studies are described. The three papers in which our results were published are presented in the subsequent chapters in slightly modified form.

6.1 Measurements of the CMB: Analysis and results from the Planck collaboration

In 2010, the Planck satellite started collecting radiation from the CMB, resulting in a temperature map with micro-Kelvin accuracy released in 2013 [32]. Anisotropies in the CMB temperature measured by Planck can be used to put constraints on a number of cosmological parameters. The anisotropies are treated as small fluctuations from a homogeneous and isotropic, flat FLRW universe. Given a set of initial conditions, the ionization history, and a specification of the constituents of the universe, the evolution of the perturbations can be computed accurately using CAMB, which was described in chapter 4. CAMB calculates the theoretical power spectrum of these fluctuations from a set of parameters which specifies a given model, and the parameter-space is sampled with CosmoMC, a Markov Chain Monte Carlo code, described in [34].

This allows determining the set of parameters characterizing our universe that best fit the data collected by the Planck satellite. The values of a set of derived parameters can then be calculated, assuming a specific cosmological model. One of these derived parameters is the Hubble parameter, often specified by $h \equiv \frac{H_0}{100 \text{ km/s/Mpc}}$. Assuming a standard Λ CDM universe, the Planck collaboration has found that $h = 0.678 \pm 0.0077$.

6.2 Measuring the expansion rate of the local universe

As described in chapter 2, the first measurement of the Hubble constant was presented by Edwin Hubble in 1929 [16], based on a graph – now known as the Hubble diagram – of the velocities of galaxies against their distance. Since then, the Hubble diagram has been improved and the data-set expanded several times. At the time the first results from the Planck satellite were published in 2013, the most accurate estimate was due to Riess et al. in 2011 [33], rendering a Hubble parameter of $h = 0.738 \pm 0.024$ ¹. This section provides a short description of how this value was obtained.

The recessional velocity of a light source can easily be found using the redshift of its light, as described in chapter 2. Finding the distances is much more difficult. The luminosity distance to a light source, also described in chapter 2, can only be determined if the inherent brightness of the source is known. This knowledge can be obtained by observing a potential standard light source to which the distance is known by other means. As soon as such a calibration has been carried out for one type of standard candles, this can in turn be used to determine the intrinsic brightness of other types of standard candles. In this process, each new distance indicator adds a step to the so-called distance ladder.

The most precise way to measure the distances to objects outside the solar system, is by using geometrical methods. This includes the parallax of stars – the apparent shift in the positions of stars as the Earth travels around the sun – which has been used to measure the distances to Cepheids within the Milky Way. Other geometrical methods include measuring the orbits of eclipsing binaries, which has been used to determine the distance to the nearby dwarf galaxy the Large Magellanic Cloud, and at greater distances, the orbits of masers (the microwave-equivalent of lasers) around the central black hole in the galaxy NGC 4258 (see for example [38] and references therein). Together, these methods provide ways to measure the distances to Cepheids both in the Milky Way and other galaxies, allowing a precise calibration of the relationship between the oscillation period and luminosity of the Cepheids.

At distances above ~ 10 Mpc, individual stars, such as Cepheids, cannot be resolved in galaxies. The best standard candle at these distances is a particular type of supernova, type Ia. By measuring the lightcurves, i.e. brightness against time after the explosion, of type Ia supernovae in galaxies with a distance determined with other methods, it has been possible to obtain a precise calibration of the luminosity of the supernovae against their lightcurves. As type Ia supernovae are extremely luminous events, they can be observed over great distances, making them great candidates for measuring the expansion rate of the universe.

To obtain the best possible calibration of the distance indicators, a simultaneous fit to all Cepheid and supernova data is performed in [33]. This fit includes parameters that account for

¹Recently, an even more accurate estimate has been published by the same authors, revealing $H_0 = (73.24 \pm 1.74)$ km/s/Mpc [35]. A recent update from the Planck Collaboration has $H_0 = (66.93 \pm 0.62)$ km/s/Mpc [36, table 8]. This increases the discrepancy to 3.4σ . However, according to another recent paper by the Planck collaboration [37], preliminary analysis of the low multipoles ($l \leq 800$) of the temperature fluctuations in the CMB points to a significantly higher value of h than the full data set, in much better agreement with the value measured in the local universe.

the dependence on metallicity of the period-luminosity relationship for the Cepheids, and reddening by dust of the light from the supernovae.

The next step is to fit the data to the theoretical distance-redshift relationship to obtain a value for the Hubble constant. In terms of magnitudes², the approximation given in equation 2.20 for the distance-redshift relation can be written as³

$$\log H_0 - 0.2M - 5 = \log \left(cz \left[1 + \frac{1}{2}[1 - q_0]z \right] \right) - 0.2m. \quad (6.4)$$

For the supernovae, this defines a constant, $a_v \equiv \log H_0 - 0.2M - 5$, which is found by fitting to the data. At last, the Hubble constant can be determined from the definition of a_v as

$$\log H_0 = \frac{M + 5a_v + 25}{5}. \quad (6.5)$$

In [33], the Hubble constant is determined from this expression using the absolute magnitude and distance to a supernovae in the galaxy NGC 4258, since the distance to this galaxy is known to great precision from the orbits of masers around the central black hole.

6.3 Studies of the local variation in the Hubble constant

The discrepancy between the present day value of the Hubble constant determined using each of the two methods described in the previous sections – fitting a multiple-parameter model to the temperature fluctuations of the CMB, and fitting to the measured luminosities and velocities of galaxies in the local universe – hints to some problem, either in the calibration of the supernova data, the measurements or fitting procedure used by the Planck Collaboration, or in our model of the Universe. However, another possibility is that the discrepancy is caused by the inhomogeneity of the actual universe, which allows for the expansion rate to vary between different regions. If we happen to live in a part of the Universe where the expansion rate is somewhat higher than the

² The brightness of astronomical objects is often specified using the logarithmic magnitude scale. In this scale, the *absolute magnitude* of an object is defined in terms of its luminosity, L , relative to a reference luminosity, L_{ref} , as

$$M \equiv -2.5 \log \left(\frac{L}{L_{\text{ref}}} \right), \quad (6.1)$$

where L_{ref} depends on which photometric pass-band the luminosity is measured in. The *apparent magnitude* is defined from the flux we receive from the object, relative to the flux of an object with luminosity L_{ref} when observed from a luminosity distance of 10 pc, that is

$$m \equiv -2.5 \log \left(\frac{L/[4\pi d_L^2]}{L_{\text{ref}}/[4\pi(10 \text{ pc})^2]} \right). \quad (6.2)$$

Rearranging, it is found that the difference between the absolute and apparent magnitudes is

$$m - M = 5 \log \left(\frac{d_L}{1 \text{ Mpc}} \right) + 25. \quad (6.3)$$

This is a measure of the distance to the object, and is defined as the *distance modulus*, $\mu \equiv m - M$ [18].

³In [33], an even more accurate approximation, including third orders of z , is used.

average value, this could potentially explain the difference between the local and the global, i.e. the CMB, value. This hypothesis is the starting point of the papers presented in the following three chapters.

Chapter 7

On the local variation of the Hubble constant

This chapter is dedicated to the description of the first study we carried out of the local variations of the Hubble constant. Except for a few modifications, it is identical to [1].

- [1] Io Odderskov, Steen Hannestad, and Troels Haugbølle, *On the local variation of the Hubble constant*, JCAP **2014** 10 028.

7.1 Introduction

As described in the previous chapter, the data released from the Planck satellite in 2013 seems to point to a relatively low value of the Hubble constant, while direct measurements relying mainly on Type Ia supernovae clearly favor a higher value, with the two being inconsistent at the 2.4σ level [32, 33]. There are several possible explanations for the disagreement between the two estimates of the expansion rate. It could be caused by a problem with the assumed cosmological model, or it could be that one (or both) of the estimates is either inaccurate or biased. The second possibility has been considered by Estathiou in [39] and by Clarkson et al. in [40]. Using an improved distance calibration, Estathiou has re-analyzed the data from [33] and found a lower value for the local Hubble parameter, which decreases the tension between the two estimates. Ref. [40] considers relativistic corrections to the distance to the CMB, and show that second order lensing corrections can possibly increase this distance by several percent, which in turn causes an increase in the best fit value of the Hubble parameter from the Planck data. Yet another possibility - the one that is tested in this paper - is that it is merely a result of the spatial variation in the expansion rate of our universe.

For a given cosmological model, the expansion rates estimated by observers at different locations are expected to vary according to some underlying distribution. To gain knowledge of the spread of this distribution, we perform N-body simulations of the model in question. Subsequently, structures are identified using a halo finder that generates a catalog containing the masses, posi-

tions, velocities, and substructures of all halos found in each simulation. From the halo catalogs, lists of observers are selected, under the assumption that the standard observer reside in a halo similar to the Local Group. Each observer is assumed to estimate the local Hubble parameter in his neighborhood by measuring the distances and velocities of halos located in a sphere around him, since this is where we would expect supernovae to be found. Finally, confidence intervals are constructed from the local Hubble parameter calculated by each of these observers. This is done in order to answer the question: Could the discrepancy between the inferred and the measured Hubble constants be due to cosmic variance?

The same question has been addressed in [41] and [42]. In [41], Marra et al. calculate the variation of local Hubble parameters based on the power spectrum, which expresses the variations of the underlying density field, and this in turn affects the velocity field and hence the local Hubble parameters. In [42], Wojtak et al. use the same approach as in this paper, i.e. N-body simulations, to estimate the spread in the local Hubble parameters. In their paper, they focus primarily on how the local Hubble parameters are affected by observer positions. While this is also discussed in the present paper, we furthermore investigate how the apparent variation is affected by only observing a fraction of the sky, and whether the cosmic evolution that takes place between the time that light is emitted by a supernova and observed by us can have a significant effect.

We finally note that measurements of variations in the Hubble parameter using type Ia supernovae is equivalent to measurements of the local bulk velocity field using the same tracers (see e.g. [43–48]).

The paper is organized as follows: In part 2, we describe the N-body-simulations that our analysis is based upon and the halo finder used to identify structure. In part 3, the calculation of the local Hubble parameters is outlined, and the selection of observers and of observed halos are motivated and described. In part 4, we present the outcome of the analysis, and finally we discuss the results in part 5.

7.2 Method

7.2.1 Simulations

The best fit cosmological parameters determined by the Planck collaboration [32] are used as the basis for N-body simulations of the universe. The N-body simulations are performed using a modified version of the GADGET-2 code [26], with initial conditions generated using a code written by J. Brandbyge [29] based on transfer functions computed using CAMB [34]. Specifically, the transfer functions are calculated with $(\Omega_b, \Omega_{CDM}) = (0.048, 0.26)$, whereas only cold dark matter is used in the N-body simulation. A flat universe is assumed, and $(h, \sigma_8) = (0.68, 0.84)$. The simulations are run from a redshift of $z = 50$ until $z = 0$.

The standard simulation is done in a box of sidelength 512Mpc/h with 512^3 particles. We perform two simulations of this size and resolution, but with different seeds for the random number generator that is used to construct the initial conditions, in order to determine how much the results

can be expected to vary between different occurrences of a universe with the same parameters. In order to check for numerical effects due to the simulation resolution and the simulation volume, we also perform two simulations with 1024^3 dark matter particles in boxes of 512Mpc/h and 1024Mpc/h, respectively. Still, all the simulations are of much smaller volume than the ones that are the basis for the analysis performed by Wojtak et al. in [42], which are of several Gpc/h, while the mass resolution is similar. The sample on which they base their analysis of the Hubble flow is therefore substantially larger than the ones used in this paper, and as a result the analyzes presented here will have a greater sample noise and a greater correlation between the observers. The latter is to some extent mitigated by using several boxes with independent random seeds. We identify 600 observers in each simulation, and use these to estimate of the mean and spread of the Hubble constant.

The observers in the simulations are spread across the entire simulation volume. In order for each of them to be able to observe in all directions, the box is taken to be periodic. To avoid an observer considering the same halo twice in his calculation of the Hubble constant, the maximal observed distance should be half a box length, that is 256Mpc/h, corresponding to a redshift of $z = 0.087$. This corresponds approximately to the greatest observed distance of $z \sim 0.1$ of the supernova surveys used in [33]. As in [33], in order to reduce the effect of the local, coherent flow, no halos closer than 30Mpc/h, corresponding to $z = 0.01$, are used.

7.2.2 Identifying halos

Halos are identified in the output of the N-body simulations using the halo finder ROCKSTAR, which was described in chapter 5.

7.3 Analysis

As mentioned, it is assumed that each observer estimates the local Hubble parameter, H_{loc} , by measuring velocities and positions of halos in his vicinity. The apparent velocities of observed halos contain two components: one from the expansion of space, and one from peculiar motion. When considering only halos in the $z = 0$ -snapshot, the radial velocities stemming from the a pure Hubble flow would be given by Hubble's law,

$$v_H = H_0 r, \tag{7.1}$$

where r is the comoving distance to the halo and H_0 is the global Hubble constant. Assuming that the observers cannot determine how large the peculiar component of the radial velocity is, they fit the distances and velocities of the halos around them to Hubble's law, using a least squares estimate, hereby getting a value for the local Hubble constant:

$$H_{loc} = \frac{\bar{r}\bar{v}}{r^2}, \quad (7.2)$$

where a bar denotes the mean and v is the total radial velocity of the observed halos, containing both the cosmological and peculiar components. Each observer is assumed to have transformed to the CMB rest frame, i.e. to correct the observed velocities for his own peculiar motion, before estimating the Hubble constant based in equation 7.2¹.

In actual observations, the position and velocity information of distant halos is primarily obtained from supernovae. In [33], 240 supernovae are used in estimating the local Hubble parameter, and for this reason we choose 240 observed halos for each of the observers in our mock survey. This is done by assuming that the probability of a supernova occurring in a given halo is proportional to the halo mass, and therefore making a mass-weighted selection of observed halos (this is in contrast to what is done in [42], where every halo within a given distance is used). The procedure results in a redshift distribution of the observed halos which is peaked at a higher value than the one used in [33], as shown in figure 7.1. In consequence we expect to slightly underestimate the variance of the local Hubble parameter at large distances.

There are some indications [49, 50] that the rate of type Ia supernovae not only depends on the stellar mass of a galaxy – or more precisely the star formation history – but there also exist a prompt component in the type Ia distribution dependent on the SFR in the galaxy. Given the current uncertainty in the fraction of prompt type Ia supernovae, this has not been taken into account in the selection of halos². When the selection of observed halos has been performed, they are binned according to distance, with the maximally observed distances (here from referred to by r_{max}) increasing from 67Mpc/h to 256Mpc/h. For each value of r_{max} , the estimates of the local Hubble constants are obtained using every observed halo within this distance.

7.3.1 Objectives

In order to determine how the variance of the local Hubble constants depend on various aspects of the observations, the observed halos are selected and handled in different manners, as is the choice of observer positions. Furthermore, effects of simulation seed, resolution, and volume are checked for, and we additionally study how the number of observed halos affect the variance. Below we describe each of these analyzes in more detail. In figure 7.2 a few of the analyzes are sketched for visualization, and an overview is given in table 7.1.

Choice of observers: The standard observer is chosen from the halo catalogs as a subhalo of mass $10^{12} - 10^{13} M_{\odot}/h$ in a host halo with mass $5 \cdot 10^{14} - 5 \cdot 10^{15} M_{\odot}/h$, since this approximately

¹When using lightcone snapshots, as will be described in the next section, equations 7.1 and 7.2 need to be modified to take the change in the Hubble parameter with time into account. This is done by fitting to equation 2.20: $d_p(t_0) = \frac{cz}{H_0} \left[1 - \frac{1+q_0}{2} z \right]$, where the redshift is approximated as $z \approx v_r/c$, and the deceleration parameter is calculated from the simulation parameters as $q_0 = \frac{1}{2}\Omega_m - \Omega_{\Lambda}$.

²In part III of this thesis, the effects of the distribution of type Ia supernovae, as modeled after the star formation histories of halos, on studies of the velocity field are investigated in much more detail.

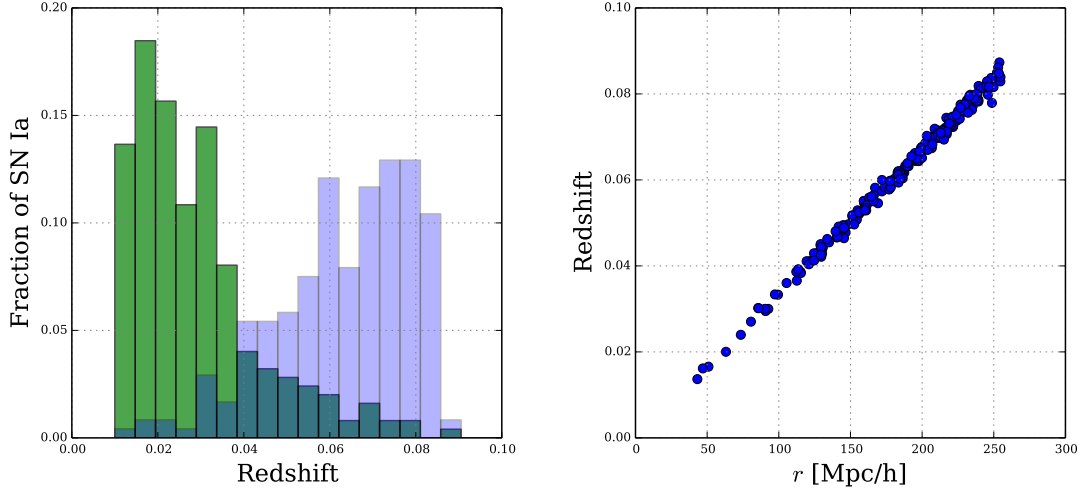


Figure 7.1: Left: Comparison between the redshift distribution measured by a typical observer in the mock catalogues (blue) and the redshift distribution of supernovae from Hicken et al. [51] (green), which closely resembles the one used by Riess et al. in [33]. Right: Hubble diagram obtained by the same mock observer.

Name	Nsim	Box [Mpc/h]	Survey geometry	Observers	Past lightcones
A.0	512	512	Full sky	Random in space	No
A.1	512	512	Full sky	Random in halos	No
A.2	512	512	Full sky	Local Group like	No
A.3	512	512	One cone	Local Group like	No
A.4	512	512	Two cones	Local Group like	No
A.5	512	512	Full sky	Local Group like	Yes
B	512	512	Full sky	Local Group like	No
C	1024	512	Full sky	Local Group like	No
D	1024	1024	Full sky	Local Group like	No

Table 7.1: Four different simulations have been run, named A-D. The number of particles in each simulation is N_{sim}^3 . For the standard simulation (A), six different analyzes have been performed, named A.0-A.5. Simulation B has the same characteristics as A, but with a different seed for the random number generator. All simulations are performed with the best fit parameters from the Planck satellite: $(\Omega_b, \Omega_{CDM}, h, \sigma_8) = (0.048, 0.26, 0.68, 0.84)$.

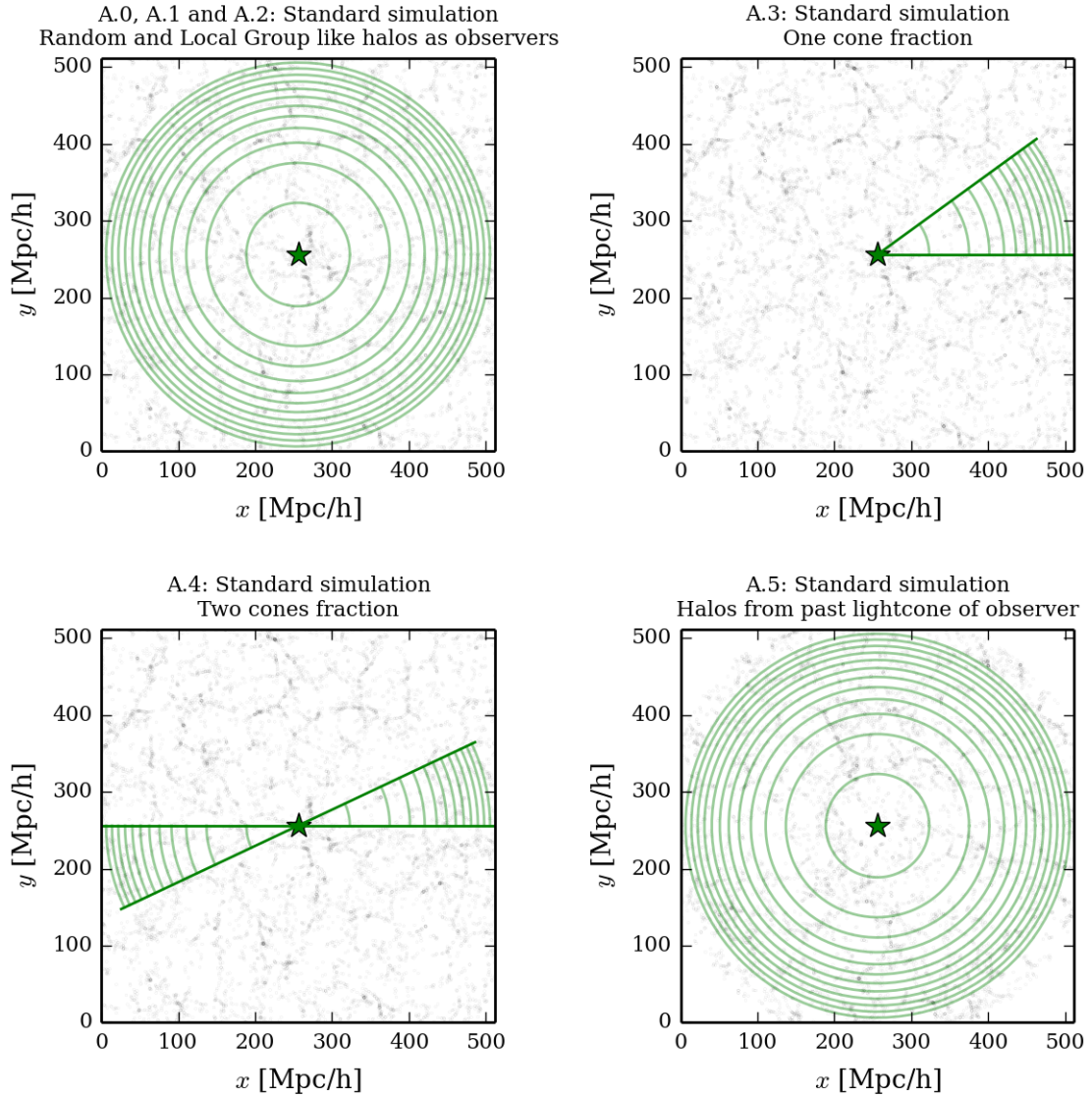


Figure 7.2: Positions of halos in a slab of thickness $10\text{Mpc}/h$, with illustrations of the observation performed by each observer (green star), with values of r_{max} shown as green circles (or arcs). For clarity, only every 5th value of r_{max} is shown.

corresponds to our position in the Local Group galaxy cluster that resides in the Virgo Super Cluster. The significance of the observer positions is checked by using two alternative selections: One in which the observer positions consists of positions chosen randomly in the simulation volume, and one in which the observer positions are chosen randomly among all the halos in the simulation.

Survey geometry: The actual supernovae used in estimating the expansion rate of the local universe are not distributed across the entire sky. In some directions, our sight is blocked, for example in the plane of the Milky Way. One could expect this to give rise to a higher variance, since the bulk flow in a particular direction is more likely to deviate from the Hubble expansion than the mean of the whole sky. To account for this effect in the analysis, at first only a small patch of the sky is observed. This patch is subsequently enlarged until it covers all of the sky. The number of supernovae is the same no matter if the whole sky or only a fraction is observed. We perform this analysis both with one cone, and with two cones pointing in opposite directions.

Cosmic evolution: Observing out to a redshift of $z \sim 0.1$, corresponds to observing 1.3 billion years back in time. When doing the same "observation" in the output of our N-body simulations, the time it takes light to travel from the distant halos is ignored, and therefore so are the changes in the growth and structure of the halos. We investigate the significance of this effect by using a locally developed plugin to GADGET-2 that during the course of the simulation reconstructs the past light cone of any observer in the box, dumping it to a snapshot on disk. Such snapshots are created for the positions of our chosen observers. Then the halo finder is applied to these past lightcone snapshots, using a functionality in ROCKSTAR in which the change in cosmological parameters as one looks backwards in time is taken into account in the analysis. Constructing the mock observations using past light cones takes into account the evolution in the cosmological model, and more accurately reproduces the actual observations.

7.4 Results

In Figures 7.3-7.6 we show how the mean of H_{loc}/H_0 among the chosen observers depend on the number of observed halos and the maximally observed distances for different choices of observers and observed halos. Confidence intervals are shown as coloured bands around the mean (solid line). The chosen confidence levels are 68.3, 95.4 and 99.7 per cent, all calculated symmetrically so that equal fractions of the locally measured Hubble constants fall below and above the interval. For comparison, the result from the standard analysis (on the right in figure 7.3) is indicated as dotted lines in all other plots.

The first plot in figure 7.3 shows H_{loc}/H_0 as a function of the number of observed halos. In figure 7.4, the analysis is repeated for two simulations with 1024^3 particles, in boxes of sidelength 512Mpc/h and 1024Mpc/h, respectively. This is done order to check that the simulation resolution and simulation volume have no significant effect on the results. The set of parameters used in the N-body simulations are the ones published by the Planck collaboration: $(\Omega_b, \Omega_{CDM}, h, \sigma_8) = (0.048, 0.26, 0.68, 0.84)$.

In figure 7.5 we show how the observer positions affect the measured values of H_{loc} (on the left). On the right, the observers are chosen randomly among all the halos in the simulation. In figure 7.6, the observations are performed using past lightcones of the Local Group like observers, so that cosmic evolution from the time that light was emitted from an observed halo is taken

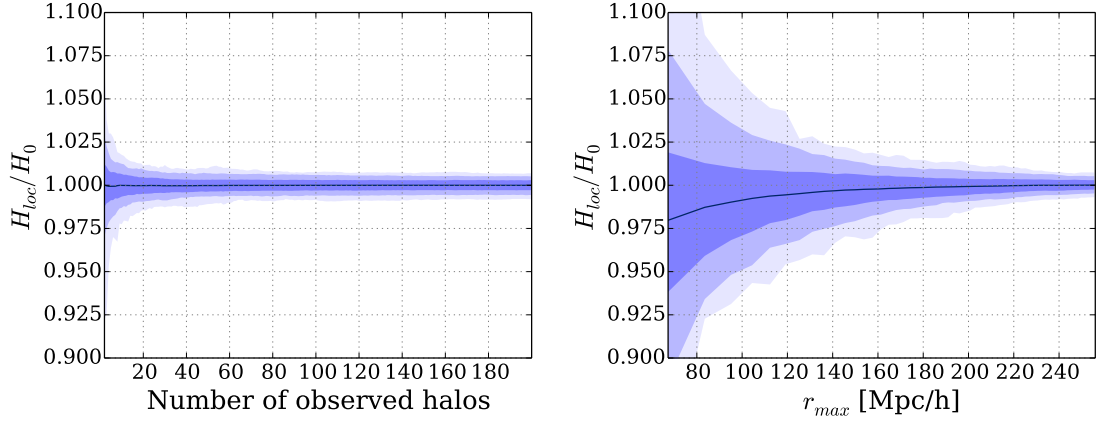


Figure 7.3: Left: Mean and scatter of the local Hubble parameter as a function of number of observed halos. The largest observed distance is held constant at 256Mpc/h, while the number of observed halos is varied from 2 to 200. Right: Mean and scatter of the local Hubble parameter as a function of the maximally observed distance. The chosen observers are Local Group like halos, each estimating the local Hubble constant by measuring the distance and radial velocities of 240 supernovae in nearby halos. The simulation consists of 512^3 particles in a periodic box of sidelength 512Mpc/h.

into account. In figure 7.7 we show how the width of the 68.3 per cent confidence interval varies as a function of both the distance r_{max} and the covered percentage of the sky. The results are summarized in table 7.2.

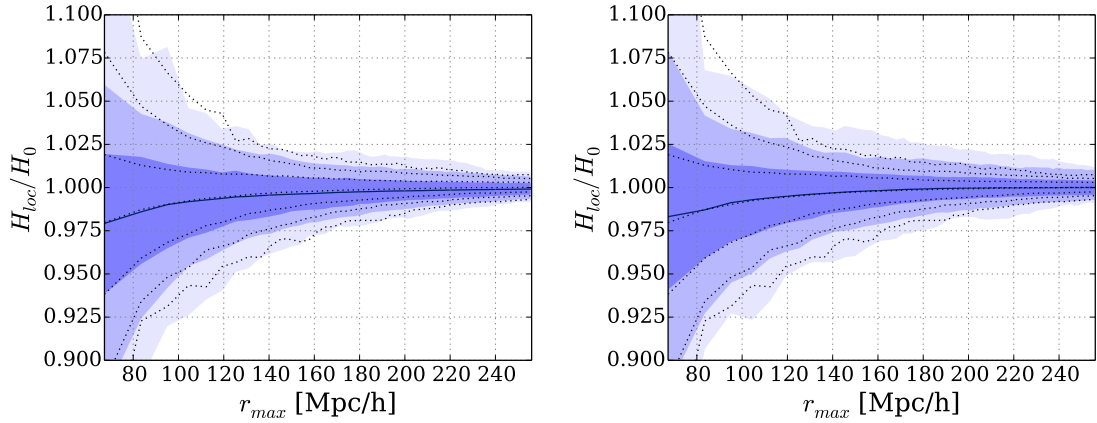


Figure 7.4: Left: Mean and scatter of the local Hubble parameter as a function of the maximally observed distance, calculated for a simulation with 1024^3 particles in box of 512Mpc/h. Right: Calculated for a simulation with 1024^3 particles in a box of 1024Mpc/h. Dotted lines indicate the result from the standard analysis.

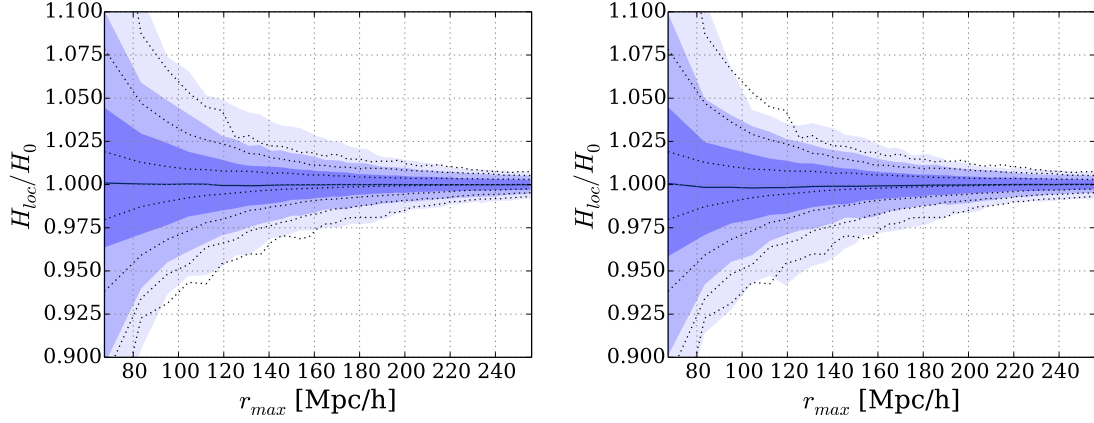


Figure 7.5: Left: Mean and scatter of the local Hubble parameter as a function of the maximally observed distance, when the chosen observers are distributed randomly in the simulation volume. Right: Observers chosen randomly among all the halos in the simulation. Dotted lines indicate the result from the standard analysis.

Name	Description	$\mu_{67}[\%]$	$\mu_{150}[\%]$	$\mu_{256}[\%]$	$\sigma_{67}[\%]$	$\sigma_{150}[\%]$	$\sigma_{256}[\%]$
Observers							
A.0	Random positions in space	0.1	0.0	0.0	4.6	0.9	0.3
A.1	Random positions in halos	0.1	-0.1	0.0	4.7	0.9	0.3
A.2	Local Group-like halos	-2.0	-0.3	0.0	4.5	0.9	0.2
10% sky coverage							
A.3	One cone	-2.6	-0.2	-0.0	4.8	1.2	0.4
A.4	Two cones	-2.6	-0.3	-0.0	4.2	1.1	0.4
Cosmic evolution							
A.5	Lightcone	-2.5	-0.3	0.0	4.4	0.9	0.2
Simulation							
B	Different seed	-1.7	-0.2	0.0	4.6	0.9	0.4
C	Box=512, Nsim=1024	-2.1	-0.4	-0.1	4.6	1.0	0.3
D	Box=1024, Nsim=1024	-1.7	-0.2	0.0	5.0	1.1	0.4

Table 7.2: Mean (μ) and variance (σ) of H_{loc}/H_0 at selected distances. The subscripts specify the distance in Mpc/h. All results are given in per cent.

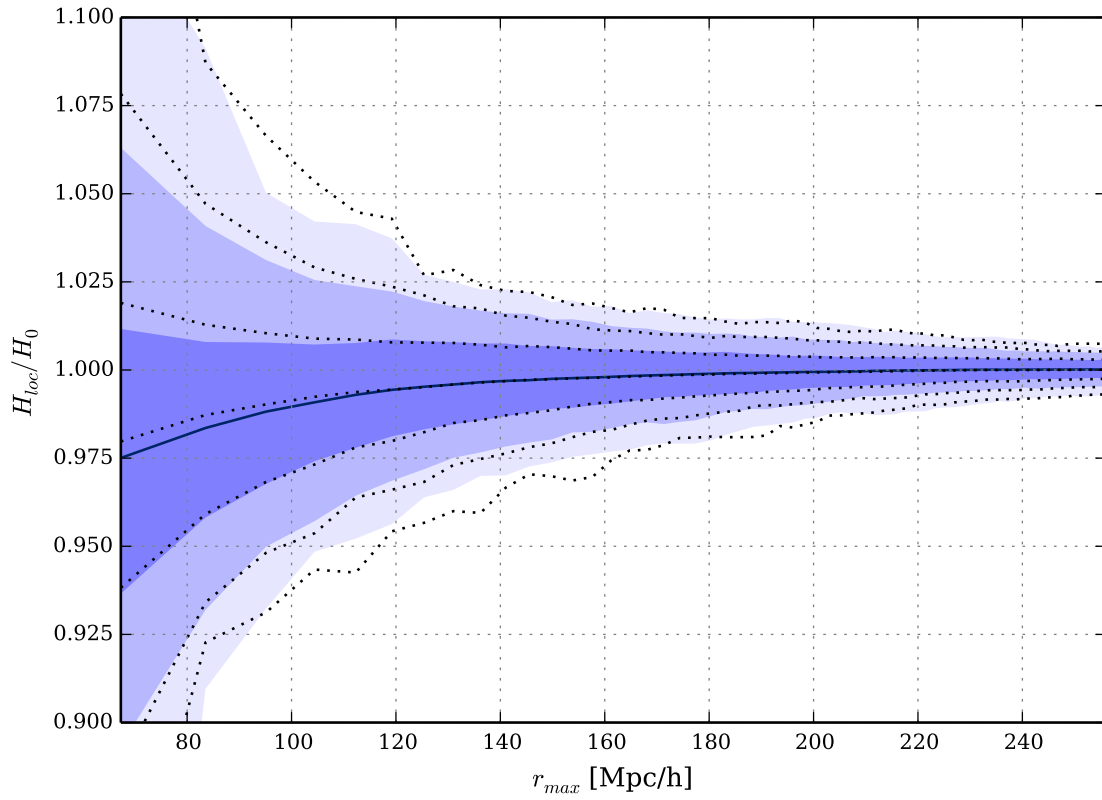


Figure 7.6: Mean and scatter of the local Hubble parameter as a function of the maximally observed distance calculated for Local Group like halos, with the effect of cosmic evolution taken into account by using lightcones. Dotted lines indicate the result from the standard analysis.

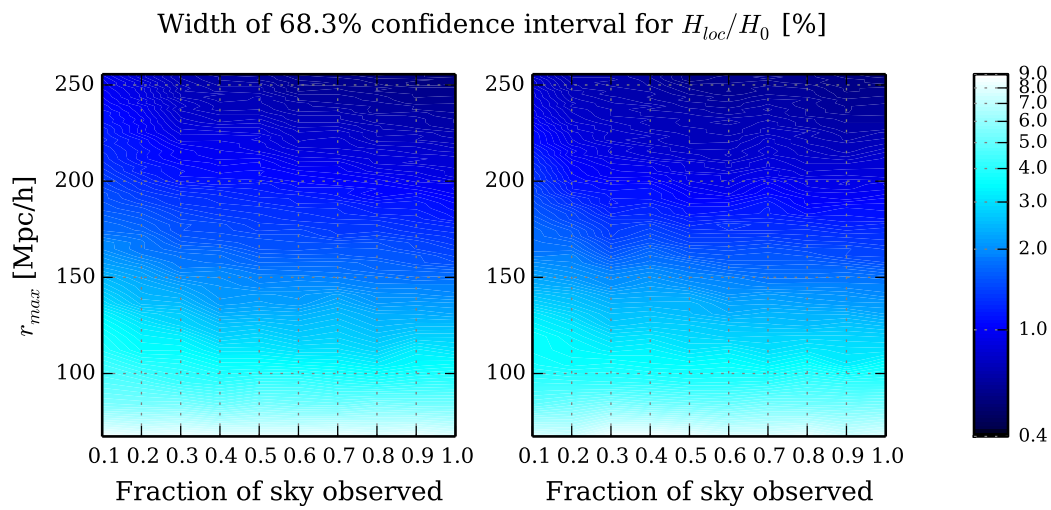


Figure 7.7: Width of 68.3% confidence interval for H_{loc}/H_0 when observing only a fraction of the sky. Left: One cone. Right: Two cones, pointing in opposite directions on the sky.

7.5 Discussion

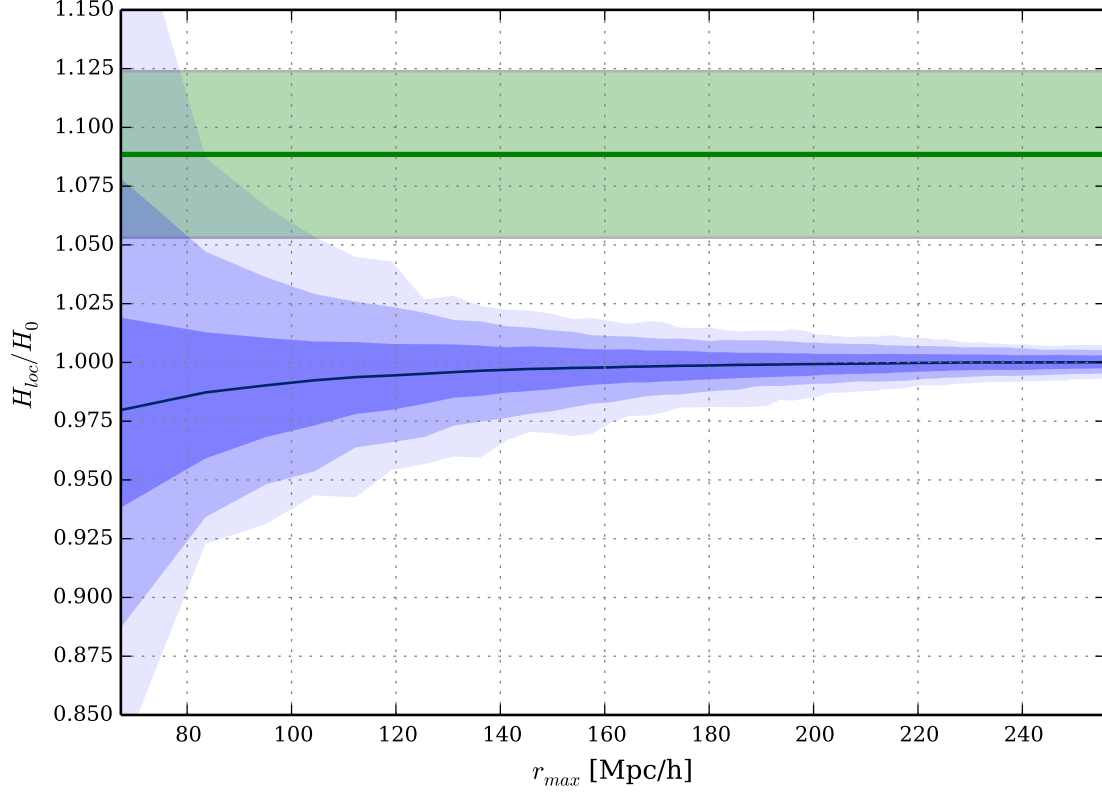


Figure 7.8: The value of the local Hubble parameter found by Riess et al. (green line), is plotted together with the value and spread of H_{loc}/H_0 found in the standard analysis. The green band indicates the 1σ uncertainty in the result from Riess et al.

Figure 7.8 shows the mean and variance of the standard simulation (as in figure 7.3) together with the value of the Hubble parameter found by Riess et al. in [33] of 73.8 ± 2.4 , plotted as a green line, with the uncertainty of the measured value shown as a green band. Only for very small values of r_{max} is there any overlap between the measured range of H_0 and the confidence bands obtained from a Planck like universe. At a distance of $r_{max} = 256 \text{Mpc}/h$, significantly less than 0.3% of the Local Group like observers would observe a value as high as the one we see. We therefore conclude that the variance of the expansion field does not lift the discrepancy between the Hubble constant determined from measurements of the CMB and that obtained by direct measurements of recessional velocities in our local universe. This has also been concluded by Marra et al. in

[41] and by Wojtak et al. in [42]. At an intermediate distance of 150Mpc/h, we find the width of the 63.8% confidence interval for the local Hubble constant to be 0.9% – 1.1% (depending on the simulation), which is in good agreement with the value of 0.9% found by Wojtak et al. We observe a tendency for the local Hubble parameter as measured by observers in halos to be systematically lower than the overall expansion rate, whereas observers distributed randomly in space tends to overestimate H_0 . This can be explained by noting that observers in halos are positioned in in-fall regions as a consequence of ongoing structure formation, whereas observers positioned at random will have a tendency to be located in regions less dense than average, because these take up a greater fraction of the simulation volume than the overdense regions. Both effect are smoothed out when observing halos at large distances. This is in good agreement with the result obtained in [42]. Observers positioned randomly in halos will in mean observe a Hubble constant very close the actual value.

Chapter 8

The local value of H_0 in an inhomogeneous universe

This chapter presents a slightly modified version of the paper [3]. The idea for the paper and the previous studies which it builds on are due to S. M. Kocsbang, while the analysis was carried out by me. The introduction has been largely altered from the introduction of the published paper, in order to introduce the central concepts. Furthermore, a few results, which did not appear in the published version of the paper, but were subsequently obtained upon request from Adam Riess, have been included. Apart from this, only a few minor changes have been made.

[3] Io Odderskov, Sofie Kocsbang, and Steen Hannestad, *The local value of H_0 in an inhomogeneous universe*, JCAP **2016** 02 001.

8.1 Introduction

In the paper presented in the previous chapter, the local variations of H_0 were studied based on mostly Newtonian considerations¹. Furthermore, the local values of H_0 were found by fitting Hubble's law to the exact distances in the $z = 0$ -snapshot and the redshifts found by adding the velocity from the expansion and the peculiar velocity together. Such a treatment (equivalent to the one presented in [42]) neglects a number of aspects that play a role in actual observations:

- We do not observe distances, but luminosities.
- We do not observe velocities, but redshifts.
- We do not observe properties of the sources as they are now, but rather as they were at the time of emission (this was taken into account in the analysis based on lightcone snapshots in our first study).

¹"Mostly" refers to the fact that relativistic effects were incorporated to some degree in the lightcone-analysis, by including the deceleration parameter in the analysis, which, according to [25], is a measure of relativistic effects in the relation between observables.

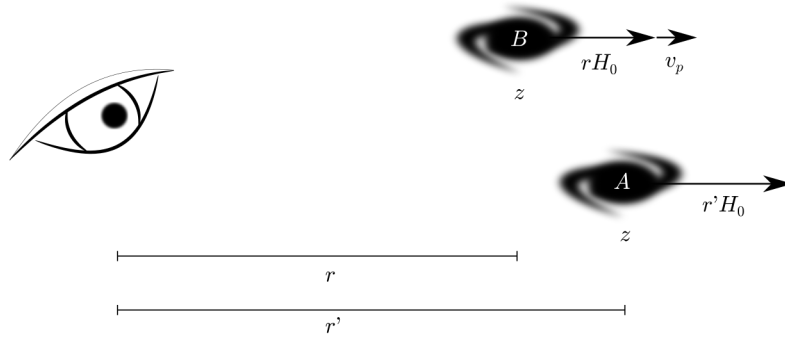


Figure 8.1: The two galaxies are observed to have the same redshift, but since galaxy B is closer to the observer than galaxy A, it looks bigger, that is, it has a smaller angular diameter distance. This is the effect described by the Doppler convergence.

- We do not estimate H_0 based on Hubble's law (as appropriate when observations are carried out in the intuitive way in a $z = 0$ -snapshot).

To assess the combined importance of these effects, an extension of the study presented in the previous chapter was carried out in collaboration with S. M. Koksang. Specifically, instead of calculating the Hubble constant based on the proper distances to the sources, we took care to base our estimates on quantities directly measurable by the observers – namely redshifts and luminosity distances.

In the study presented in this chapter, the effect of peculiar velocities on measured redshifts and luminosity distances were treated using the *Doppler convergence*. As mentioned in section 2.7, the peculiar velocity of a light source affects the measured luminosity distance to the source, D_L , but not the angular diameter distance, D_A . However, this is of course only true as long as we consider objects at a given (proper) distance. Alternatively, one can consider objects at a given redshift. To illustrate this point, we can again consider two galaxies, A and B, but this with the same observed redshift, rather than the same proper distances (see figure 8.1). We will again assume that galaxy A follows the Hubble flow, and galaxy B has a peculiar velocity away from us. The fact that the galaxies are observed to have the same redshift, although the redshift of galaxy B is comprised of both a cosmological *and* a peculiar part, must mean that galaxy B has a smaller cosmological redshift than galaxy A, i.e. galaxy B is at a smaller proper distance, and therefore looks bigger

than galaxy A^2 . The effect can be incorporated into studies of weak lensing, i.e. the magnification and distortion of light sources due to the gravitational field. This is achieved by adding a term describing the effects of the peculiar velocities to the *lensing convergence* (or just *convergence*), κ , which is the part of the weak lensing that accounts for the magnification of light sources, so that the total convergence is comprised of a gravitational term and a Doppler term [52]. At the low distances considered in this study, the gravitational effects on light are negligible, and so the Doppler convergence offers a way to incorporate the effects of peculiar velocities into the study, thereby accounting for the effects of the inhomogeneities not only on the observed redshifts (which are shifted from their cosmological values due to the peculiar velocities), but also on the observed distances.

Section 8.2 below describes how fluctuations in the luminosity distance due to peculiar velocities are computed. After that, section 8.3 gives a description of the mock-observations constructed for the study. Our findings are presented in section 8.4, which include a few results which were not included in the published paper, as they were obtained upon request after the paper had been published. And finally, we summarize and conclude in section 8.5.

8.2 Method for computing redshift-distance relations in N-body simulations at low redshift

In order to study the effects of inhomogeneities on the local measurement of H_0 , mock observations are constructed by computing redshift-distance data points using results from an N-body simulation. The formalism for computing redshift-distance data points is introduced below while practical aspects regarding the N-body simulation are described in section 8.3.

A recipe for going between Newtonian N-body simulations and a relativistic spacetime corresponding to the first order perturbed FLRW metric in the Newtonian gauge was given in [53]. By using N-body data based on exact, inhomogeneous solutions to Einstein's equations, it was in [54, 55] shown that the recipe leads to a very precise reproduction of redshift-distance relations in an inhomogeneous universe as long as the anisotropy of the individual structures is low. The particular procedure for computing redshift-distance relations studied in [55] will be used here. The study in [55] only included mildly non-linear structures, but in relation to the study presented here, a similar precision of the method has been confirmed for density fractions in the range $0.05 \lesssim \frac{\rho}{\rho_{bg}} \lesssim 10$, where ρ_{bg} is the density of the assumed *background*. (The precision of the method for inhomogeneities outside this range has not been studied.) The procedure is therefore expected to yield fairly accurate estimates of redshift-distance relations including effects of inhomogeneities.

The procedure is only summarized below, and the reader is referred to *e.g.* [53, 55] or the other references cited in this section for elaborations.

²This is actually only true up to a given cosmological redshift, due to the factor of $(1+z)^{-1}$ in equation 2.17 for the angular diameter distance. This ensures that the angular diameter distance does not increase indefinitely with redshift, but reaches a maximum around $z \sim 1.5$ [52]. However, we will not encounter any galaxies of a cosmological redshift greater than $z \sim 0.15$.

The observed redshift of a light ray with tangent vector k^α is computed following the definition $z_{\text{obs}} + 1 = \frac{(k^\alpha u_\alpha)_e}{(k^\alpha u_\alpha)_0}$. The subscripts 0 and e indicate evaluation at the spacetime position of observation and emission respectively such that *e.g.* $(u^\alpha)|_0$ is the observer velocity and $(u^\alpha)|_e$ is the velocity of the source. The velocity field is given by $u^\mu = \frac{c}{V}(1, v^i)$, where v^i are the velocity components obtained from the N-body simulation and the normalization factor $V \approx \sqrt{c^2 - a^2(v_r^2 + v_\theta^2 r^2 + v_\phi^2 r^2 \sin^2(\theta))}$ is computed according to the findings of [55].

In a homogeneous FLRW universe, the angular diameter distance corresponding to an observed redshift, z_{obs} , can be calculated from equations 2.13 and 2.17. This will be referred to as the background value of the angular diameter distance, $D_{A,bg}$. The effects of inhomogeneities on the angular diameter distance can be described by the convergence, κ , such that the angular diameter distance along light rays in the N-body simulation is given by $D_A \approx D_{A,bg}(1 - \kappa)$. Once the angular diameter distance is known, the corresponding luminosity distance can be computed using the distance duality relation $D_L = (1 + z_{\text{obs}})^2 D_A$.

At linear level, the convergence is divided into several different contributions including the (integrated) Sachs-Wolfe contributions, a gravitational contribution and a Doppler contribution. In general, the two dominant contributions are the gravitational convergence and the Doppler convergence. As shown in [52, 55, 56], the gravitational contribution to the convergence is, however, irrelevant at low redshifts. Hence, for the purpose of the current study, the angular diameter distance can be computed as $D_A \approx D_{A,bg}(1 - \kappa_v)$, where κ_v denotes the Doppler convergence. The Doppler convergence can be computed by (see *e.g.* [57]):

$$\kappa_v c = \left(1 - \frac{1}{a_{,t}(\eta_0 - \eta)}\right) n^i u_i, \quad (8.1)$$

where $\eta \equiv \int_0^t \frac{dt'}{a(t')}$ denotes conformal time and u_i is the (spatial) velocity of the source. The Einstein convention is used with i running over the spatial indices 1, 2, 3. The vector n^μ is the propagation direction unit 4-vector, *i.e.* $n^\mu \propto k^\mu + \frac{k^\nu u_\nu}{c^2} u^\mu$. It is sufficient to use the background version of n^μ and in that case n^i is the unit vector pointing in the direction from the source to the observer.

In the expression for the Doppler convergence given above, a term due to the peculiar motion of the observer has been omitted. This is justified by noting that the observer velocity can be estimated by measuring the CMB dipole and hence has no consequences when interpreting real observations. Note also that in equation (8.1), the scale factor etc. are evaluated at the spacetime position corresponding to the *observed* redshift z_{obs} , not a background redshift computed with the background metric.

When mock redshift-distance data points have been obtained as described above, they are fitted to the expression for the luminosity distance in an FLRW universe,

$$D_L(z) = \frac{(1+z)c}{H_0} \int_0^z \frac{dz'}{\sqrt{\Omega_{m,0}(1+z')^3 + \Omega_{\Lambda,0}}}. \quad (8.2)$$

When fitting, H_0 is used as fitting parameter while $\Omega_{m,0}$ and $\Omega_{\Lambda,0}$ are fixed to the values used in the N-body simulation.

Before moving on, it should be noted that the Doppler convergence occurs because of the difference between the observed redshift and the redshift obtained from background computations (see *e.g.* [20, 52, 56–58]). The effects of inhomogeneities studied here are therefore effects of peculiar velocities. The peculiar velocities are gravitationally induced by an inhomogeneous energy density and the effects of the peculiar velocities are thus effects of having a spacetime that deviates from the exactly spatially homogeneous and isotropic FLRW spacetimes. This fact will in the following be emphasized by referring to an “inhomogeneous velocity field” instead of “peculiar velocities”.

8.3 Mock observations

This section serves to introduce the construction of the mock observations used for the study. The (mock) observations are based on a Newtonian N-body simulation with cosmological parameters in agreement with the 2013 results from the Planck collaboration [32], *i.e.* the cosmological parameters are set according to $(\Omega_b, \Omega_{\text{CDM}}) = (0.048, 0.26)$ and $(h, \sigma_8) = (0.68, 0.84)$. The simulation is performed using a modified version of the GADGET-2 code [26], with initial conditions generated using a code written by J. Brandbyge [29] based on transfer functions computed using CAMB³ [34]. The simulation is run in a box of side length 512 Mpc/h, containing 512^3 dark matter particles. The simulation is initiated at a redshift of $z = 50$ and run until the present time.

Box size, simulation resolution and source distribution on the sky will not be varied here as it was in [1] shown that such variations have only small effects on the results.

Velocities and positions of sources as well as positions of observers are obtained by identifying these with halos, which are found using the halo-finder ROCKSTAR [30].

As seen in equation (8.1), the velocity fields of the sources are highly important for computing the Doppler convergence. It was demonstrated in [59] that the effects of inhomogeneities on observations will depend on the smoothing scales used to obtain *e.g.* the velocity field from the discrete N-body data. This issue is here overcome by estimating source velocities as the velocities of bound structures, *i.e.* halos, in the simulation. Assuming that galaxies follow the motion of their dark matter host halos, this procedure corresponds to probing the velocity field in the same manner as is done in real observations.

8.3.1 Redshift distribution of sources

The redshift distribution of the sources affects the study; the further away the sources are, the less impact the peculiar velocities have. To understand the significance of the sources’ redshift distribution, two different redshift distribution schemes are used. In one of the schemes, the sources are distributed according to the redshift distribution of the 155 supernovae of the CfA3+OLD sample [51, 60]. The other scheme selects the 155 sources according to a mass weighted distribution, in which each halo in the distance range $30 \text{ Mpc/h} < r < 256 \text{ Mpc/h}$ is selected with a probability

³<http://camb.info/>

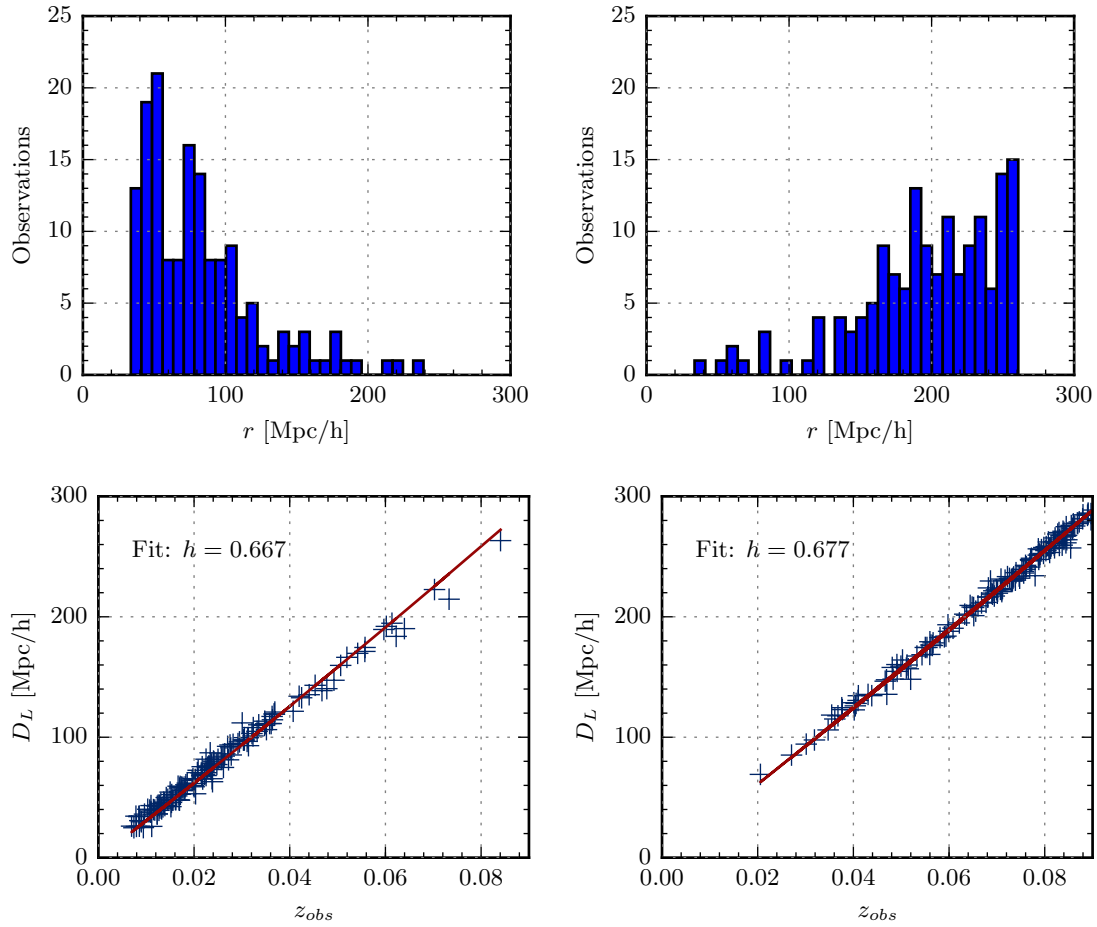


Figure 8.2: **Top:** Distribution of observations as a function of distance. Left: 'Typical' distribution used in estimates of H_0 in the local universe, chosen to correspond to the redshift distribution of the 155 SNe of the CfA3+OLD sample [51, 60]. Right: Mass weighted distribution. **Bottom:** Example of fitting mock observations to equation (8.2) to obtain H_0 , given in terms of the dimensionless Hubble parameter $h = H_0/(100 \text{ km/s/Mpc})$, for the two different redshift distributions.

proportional to its mass⁴. This distribution has the advantage that it is growing as a function of distance (due to the increasing volume of shells). Using this distribution scheme thereby provides a check that the H_0 estimates converge to the true value at large distances. Note also that it is this second scheme that was used in [1].

The difference between the two types of distributions is illustrated in figure 8.2. The figure also shows an example of the differences in H_0 estimates based on observations following the two schemes.

⁴This distribution scheme builds on the assumption that the probability of a type Ia supernova occurring in a given halo is proportional to the halo mass. However, as seen in figure 8.2, the scheme leads to a redshift distribution which is significantly different than the distribution of the CfA3+OLD sample.

8.3.2 Observers

In order to take cosmic variance into account⁵, each set of mock observations are based on a group of observers instead of a single observer. The observer positions are still important for the study as the local environment may bias observations at low and intermediate redshifts. For instance, placing the observers in massive halos amounts to placing them in infall regions and will thus lead to a bias of peculiar source velocities, and hence redshifts, in the direction towards the observer which will again lead to a smaller H_0 estimate. This is predicted by gravitational instability theory [21, Chapter 5], and can in principle be corrected for by subtracting the peculiar motion induced by the local density field when analyzing real observational data (see *e.g.* [61]). Such a correction was for instance made in [33].

In order to study the effects of the local environment of the observers, two different sets of observers are used. The first set consists of observers residing in subhalos of mass $10^{12} - 10^{13} M_\odot/h$ in a host halo in the mass range $5 \cdot 10^{14} - 5 \cdot 10^{15} M_\odot/h$. This approximately corresponds to our position in the Local Group galaxy cluster, a member of the Virgo Super Cluster. The second set of observers are placed at random positions throughout the simulation volume. As underdense regions take up the larger part of the volume, these observers will tend to be positioned in underdense regions.

When observers are placed in halos, their peculiar velocities are taken to be those of the host halos. When they are placed at random positions, they are assumed to be at rest with respect to the background. The observer velocities enter into the computations of the observed redshift and so using these two different methods for estimating observer velocities may affect the results. This has been tested not to be the case though; setting the observer velocities to zero in the case where the observers are placed in halos is insignificant for the results.

8.3.3 Lightcone snapshots

The velocity in equation (8.1) is the comoving velocity of the source at the time of emission. The mock observations are carried out in the halo catalog at $z = 0$. However, comoving source positions change over time due to the sources' peculiar velocities (which also change over time). Since the study made here is based on low-redshift observations with $z \lesssim 0.1$, this cosmic evolution should not affect the results at a significant level. To test this assessment, two types of halo catalogs are made. One is based on a regular GADGET-2 snapshot at $z = 0$, while the other type is based on lightcone snapshots⁶ (one for each observer). ROCKSTAR's lightcone functionality can be used for identifying structures in such a snapshot. In the resulting halo catalog, the positions and velocities are stored as they were at the time of emission.

⁵The term "cosmic variance" is here used to mean the uncertainty in observations due to our ability to only observe the Universe from a single spacetime position.

⁶The lightcone snapshots are created by using a plug-in to GADGET-2 written by Troels Haugbølle. The same plug-in was used in [1].

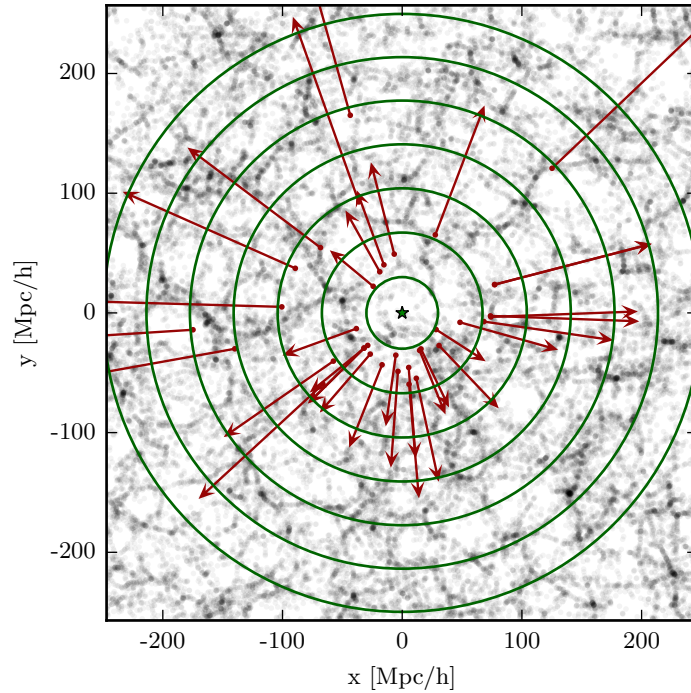


Figure 8.3: Example of the observations carried out by one of the observers (indicated by the green star). The observed halos are colored red, and their total physical velocities relative to the observer are shown with red arrows. The division of redshift bins is illustrated with green circles – only every 5th division is shown.

8.3.4 Summary

In figure 8.3, an example of the observations performed by a single observer is shown. As seen, the observers view the full sky. See *e.g.* [1] for the effects of using smaller sky coverage.

Following the various schemes discussed above, a number of different analyzes have been performed. These are summarized in table 8.1.

Since the lightcone snapshots are very time consuming to use, only a single analysis is made with these. That analysis is denoted Dlc and is the analysis which best resembles real observations.

Figure	Analysis name	Observer positions	SN-distribution	Fit	Lightcone
8.4	Dref	Subhalos	Typical	Full	No
	Href	Subhalos	Typical	Linear	No
8.5	Dlc	Subhalos	Typical	Full	Yes
	Dmw	Subhalos	Mass Weighted	Full	No
	Drp	Random Positions	Typical	Full	No
	Hrp	Random Positions	Typical	Linear	No
	Hmw	Subhalos	Mass Weighted	Linear	No

Table 8.1: Overview of analyzes included in the study. The analysis names are given such that analyzes with H_0 estimates based on Hubble's law ("linear" fit) start with an "H" while those with H_0 estimates based on computing D_L using the Doppler convergence and fitting to the full $D_{L,\Lambda\text{CDM}}$ expression ("full" fit) start with a "D". The last part of the name denotes how each analysis deviates from the reference ("ref") analysis, respectively by using lightcone snapshots ("lc"), using a mass weighted selection of SNe ("mw"), and placing the observers at random positions instead of in halos ("rp").

8.4 Results and discussion

Figures 8.4 and 8.5 show how the local estimates of H_0 are distributed among the observers in the different analyzes. Specifically, the deviation in the local Hubble constant from the true value, $(H_{0,loc} - H_0)/H_0$, is shown as a function of the distance r_{max} to the most distant bin included in the estimate of $H_{0,loc}$. The sources are distributed in bins according to their comoving distances from the observer, which are related to the redshifts of the FLRW background via $r = \frac{c}{H_0} \int_0^z \frac{dz'}{\sqrt{\Omega_{m,0}(1+z')^3 + \Omega_{\Lambda,0}}}$. The mean value of the deviation is shown with a solid line, and the 68.3%, 95.4% and 99.7% confidence intervals are indicated with either shaded areas or dashed lines.

The results are shown using different combinations of choices for the observer positions, redshift distribution of supernovae, and fitting method. An overview of the different combinations that have been studied is given in table 8.1 where a naming scheme for the analyzes is also introduced. The analysis Dlc is the one which is closest to actual observations; it uses observers placed in subhalos with a typical supernova distribution in a lightcone snapshot and obtains H_0 by a fit to the FLRW redshift-distance relation as explained in section 8.3. In figure 8.5, analysis Dlc is compared to analysis Dref which differs from Dlc only in that it is based on a regular GADGET-2 snapshot. As seen, the difference between using the two types of snapshots is negligible.

Figure 8.4 compares analysis Dref to analysis Href. Analysis Href differs from analysis Dref in that H_0 has been obtained using Hubble's law. The comparison shows that the mean H_0 estimate is smaller when Hubble's law is used instead of the recipe based on the Doppler convergence as described in section 8.2. The difference is quite small, ranging from 1.9% in the innermost bin to 0.3% in the outermost bin. A similar result is seen in figure 8.5, *i.e.* the analyzes based on Hubble's law consistently yield a H_0 estimate that is slightly smaller than the estimate of the corresponding analysis based on the Doppler convergence computations described in section 8.2.

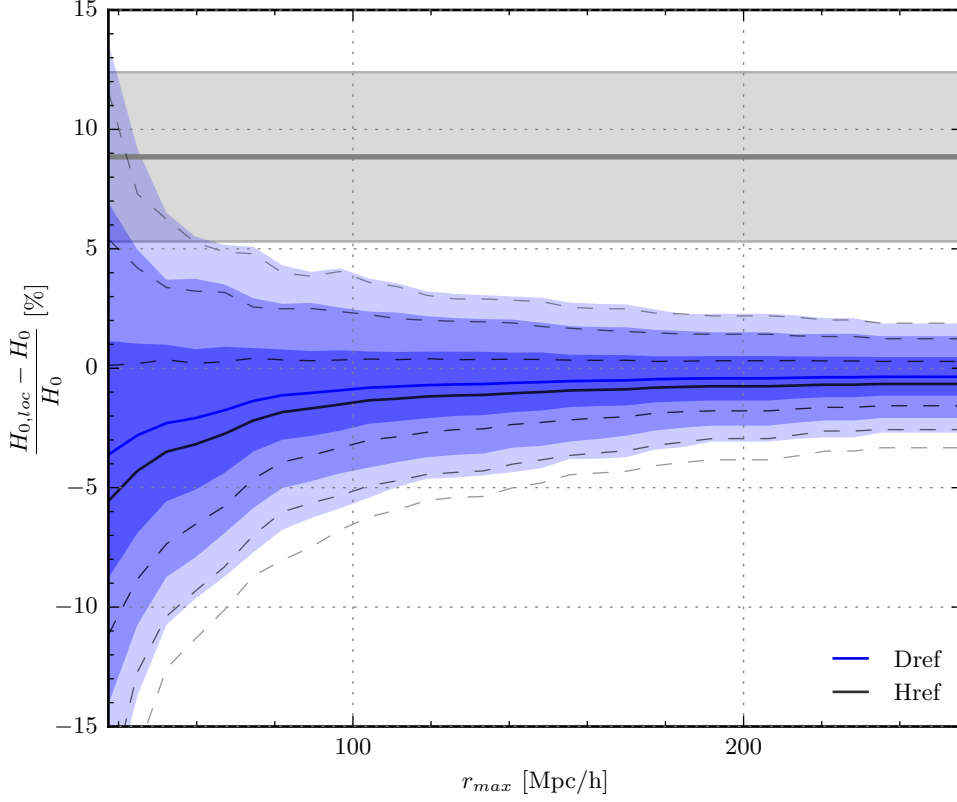


Figure 8.4: Deviations between H_0 of the N-body background and the local values $H_{0,loc}$ of H_0 obtained using the analyzes Dref and Href described in table 8.1. Shadings and dashed lines indicate 68.3%, 95.4% and 99.7% confidence intervals while solid lines indicate mean values. The results are shown as a function of the maximum distance r_{max} between the observer and observed objects included in the H_0 estimates. The gray area indicates the observed value and uncertainty of H_0 found in [33].

Figure 8.5 illustrates the importance of using realistic source and observer distributions. In particular, the figure shows that by changing the observer positions to be random, the H_0 estimates grow. This is because underdense regions take up more of the simulation volume and hence will be favored when using random observer positions. The result can thus be considered a type of Hubble-bubble effect (see *e.g.* [41, 60, 62]). This type of Hubble-bubble result is particularly interesting since there in fact are some indications that we may be living in an underdense region of the Universe [63].

The figure also shows that the distribution of sources has impact on especially the uncertainty of the H_0 estimates. Specifically, the spread in the results is much less when higher-redshift sources are favored in the observations. This is consistent with peculiar motions being less important at larger distances.

Lastly, it is noted that the results presented here yield mean H_0 estimates that are *lower* than

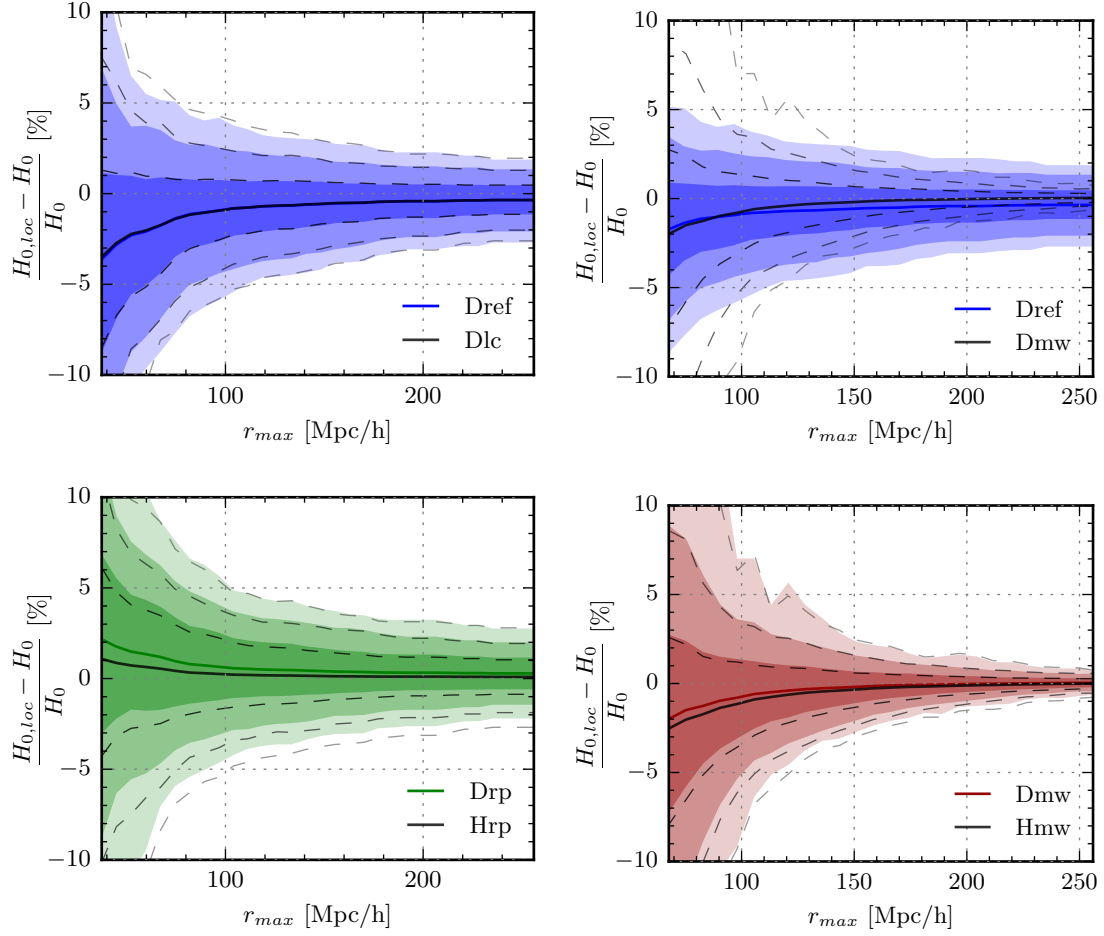


Figure 8.5: Deviations between H_0 of the N-body background and the local values of H_0 obtained using the analyzes listed in table 8.1 as indicated in the figure legends. Shadings and dashed lines indicate 68.3%, 95.4% and 99.7% confidence intervals while solid lines indicate mean values. The results are shown as a function of the maximum distance r_{max} between the observer and observed objects.

the H_0 value of the N-body background. The only exception to this result is the analyzes with random observer positions discussed above. Within the standard cosmological scheme studied here, the effect of peculiar velocity fields thus seems to be to *reduce* the local value of H_0 compared to the global value. Hence, inhomogeneities cannot provide a solution to the tension of different types of H_0 estimates. In fact, the results show that inhomogeneities will in principle increase the tension. As mentioned in section 8.3.2, to the extent that the shift in the mean estimate of H_0 compared to the global value is a result of the local environment at the observer position, this can be corrected for when interpreting real observations.

8.4.1 The local value of H_0 in an inhomogeneous universe based on observations in the redshift range $0.0233 < z < 0.15$

The analysis presented above has been repeated using a redshift distribution of type Ia supernovae ranging from $z = 0.0233$ to $z = 0.15$. This was done upon request from Adam Riess, in order to provide an estimate of the uncertainty in local measurements of H_0 due to the effects of inhomogeneities based on observations similar to those used for the most recent determination of the local Hubble constant, as presented in [35]. We have used the redshift distribution of supernovae in the Union2.1 catalog in the range $0.0233 < z < 0.15$.

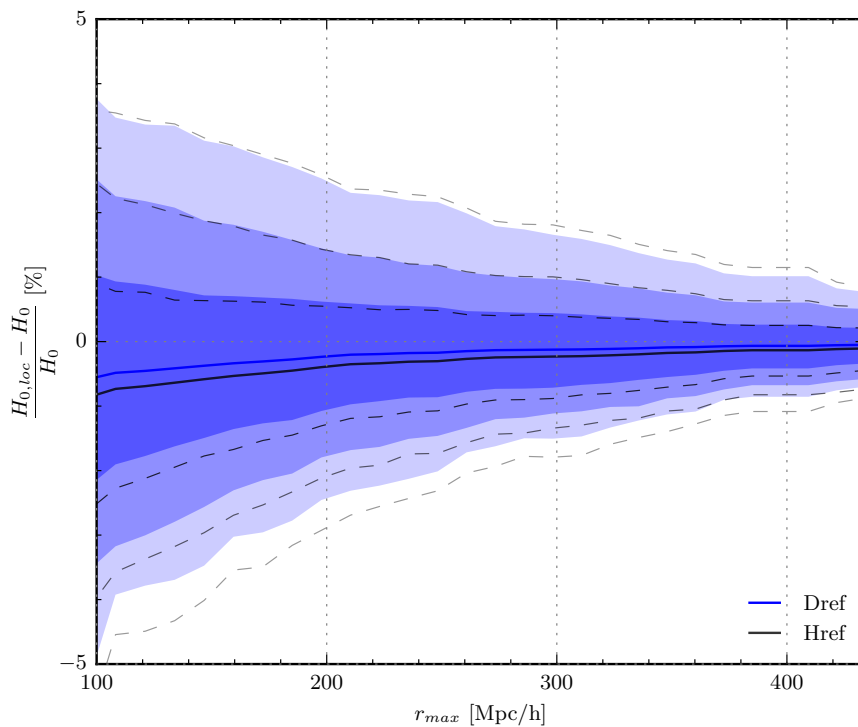


Figure 8.6: Deviations between H_0 of the N-body background and the local values $H_{0,loc}$ of H_0 obtained using Hubble's law (Href) and the Doppler convergence (Dref), based on the redshift distribution of supernovae in the Union2.1 catalog. Shadings and dashed lines indicate 68.3%, 95.4% and 99.7% confidence intervals while solid lines indicate mean values. The results are shown as a function of the maximum distance r_{max} between the observer and observed objects included in the H_0 estimates.

Again, the Hubble constants have been determined using respectively Hubble's law (the analysis marked with an H) and the Doppler convergence (marked with a D). At $z = 0.15$, the Hubble constants obtained using the Doppler convergence are found to be 0.06% higher than those obtained using Hubble's law, when the observers are placed in Local Group like halos, as shown in figure 8.6, and 0.03% higher when the observers are placed at random positions. The width of the 68.3%

confidence interval is found to be 0.27% at $z = 0.15$ – both for observers placed in Local Group like halos, and for observers placed at random positions. When the redshift distribution that peaks at high redshifts is used, the width is found to be 0.16%.

8.5 Summary

N-body simulations were used to study low-redshift determinations of H_0 in an inhomogeneous universe. In particular, it was studied whether or not an inhomogeneous velocity field leads to a local H_0 value different from the global value, the latter corresponding to that of the N-body background and which is what one expects to measure using high-redshift observations such as those based on the CMB. The H_0 values were obtained by approximating light paths according to the background model and computing the angular diameter distance of objects by using the Doppler convergence to take effects of inhomogeneities into account. Inhomogeneities were also taken into account when computing source redshifts. This procedure differs from that used in earlier work of this kind, where H_0 determinations have been estimated by using the linear relation known as Hubble's law. The results obtained with the method introduced here consistently lead to a mean H_0 value which is higher than that obtained by simply using Hubble's law. The difference is, however, very small.

The H_0 estimates were found to be slightly lower than the background value except in a single of the studied cases: When the observers are placed at random positions in the simulation box, the resulting mean H_0 estimate is slightly above that of the N-body background. This result is similar to the Hubble-bubble effect.

As source distances and numbers are increased, all the H_0 estimates converge towards the value of H_0 of the N-body background.

The results summarized above indicate that the tension between high- and low-redshift determinations of H_0 cannot be alleviated by taking inhomogeneities into account – at least not without straying from standard cosmology.

Chapter 9

The effect of interacting dark energy on local measurements of the Hubble constant

This chapter is based on the study presented in [2], which builds on simulations of interacting dark energy carried out by Marco Baldi. It presents an investigation of the variations of the Hubble constant in a set of alternative cosmological models, in which dark energy interacts with dark matter. The study was undertaken as we realized that local fluctuations in the velocity field were significantly larger in such scenarios. The chapter is practically identical to the published paper.

[2] Io Odderskov, Marco Baldi, and Luca Amendola, *The effect of interacting dark energy on local measurements of the Hubble constant*, JCAP **2016** 05 035.

9.1 Introduction

Today, cosmological parameters are being measured with an accuracy of a few percent. This makes it possible to constrain cosmological models by comparing independent estimates with each other under the assumption of some specific model. Recently, this led to questioning the standard cosmological scenario, when the Planck Collaboration found that measurements from the CMB under the assumption of the Λ CDM model led to a surprisingly low value of the Hubble constant, more than two standard deviations from the one measured in the local universe [32, 33]. One possible solution to this that did not challenge the Λ CDM model was that the discrepancy was caused by local variations in the cosmic flow field. This was studied by [1, 41, 42], and found to have an insignificant effect at the distance scales probed by type Ia supernovae. Another possible resolution of the discrepancy, which has been suggested in [39], is that systematics in the calibration of the distance-luminosity relation for type Ia supernovae may lead to an overestimate of the Hubble constant. The calibration used by [33] is primarily based on Cepheids, and the precision of this

calibration both limits the accuracy to which the Hubble constant can be determined and possibly introduces systematics leading to an erroneous estimate.

One of the alternative ways to measure the Hubble constant is to use Cepheids in the Coma Cluster. This would eliminate a step on the distance ladder and the possible error associated with the calibration [64, 65]. But at this much smaller distance, the effect of the local variations is much larger.

Here, we study the local variations associated with a determination of the Hubble constant using Cepheids in the Coma Cluster. We further study the model dependence of this method. This is done using a set of publicly available cosmological simulations and halo catalogs from the CoDECS project¹, which include a coupling between a dark energy scalar field and dark matter particles [66, 67]. We show that the uncertainty associated with the local variations is model dependent, and that the presence of a coupling between dark matter and dark energy would increase the variance among the locally measured Hubble constants by about 1%. A substantially larger fraction of the observers in cosmologies with a strong coupling would significantly over- or underestimate the expansion rate. By performing the same analysis on a standard Λ CDM simulation featuring a high value of σ_8 , we find that most of the effect can be ascribed to the higher value of σ_8 arising in the coupled cosmologies as a consequence of the fifth-force mediated by the dark energy field, in order for them to be consistent with constraints from the CMB. However, this does not account for all of the added variance.

We also test the procedure of subtracting the component of peculiar velocities predicted by gravitational instability theory, and discuss the validity of this approach in the coupled cosmologies. We show that the correction reduces the variance in all the considered cosmologies, when the velocities are smoothed over a sufficiently large radius.

The paper is organized as follows: In section 9.2, we provide a short description of coupled dark energy cosmologies. The simulations and halo catalogs are described in section 9.3. In section 9.4 we describe how the distributions of local Hubble constants are found by identifying mock observers in the halo catalogs, who each carry out a mock observation in order to determine the Hubble constant in their local universe. We also explain the subsequent correction procedure carried out by each observer. In section 9.5 we present and discuss our results, and we conclude in section 9.6.

9.2 Coupled dark energy cosmologies

If the dark energy component of the universe is coupled to some of the matter species, as first proposed in [68], this would provide a possibility for gaining a deeper insight into this mysterious component and to address some of the naturalness problems associated with the onset of the cosmic acceleration. To be able to detect such a coupling, it is essential to understand what imprint it would make on observables, for example the density field and the velocities of its tracers [69, 70].

¹“Coupled Dark Energy Cosmological Simulations”, the halo catalogs are available at <http://www.marcovaldi.it/CoDECS>

The cosmologies considered in this paper are based on an evolving scalar field, playing the role of the dark energy, which couples to dark matter. See [66, 67, 69–74] for further details about the motivation and evolution of such cosmologies. The interaction gives rise to a fifth force, acting between dark matter particles, which is mediated by the dark energy scalar field. This modifies the processes of both linear and non-linear structure formation, and it is therefore natural to consider a possibly important modification of the local variations in the expansion rates found at different positions in the universe.

The coupling modifies the evolution equations for dark matter and dark energy by adding a source term in each of the respective dynamic equations (see [67]):

$$\begin{aligned}\dot{\rho}_c + 3H\rho_c &= -\sqrt{\frac{16\pi G}{3}}\beta_c(\phi)\rho_c\dot{\phi}, \\ \ddot{\phi} + 3H\dot{\phi} + \frac{dV}{d\phi} &= \sqrt{\frac{16\pi G}{3}}\beta_c(\phi)\rho_c.\end{aligned}\tag{9.1}$$

Here, ρ_c is the density of cold dark matter, H is the Hubble constant, G is Newtons gravitational constant, ϕ is the scalar field, $V(\phi)$ is the potential in which it evolves, and the coupling of the scalar field to cold dark matter is described by the coupling function $\beta_c(\phi)$. Overdots denote derivatives with respect to cosmic time. The models considered in this paper are a subset of the ones included in the CoDECS project, corresponding to a set of flat cosmologies with different assumptions about the potential $V(\phi)$ in which the scalar field evolves, and about the coupling function $\beta_c(\phi)$. We use the same naming convention as in the CoDECS project, where the first part of the name of a model describes the form of $V(\phi)$, and the last part describes the strength of the coupling function $\beta_c(\phi)$. The models considered are:

$$\Lambda\text{CDM:} \quad V(\phi) = A \quad ; \quad \beta_c(\phi) = 0, \tag{9.2}$$

$$\text{EXP00[1,3]:} \quad V(\phi) = Ae^{-\alpha\phi} \quad ; \quad \beta_c(\phi) = \beta_0, \tag{9.3}$$

$$\text{EXP008e3:} \quad V(\phi) = Ae^{-\alpha\phi} \quad ; \quad \beta_c(\phi) = \beta_0e^{\beta_1\phi}, \tag{9.4}$$

$$\text{SUGRA003:} \quad V(\phi) = A\phi^{-\alpha}e^{\phi^2/2} \quad ; \quad \beta_c(\phi) = \beta_0, \tag{9.5}$$

with the values of α , β_0 and β_1 given in table 9.1. See [69] for more details about the models with constant coupling (EXP001 and EXP003), [73] for details about the model with variable coupling (EXP008e3) and [74] for details about the SUGRA model.

As shown in [71, 73], the relation from linear perturbation theory relating the density parameter for matter, Ω_m , and the growth rate, $f(a)$: $f(a) = \Omega_m^\gamma$ with $\gamma = 0.55$ [21], no longer holds in coupled models. In [66] it was found that a good fit can be achieved with the formula

$$f(a) \approx \Omega_m^\gamma \left(1 + \gamma \frac{\Omega_c}{\Omega_m} \epsilon_c \beta_c^2 \right), \tag{9.6}$$

where Ω_c is the density parameter for cold dark matter, with $\gamma = 0.56$ and $\epsilon_c = 2.4$. For the models with an exponential potential, EXP001, EXP003, and EXP008e3, the normalization of the scalar field is $\phi(z = 0) = 0$. This means that $\beta_c(z = 0) = \beta_0$ for each of the coupled models.

9.3 Simulations and halo catalogs

The simulations in the CoDECS project have been created using a modified version of GADGET [26]. The implementation of the modifications is described in [66]. The simulations which are used in this study have been run in periodic boxes of 1 Gpc/h, containing 1024^3 CDM particles and the same number of baryon particles, corresponding to particle masses at $z = 0$ of $m_c = 5.84 \times 10^{10} M_\odot/h$ and $m_b = 1.17 \times 10^{10} M_\odot/h$, respectively. The only difference between the two types of particles is that the baryons do not couple to the scalar field. The softening length in the simulations is $\epsilon_s = 20$ kpc/h.

All the simulations share the same set of parameters at the present time, except for the amplitude of density perturbations, σ_8 , which has been normalized to the value it had at the time of last scattering ($z_{CMB} \approx 1100$), in order to be consistent with constraints from the CMB. Therefore, the different growth rates result in different values of σ_8 today.

Ideally, all of the simulations should be run in different versions with different cosmological parameters, in order to check the importance of each of these on the results. However, this is computationally expensive with simulations of these sizes, and beyond the scope of this work. The most important parameter in this regard is σ_8 , which differs much between the simulations and can be expected to be responsible for a large part of the difference in their velocity fields, which causes the local variations in H_0 . For the purpose of distinguishing the effect of σ_8 from separate effects caused by the coupling, we include in the studied models a further realization of Λ CDM in which σ_8 has the same value as in the strongly coupled model, EXP003 (see table 9.1). This model will be referred to as Λ CDM_HS8.

The initial conditions have been created by displacing particles from a homogeneous glass distribution using the Zel'dovich approximation [75], in order to match a random-phase realization of the linear matter power spectrum (assumed to be Gaussian, with a spectral index of $n_s = 0.966$). The simulations were started at an initial redshift of $z_i = 99$. The phase of displacements were chosen to be the same for each model, so that the large scale cosmic structures are the same in all the simulations.

The simulation parameters correspond to the 7th year results of the Wilkinson Microwave Anisotropy Probe [76]: The universe is assumed to be flat, and $h = 0.703$, $\Omega_c = 0.226$, $\Omega_\Lambda = 0.729$, $\Omega_b = 0.0451$. This results in particle masses of $m_c = 5.84 \times 10^{10} M_\odot/h$ for the CDM particles and $m_b = 1.17 \times 10^{10} M_\odot/h$ for the baryons at $z = 0$ (the particle masses vary with redshift in the coupled cosmologies). Only the halo catalogs at $z = 0$ have been used. The parameters are summarized in table 9.1.

The halo catalogs have been generated using the SUBFIND algorithm [77]. First, particle groups were identified by running a Friends-of-Friends algorithm over the CDM particles only,

Model	A	α	β_0	β_1	σ_8
Λ CDM	-	-	-	-	0.809
Λ CDM_HS8	-	-	-	-	0.967
EXP001	0.0218	0.08	0.05	0	0.825
EXP003	0.0218	0.08	0.15	0	0.967
EXP008e3	0.0217	0.08	0.4	3	0.895
SUGRA003	0.0202	2.15	-0.15	0	0.806

Table 9.1: Cosmological parameters for the simulations. The sidelength of the box is 1Gpc/h, the number of particles is $2 \cdot 1024^3$, and $h = 0.703$, $\Omega_c = 0.226$, $\Omega_\Lambda = 0.729$, $\Omega_b = 0.0451$. The spectral index for the Gaussian initial conditions is $n_s = 0.966$, and the normalization of scalar perturbations is $\mathcal{A}_s = 2.42 \times 10^{-9}$.

with a linking length of 0.2 times the mean particle distance. Only groups with at least 32 CDM particles have been retained, and baryonic particles having as nearest CDM neighbour a group member were subsequently attached to the group. Next, gravitationally bound substructures (halos) within the FOF-groups were identified by SUBFIND. In this second step, only halos with at least 20 bound particles (CDM as well as baryons) were kept. The mass of a group or a halo was calculated as the sum of the masses of all the particles it contains.

9.4 Method

Using the halo catalogs of the N-body simulations described above, we estimate the distribution of Hubble constants that would be observed by observers who find themselves in a position in the universe similar to ours. The spread of this distribution contributes to the uncertainty associated with the method.

Mock observers and observations

We use the halo catalogs from the CoDECS project, described in the previous section, to mimic the observations of the Coma Cluster. At first, in each simulation we choose 1000 observers with a position which has the same characteristics as our position in the universe. This is done by identifying the halos with a mass similar to that of the Local Group (in the mass range $1 \times 10^{12} - 1 \times 10^{13} M_\odot/h$) which are subhalos of a group with a mass similar to that of the Virgo Supercluster (in the mass range $5 \times 10^{14} - 5 \times 10^{15} M_\odot/h$). Each observer makes an observation of a halo at a distance of 65 – 75Mpc/h. Since $h = 0.703$, this corresponds to the distance to the Coma Cluster (99Mpc = 70Mpc/h). The observer then estimates the Hubble constant from the measured distance, r , and radial velocity, v_r , of the halo as

$$H_{loc} = \frac{v_r}{r}. \quad (9.7)$$

The velocity is the sum of the velocity due to the expansion, given by $H_0 r$, and the radial part of the peculiar velocity of the halo. This corresponds to the velocity that would be deduced from the

measured redshift.

The peculiar velocities are generally assumed to be generated by the process of structure formation. This can be described using linear perturbation theory, as will be further discussed in the next section. However, this is only valid when the matter distribution is smoothed on sufficiently large scales. The Cepheids at the center of the Coma Cluster are assumed to be at rest with respect to the cluster, and therefore follow its overall motion,² which can be found as the center of mass motion of its constituents. In order to make the observations in the mock catalogs fit the observation of the Coma Cluster as accurately as possible, we measure these velocities in the following way: Each observer starts by identifying the most massive halo in the chosen distance range, and subsequently finds all halos within a radius R of this halo. Then, the center of mass velocity of this group of halos is calculated, which corresponds to smoothing the velocity field on a scale given by R . We investigate how the results depend on the scale by using different radii for the calculation of the center of mass motion, ranging from $R = 0$, equivalent to no smoothing, to $R = 15 \text{ Mpc}/h$, which is significantly larger than the radius of the Coma Cluster.

The observation carried out by each observer is illustrated in figure 9.1.

Correcting for local flows

In [79], the observed velocities are corrected by subtracting the predicted velocity as calculated from a sum over the nearby attractors (The Virgo Supercluster, The Great Attractor and the Shapley Concentration [79, 80]). Thanks to large galaxy surveys and improved computer resources, today it is possible to integrate the entire density field in the nearby universe, at least to the degree that it can be accurately probed by tracers such as galaxies. This approach is for example described in [61] using the IRAS PSCz galaxy redshift survey.

The predictions for the local flows are found by applying linear perturbation theory to the density field. As well known [21], the peculiar velocity at a position \mathbf{r} is related to the gravitational field through

$$\mathbf{v}(\mathbf{r}) = \frac{2}{3} \frac{f(\Omega)}{\Omega_m H(z)} \mathbf{g}(\mathbf{r}), \quad (9.8)$$

where Ω_m is the density parameter for matter, $H(z)$ is the Hubble constant at redshift z , and $f(\Omega)$ is the growth rate. The gravitational field $\mathbf{g}(\mathbf{r})$ can be found by integrating the overdensity $\delta_m(\mathbf{r}) \equiv \frac{\rho_m(\mathbf{r}) - \bar{\rho}_m}{\bar{\rho}_m}$, where $\rho_m(\mathbf{r})$ is the matter density at position \mathbf{r} , and $\bar{\rho}_m$ is its mean value:

$$\mathbf{g}(\mathbf{r}) = G\bar{\rho}_m \int \frac{\mathbf{r}' - \mathbf{r}}{|\mathbf{r}' - \mathbf{r}|^3} \delta_m(\mathbf{r}') d^3\mathbf{r}'. \quad (9.9)$$

The overdensity field can be related to the halo overdensity field as $\delta_h = b_h \delta_m$, where b_h is the halo bias. Using this, and combining the two equations above, it is found that the peculiar velocity from linear perturbation theory at position \mathbf{r} is given by

²This assumption might be problematic, as results from large scale surveys indicate that central galaxies might not be at rest at the halo centers. See for example [78].

$$\mathbf{v}(\mathbf{r}) = \frac{H(z)f(\Omega)}{4\pi\bar{\rho}_m b_h} \int \frac{\mathbf{r}' - \mathbf{r}}{|\mathbf{r}' - \mathbf{r}|^3} \delta_h(\mathbf{r}') d^3\mathbf{r}', \quad (9.10)$$

where we have also used the Friedmann equation, $H^2(z) = \frac{8\pi G}{3} \frac{\rho_m}{\Omega_m}$. It is assumed that the monopole term of the integral does not contribute, as will be the case if the integral is over all of space or over a sphere around the halo at position \mathbf{r} . The density field of the halos in the simulation can be represented as a sum of delta functions at the halo positions, and thereby the expression above turns into

$$\mathbf{v}(\mathbf{r}) = \frac{H(z)f(\Omega)}{4\pi\bar{\rho}_m b_h} \sum_i \frac{\mathbf{r}_i - \mathbf{r}}{|\mathbf{r}_i - \mathbf{r}|^3} m_i, \quad (9.11)$$

where m_i is the mass of the i th halo. In our analysis, we assume $b_h = 1$. We use the growth rates given in equation 9.6.

Linear perturbation theory only gives an accurate description of the velocity field when it is smoothed with a sufficiently large smoothing radius. When the smoothing scale R is small, a massive halo just outside the observed sphere (the blue circle in figure 9.1) will lead to extreme predictions for the velocity, due to the distance in the denominator of equation 9.11. Such velocities will be only weakly correlated with the actual velocities, because they are determined by processes that are not captured by linear perturbation theory, such as virialization. In these cases, the correction procedure will lead to estimates of the Hubble constant very far from the true value. Therefore, the correction procedure can be expected to give very bad results in the case of a small smoothing scale.

Due to the intimate relation between the density field and the peculiar velocity field, the amount of clustering, measured by σ_8 , can be expected to significantly affect the results. This issue is also discussed in [81], where the effect of interacting dark energy on redshift space distortions is studied, and found to be strongly degenerate with the value of σ_8 at scales larger than 5 – 10 Mpc/h. Since the scale considered in this study is much larger than this (~ 70 Mpc/h), we expect our results to be strongly dependent on the values of σ_8 featured in the different models.

Distribution of local Hubble constants

The difference in the measured Hubble constants at different locations in the universe is a consequence of the inhomogeneities in the matter distribution, which induces peculiar velocities. The matter distribution, described in terms of the overdensity parameter, $\delta_m = \frac{\rho_m(\mathbf{r}) - \bar{\rho}_m}{\bar{\rho}_m}$, is necessarily characterized by a skewed distribution, since the allowed values of δ_m ranges from -1 to ∞ . In agreement with this, it has been found that it is well described by a log-normal distribution [82]. As in [41], we assume that local Hubble constants follow the same distribution as the inhomogeneities in the matter distribution, since this is the source of the variations in the Hubble constants. Therefore, we fit the distribution of local Hubble constants in the simulations by a log-normal distribution:

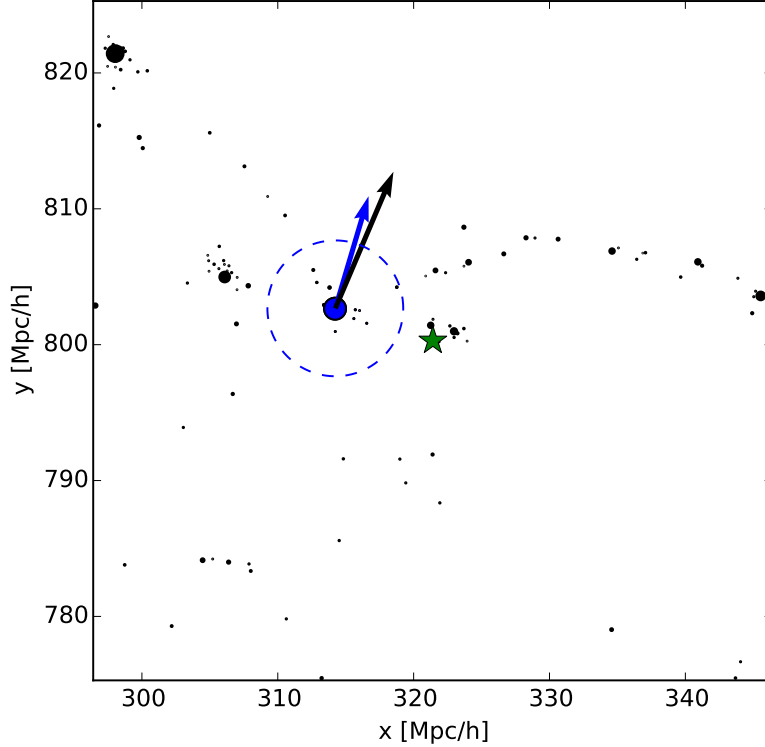


Figure 9.1: An illustration of the observation performed by each observer. The observer is marked with a green star. It chooses the most massive halo in the distance range $65 - 75$ Mpc/h. The peculiar component of the center of mass motion of all halos within $R = 5$ Mpc/h (in the case displayed above) is then calculated (blue arrow), and the radial part is used for the estimation of the Hubble constant. The black arrow is the velocity calculated with equation 9.11. The slice is 10 Mpc/h thick, and is centered on the observer.

$$f(x) = \frac{1}{x\sigma\sqrt{2\pi}} \exp\left[-\frac{(\ln x - \mu)^2}{2\sigma^2}\right], \quad (9.12)$$

where in our case $x = H_{loc}/H_0$. The mean and spread of $\ln(x)$ are given by the fitting parameters μ and σ . In table 9.2, we show the corresponding mean and spread of x , namely $\mu_x = e^\mu$ and $\sigma_x = \mu_x \cdot \sigma$, where the last part follows from the law of propagation of errors.

9.5 Results and discussion

In figure 9.2, we show the distributions of the Hubble constants measured by the different observers in each of the considered models. For each model, we show both the original (blue) and the

corrected (green) distribution, which is obtained by subtracting the peculiar velocity predicted by linear theory, equation 9.11, before calculating the Hubble constant. Each model is compared to the distributions in the standard Λ CDM model, which are indicated in magenta. We have chosen a smoothing radius $R = 5 \text{ Mpc/h}$, since this approximately corresponds to the size of the Coma Cluster.

The dependence on the smoothing length is illustrated in figure 9.3, where the corrected and uncorrected distributions are shown for smoothing radii of 0, 1 Mpc/h, 5 Mpc/h, and 10 Mpc/h, respectively, for the EXP003 model.

The parameters for the fitted distributions are given in table 9.2. Before correcting for the linear flows, the models with a strong coupling (EXP003 and EXP008e3) show a spread in the locally measured Hubble constants between 0.6% and 0.8% larger than the spread found in the Λ CDM model. It is perhaps even more interesting to consider the tails of the histograms. A substantial fraction, 13.4%, of the observers in the Λ CDM model would over- or underestimate the Hubble constant by more than 5%, and this number increases to respectively 24.4% and 22.9% in the cosmologies with a strong coupling. The distributions in the weakly coupled cosmologies are very close to the one found for Λ CDM.

For the case of the Λ CDM_HS8 model, featuring a high value of σ_8 , the distributions are very similar to those found for EXP003, which has the same value of σ_8 . This is shown in figure 9.4, in which the fitted distributions for EXP003, Λ CDM, and Λ CDM_HS8 are compared. This indicates that most of the difference between the coupled and uncoupled models can be attributed to the different values of σ_8 . There is, however, a small residual difference. This is most notable when considering the tails of the histograms: The fraction of observers who over- or underestimate the Hubble constant by more than 5% is a few percent higher in the EXP003 model than in the Λ CDM model with the same value of σ_8 . Furthermore, the model with a variable coupling, EXP008e3, also has a wider distribution than Λ CDM_HS8, despite having a lower value of σ_8 . This is similar to the results presented in [83], in which the pairwise infall velocity of clusters is found to be greatest in the simulation which features a variable coupling. In [83], this result is further investigated by considering the first order equations from [71] for the density and velocity perturbations in coupled dark energy models. By solving these, it is shown that the biggest perturbations in the peculiar velocity field at $z = 0$ are found in the exponentially coupled model, even though the corresponding enhancement of the density perturbations (as measured by σ_8) is significantly smaller than in the EXP003 model. Hence, this result is in agreement with what one should expect from linear perturbation theory.

When varying the radius used for the CoM calculation, we see that increasing the radius generally leads to better results for the correction procedure. This is expected, as velocities on larger scales will be better approximated by linear perturbation theory. However, when the CoM-scale is increased to 15Mpc/h, the correction procedure becomes less effective. We attribute this to the effect of the finite box size. It is seen that the correction slightly underestimates the peculiar velocity caused by the presence of the halo in which the observer is situated, by the fact that also

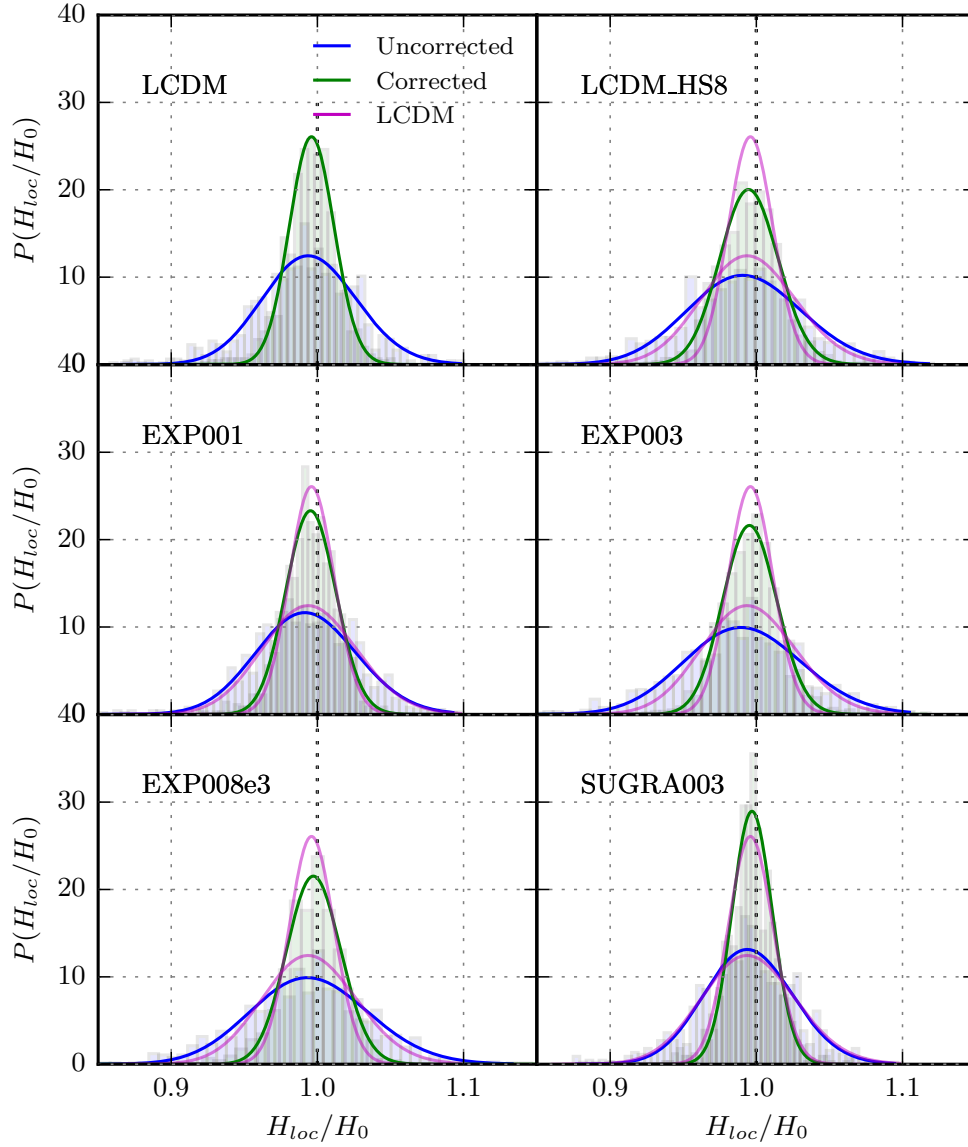


Figure 9.2: The distribution of the measured Hubble constants among the halos with characteristics similar to that of the local group in each of the considered models. The CoM scale is $R = 5 \text{ Mpc}/h$ in all cases. The blue histograms corresponds to the uncorrected distributions, the green histograms to the corrected distributions. The lines are the fitted log-normal distributions. The fitted distributions for the Λ CDM model are shown in magenta for comparison.

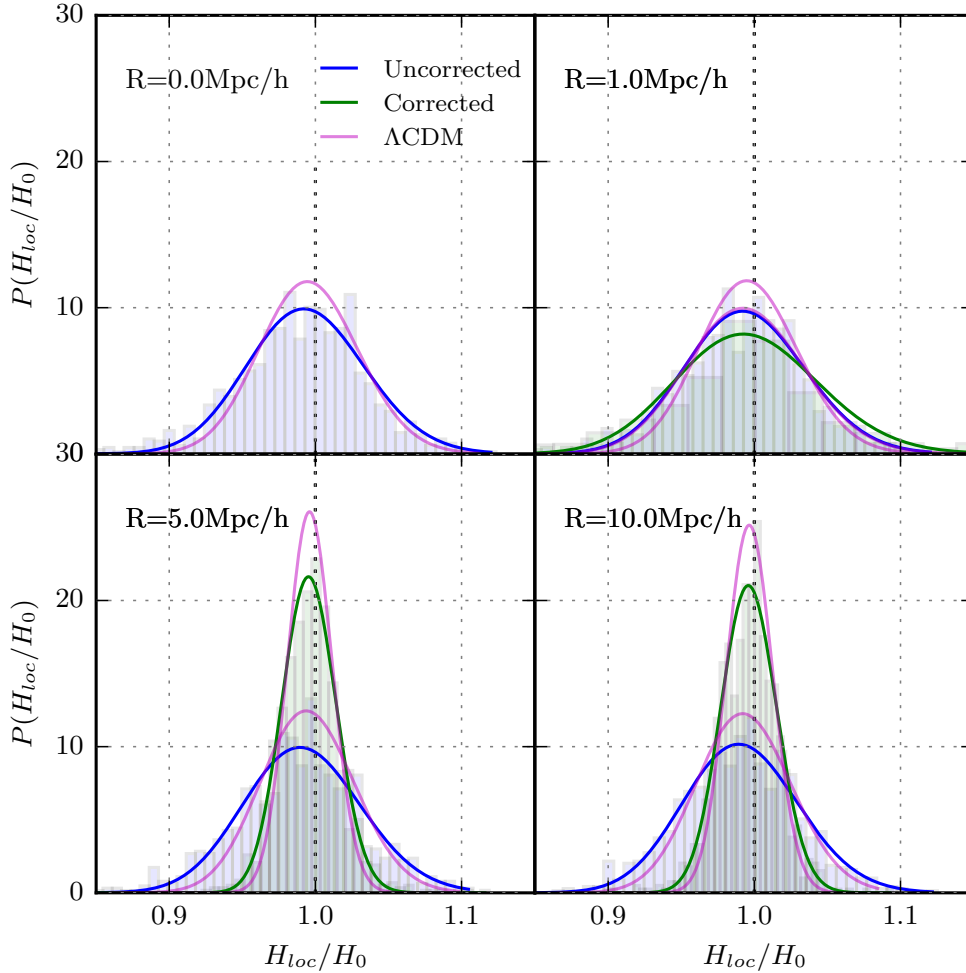


Figure 9.3: The distribution of the measured Hubble constants among the halos with characteristics similar to that of the local group in the strongly coupled model (EXP003). The blue histograms are the distributions before the correction procedure is applied, the green histograms corresponds to the corrected distributions (not shown for the case without any smoothing, $R = 0$). The lines corresponds to the fitted log-normal distributions. The fitted distributions for the Λ CDM model are shown in magenta for comparison.

the corrected distribution has a mean value less than one. This might be caused by the choice to set the halo bias b_h equal to one. Apart from this, the correction procedure efficiently reduces the spread of the distribution for both the standard and the coupled cosmologies. It is also seen that linear theory only reduces the uncertainty at scales above a couple of Mpc. However, structures

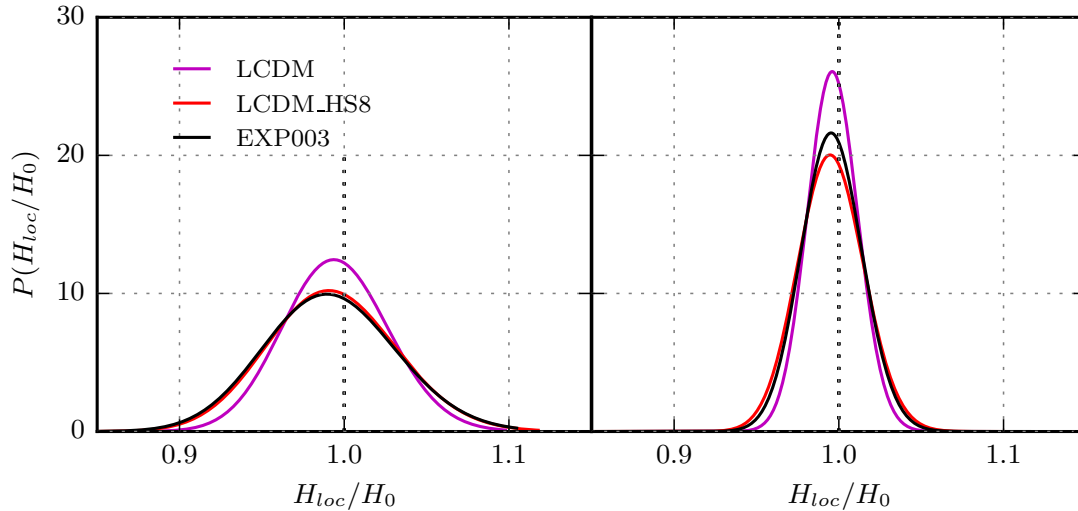


Figure 9.4: Comparison between fitted distributions for uncorrected (left), and corrected (right) distributions of the locally measured Hubble constants. It is seen that most of the difference between the distributions found in Λ CDM and in EXP003 can be attributed to the higher value of σ_8 in the coupled model.

of a size similar to that of the Coma Cluster (with a radius a little above 5Mpc/h) have a peculiar motion which appears to be well described by this theory.

Future studies might include a more thorough exploration of the peculiar velocities in coupled cosmologies. This subject is also treated in [84], where differences in the pairwise velocity distributions of the coupled cosmologies are explored. It is briefly discussed how the effects of the coupling compares to the effects caused by the existence of massive neutrinos. The signature from massive neutrinos points in the opposite direction of the change caused by the coupling [85]. Therefore, if massive neutrinos were present, this could allow for a large coupling. And since the coupling causes a larger variance, this could potentially explain a discrepancy between the Hubble constant estimated from the CMB and the value measured in the local universe. In the most strongly coupled model considered here, EXP003, 0.8% of the observers would measure a local Hubble constant more than 8.8% higher than the true value, corresponding to the discrepancy between the local and the CMB value. This is 4 times as many as in the Λ CDM case (0.2%). However, the corresponding fraction in the Λ CDM_HS8 model is also 0.8%, which confirms that the higher value of σ_8 is responsible for most of the additional variance.

Model	σ_8	R	μ_x	σ_x	$P(\frac{H_{loc}}{H_0} < 0.95)$	$P(\frac{H_{loc}}{H_0} > 1.05)$
Λ CDM	0.809	0.0	99.6 (-)	3.4 (-)	10.8 (-)	5.3 (-)
		1.0	99.6 (99.4)	3.4 (4.0)	10.4 (17.3)	4.7 (7.7)
		5.0	99.5 (99.6)	3.2 (1.5)	10.3 (1.6)	3.1 (0.6)
		10.0	99.3 (99.7)	3.3 (1.6)	9.9 (1.2)	4.7 (0.2)
		15.0	99.2 (99.7)	3.3 (1.8)	11.3 (1.5)	4.4 (0.6)
EXP003	0.967	0.0	99.3 (-)	4.0 (-)	17.7 (-)	7.3 (-)
		1.0	99.4 (99.5)	4.1 (4.9)	18.0 (23.6)	8.0 (16.2)
		5.0	99.1 (99.6)	4.0 (1.8)	17.0 (1.5)	7.4 (1.4)
		10	99.1 (99.6)	3.9 (1.9)	18.0 (1.5)	5.8 (0.4)
		15	99.2 (99.7)	4.0 (2.1)	14.7 (3.5)	6.0 (1.4)
Λ CDM_HS8	0.967	5.0	99.2 (99.6)	3.9 (2.0)	15.3 (2.3)	6.3 (0.7)
EXP001	0.825	5.0	99.3 (99.6)	3.4 (1.7)	10.1 (1.8)	3.1 (0.4)
EXP008e3	0.895	5.0	99.5 (99.8)	4.0 (1.9)	15.8 (3.0)	7.1 (0.9)
SUGRA003	0.806	5.0	99.5 (99.7)	3.0 (1.4)	9.8 (1.3)	3.8 (0.4)

Table 9.2: Parameters for the fitted distributions (mean and spread of $x = H_{loc}/H_0$), and the probabilities of measuring a Hubble constant which deviates from the true value by 5% or more, as calculated directly from the histograms. The numbers in the parentheses are the parameters after correcting for the linear velocities induced by the matter distribution. These are omitted for the case of no smoothing, $R = 0$, as non-linear velocities completely dominates in this case. All the numbers are in percent, except for the CoM-scale, R, which is in Mpc/h, and σ_8 .

9.6 Conclusions

We have investigated local variations in the Hubble constant as measured from Cepheids in the Coma Cluster, using a set of simulations featuring a coupling between a dark energy scalar field and dark matter, as well as two Λ CDM simulations with different values of σ_8 . In the standard Λ CDM model, a substantial fraction of the observers (more than 13%) would over- or underestimate the Hubble constant by more than 5%. The variance is found to be much larger in the strongly coupled models, such that almost twice as many observers measures a Hubble constant which deviates substantially from the true value. Most of the added variance was found to be attributed to the higher value of σ_8 in the coupled models. However, especially in the model featuring a variable coupling, there is a residual effect that cannot be explained by σ_8 .

We have tested how the distributions of local Hubble constants are affected by correcting for peculiar velocities induced by the matter distribution, as predicted by linear theory of structure formation, also taking into account the modified relation between density and velocity arising in interacting Dark Energy cosmologies. The correction procedure effectively reduces the spread in the distributions in both standard and coupled cosmologies. And although the fraction of observers who would significantly over- or underestimate the Hubble constant is still much larger in the coupled cosmologies after the correction procedure, it is less than 4% in all the considered cosmologies for a smoothing radius of 5 Mpc/h.

Part III

Realistic forecasts of SNe Ia observations for measurements of the peculiar velocity field

Chapter 10

Imprints of the velocity field on type Ia supernova observations

As discussed in chapter 6, type Ia supernova are some of the best probes of the expansion history of the universe, thanks to their high intrinsic luminosity and the possibility of determining it from the shape of the supernova light curve. However, as we have also discussed, the light from type Ia SNe does not only carry information about the expansion history. For example, the light we receive from distant supernovae is lensed and redshifted by the gravitational fields of structures it has passed through [20, 58]. Such effects are negligible for supernovae at small distances, as the light we receive from these has not passed through many structures. But in this regime the peculiar velocities – typically a few 100 km/s – account for a significant fraction of the measured redshift. In part II, it was examined how large an uncertainty these effects induce on the Hubble constant measured in the local universe. As shown in for example [20, 47, 61, 86], the imprints from inhomogeneities on measured redshifts and luminosity distances also lead to biased estimates for other cosmological parameters, such as the dark energy equation of state, which determines whether the density of dark energy is truly constant as the universe expands.

But the imprint from large scale structure on luminosity distances and redshifts can also be used as a signal in itself. In [58, 87], it was explored how the correlations in the luminosity distances of distant supernovae can be used to measure cosmological parameters. Our purpose is to investigate the potential for using observations of type Ia supernovae at *low* redshift as a cosmological probe. By assuming a specific expansion rate, the luminosity distances and redshifts can be used to determine the peculiar velocities of the observed galaxies [19]. And since these are created by the gravitational attraction of overdensities, they can be used to probe the matter distribution in the local universe and its associated parameters [88–91].

10.1 The power spectrum of the peculiar velocity field

The theoretical predictions for the peculiar velocity field are provided by gravitational instability theory, which describes how structures grow in response to small perturbations in the density

field (see for example [24, chapter 14]). The comoving velocity field, $\mathbf{v}(\mathbf{x}) = \dot{\mathbf{x}}$, describes the peculiar velocity of a mass element at each position, and the density field is described using the overdensity parameter, $\delta(\mathbf{x}) = \frac{\rho(\mathbf{x}) - \rho_0}{\rho_0}$, which was introduced in chapter 3. According to gravitational instability theory, these fields are related via the continuity equation, $\frac{\partial \delta}{\partial t} + \nabla \cdot \mathbf{v} = 0$.

Using peculiar velocities is a promising way to measure cosmological parameters associated with the matter distribution, and offers an independent check of parameters determined from other methods. Since the matter distribution is observed through its gravitational influence alone, the method is unaffected by galaxy bias. Furthermore, selection effects play a much smaller role than in galaxy surveys, since the velocity field is being measured directly instead of being summed up by number counting of galaxies.

How the peculiar velocity field depends on cosmological parameters can be deduced from the continuity equation. In chapter 3, it was found that this could be expressed in terms of the growth rate, f , as $\nabla \cdot \mathbf{v} = -Hf\delta$. By taking the Fourier transform of this, the component of the velocity field stemming from density perturbations of wavelength $\frac{2\pi}{k}$ and direction $\hat{\mathbf{k}}$ is seen to be

$$\mathbf{v}_{\mathbf{k}}(a) = -\frac{ifH\delta_{\mathbf{k}}(a)}{k}\hat{\mathbf{k}}. \quad (10.1)$$

The occurrence of k in the denominator shows that the velocity field is more sensitive to clustering on large scales than the density field. This means that analysis of the velocity field makes it possible to study clustering on larger scales than can be reached using direct measurements of the matter distribution.

In section 3.1, the power spectrum of density fluctuations was introduced as $P(\mathbf{k}) = \frac{1}{V}\langle|\delta_{\mathbf{k}}|^2\rangle$. From equation 10.1, the power spectrum of the perturbations of the velocity field, $P_v(k) \equiv \frac{1}{V}\langle|\mathbf{v}_{\mathbf{k}}|^2\rangle$, is then found to be related to the matter power spectrum via

$$P_v(k) = H^2 f^2 k^{-2} P_m(k). \quad (10.2)$$

As we saw in section 3.3, the growth rate is a function of the matter density of the universe; hence this is one of the parameters that can be obtained from studies of the velocity field. Likewise, the close relation between $P_v(k)$ and $P_m(k)$ implies that parameters associated with matter power spectrum, such as its shape and amplitude, can be determined from such studies.

Since equation 10.2 has been derived from linear theory, the peculiar velocity field and the density field should both be smoothed over non-linear scales. The velocity deduced from the redshift of a galaxy is already smoothed on the scale of the galaxy. And we will further smooth the velocity field to remove the effect of the limited resolution, which is determined by the actual distribution of supernovae.

If all three components of the peculiar velocities could be observed, the equation above relating the 3D power spectra of the density field and the velocity field could be directly used for parameter estimation. However, this is not the case: The velocities are measured from the redshift of the observed galaxies, and therefore, only the radial component can be measured. For this reason, a more suited observable than the 3D velocity power spectrum is the 2D power spectra of the radial

peculiar velocities in shells at different redshifts. With the current sample of type Ia supernovae, only the lowest multipoles can be reliably estimated [43, 48]. However, this will change in the near future with the large sample of type Ia supernovae to be collected in the LSST sky survey. To investigate how well the multipole expansion can be determined from the low-redshift type Ia supernovae observed by the LSST, we have created realistic mock catalogs of the type Ia supernova rates in galaxies in the present day universe. These have been created by running large dark matter N-body simulations, and calculating the rate of type Ia supernovae based on the star formation histories in halos, which we obtain by using a code for semi-analytical galaxy formation. The next two chapters are dedicated to a description of the way we have modeled galaxy formation and type Ia supernovae in order to create the mock catalogs. In the last chapter of this part of the thesis, we present the results from the simulations and the reconstruction of the velocity field from the mock supernova data.

Chapter 11

Semi-analytical galaxy formation

This chapter is dedicated to a presentation of semi-analytical methods for modeling galaxy formation (SAMs). Initially, a general introduction to the primary elements of the method is given. In the following sections, the various components of semi-analytical modeling of galaxy formation are described in more depth, as we introduce and describe the specific codes we have used.

11.1 The two stages of galaxy formation

In 1978, White and Rees proposed a two stage model for the formation of galaxies [92]. They reasoned that the details of how baryonic material evolves due to non-gravitational forces do not have any significant effect on the large scale clustering of matter, but only become important for matter distribution on much smaller scales, deep within the dark matter halos where galaxies form. Therefore, the formation of halos and the evolution of gas, stars, and galaxies within them can be treated as two separate processes.

The first stage is the formation of dark matter halos: At high redshifts, dark matter formed small halos, which subsequently clustered in a hierarchical way to form the distribution of dark matter halos seen in the universe today. The history of how the individual halos formed through mergers with other halos is called the halo merger tree.

The second stage follows the evolution of baryonic material, which fell into the dark matter halos after recombination. This heated the gas, which became pressure supported and the collapse stalled. But as the hot gas subsequently cooled, it contracted and fell to the center of the halos, where galaxies were formed. As some of the gas fragmented into stars, stellar winds and supernovae injected energy into the gas which had not yet formed stars, thereby ejecting much of this residual gas.

Since much of the physics behind these baryonic processes is poorly understood (in contrast to the formation and evolution of the dark matter halos), these processes are modeled by using several different recipes for describing the various aspects of the formation of stars and galaxies. The recipes used for handling each of these components contain parameters, which are set by

demanding that some observables of the galaxy population are reproduced. We will see some examples of how different processes are modeled later in this chapter.

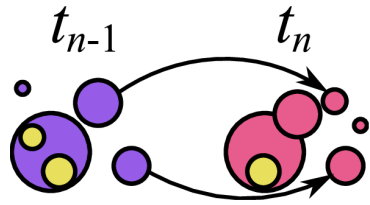
The amount and distribution of hot and cold gas in the halos, which determines the rate with which galaxies and stars are formed, depends both on the internal structure of the halos, as described by their density profiles and angular momenta, as well as their merger history [93]. The catalogs and merger histories of the halos can for example be constructed using a Monte-Carlo approach, by sampling the distribution of progenitor masses predicted by the extended Press-Schechter theory [93]. We will instead use a so-called “hybrid” SAM [94], in which the merger trees are extracted from a dark matter N-body simulation.

11.2 Stage 1: Merger trees

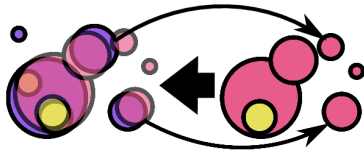
The extraction of halo merger trees from N-body simulations is performed by first identifying halos in snapshots created at several different times, and then determining the probable formation history for the individual halos by comparing halo catalogs at adjacent times to each other. To construct the halo catalogs, we use the halo finder ROCKSTAR [30], which, as described in chapter 5, identifies halos by grouping particles according to their distances in phase-space.

When the halo catalogs have been generated for all the simulations, they are fed to the Consistent Trees code [95]. This code solves a number of non-trivial problems associated with the construction of merger trees. For example, a subhalo that passes close to the center of its host at one time step can be identified as having merged with its host. But if it then reappears at the next time step, it is identified as a new halo with no merger history. A failure to treat such situations will lead to incorrect predictions for the galaxies residing in the halos. Halos close to the threshold of identification pose problems as well: They may appear and disappear many times, which can result in false mergers and halos with no merger history [95]. To handle such problems, each time a halo is not found near its predicted location, the tidal field experienced by the halo is calculated. If a nearby halo exerts strong tidal forces on the halo in question, there is a good chance that it has been ripped apart and its particles have been engulfed by the other halo. A threshold tidal field is therefore defined, which is used to determine whether the halo is most likely to have been disrupted or fluctuated below the threshold of detection.

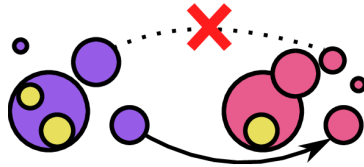
The algorithm used by Consistent Trees to determine the merger histories of the halos is illustrated in figure 11.1. In order to track halos through all the snapshots of the simulation, Consistent Trees starts at the last snapshot and works backward. This approach is inspired by the general assumption in the Λ CDM-model, that halos are build up by gradual accretion and mergers. Therefore, a halo found at one time step must have a progenitor at a previous time step, unless it is small enough that it has only just crossed the detection threshold of the halo finder. However, since halos can merge with each other or be disrupted by tidal forces, the presence of a halo at some time step does not imply that it must also exist at the next time step. Therefore, the most reliable predictions about halos can be made backwards in time. Based on backwards predictions of the halo properties, such as position and velocity, the most likely progenitor of a



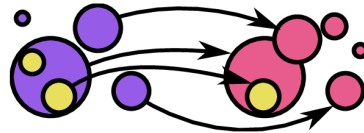
For each halo at t_{n-1} , identify the halo at t_n that contains the largest fraction of the original halos' particles. Calculate the characteristic errors in the predicted positions, velocities, and maximum circular velocities.



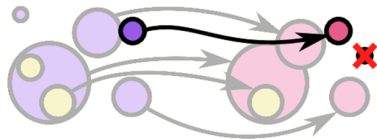
Based on positions and velocities at t_n , predict the properties of the halos at t_{n-1} .



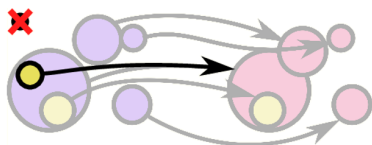
Cut unlikely connections ...



... and create new connections between halos for which the predictions have provided a good match.



Create phantom halos at t_{n-1} for each of the halos at t_n that lack a progenitor. Remove phantom halos for which no real progenitor has been found for several timesteps.



Assume that halos with no descendant have either merged into the halo exerting the strongest tidal forces, or that they were not real halos but only statistical fluctuations.

Figure 11.1: The Consistent Trees algorithm, illustration from [95]. © The Astrophysical Journal. Reproduced with permission from the journal and the authors. The explanations for what happens in each step of the algorithm are my own.

given halo is identified, by requiring a consistent evolution of the structures in the simulation. If a halo disappears for a few time steps, the predictions can be used to "fill the hole" in the merger tree. Or, if no plausible progenitor is found, the halo can either be removed from the catalog or acknowledged as a newly formed halo if it is small enough.

For the purpose of linking halos across time steps, a measure similar to the phase space distance used by ROCKSTAR (described in chapter 5) is defined, which provides a metric for ranking the candidate progenitors of a given halo, and defining a maximum distance for physical consistency. The metric is based on three predicted properties for the potential progenitor: position, velocity, and the maximum circular velocity, $v_{\max} = \sqrt{GM(r)/r}$, which is calculated from the maximum of the centripetal force exerted by the halo, and contains information about its radius and mass [30]. In order to calibrate the metric, Consistent Trees starts by making naive guesses for the descendants of the halos at each but the last snapshot. For each halo, the guess is made by considering which halo at the next snapshot receives the largest fraction of the original halos' particles. The characteristic error in the predicted positions, τ_x , velocities, τ_v , and maximum circular velocities, $\tau_{v_{\max}}$, can then be calculated, which provide the calibration for the metric used to distinguish between potential halo links. The difference between the expected ("e") values of the properties for the progenitor of a given halo, and the corresponding values for a candidate ("c") progenitor is measured in units of the characteristic uncertainties for all halos of similar mass at the given time in the catalog. The *property-distance* is defined as

$$d(e, c) = \sqrt{\frac{|\mathbf{x}_e - \mathbf{x}_c|^2}{2\tau_x^2} + \frac{|\mathbf{v}_e - \mathbf{v}_c|^2}{2\tau_v^2} + \frac{[\log(v_{\max,e}) - \log(v_{\max,c})]^2}{2\tau_{v_{\max}}^2}}, \quad (11.1)$$

By computing the distance between halos and their potential progenitors, the most likely formation history for each halo is identified. And halos for which no consistent history can be identified are removed from the catalogs. In this way, reliable and consistent merger trees are obtained, which can then be used to predict the formation and evolution of galaxies.

11.3 Stage 2: Galaxy formation

As previously mentioned, dark matter halos act as the formation sites for galaxies, with the details of the processes involved being dictated by the merger histories for the halos. In this section, we will give a rudimentary description of how galaxy formation is modeled in the Galacticus code, with much of the physics described following [93]. The Galacticus code is written and developed by Andrew Benson, who gives an overview of the code in [96]. In addition to this, he has also written a very extensive manual, [97].

11.3.1 The basic scheme of Galacticus

In the previous section, it was described how the merger history of dark matter halos could be extracted from an N-body simulation. This merger tree provides the starting point for Galacticus,

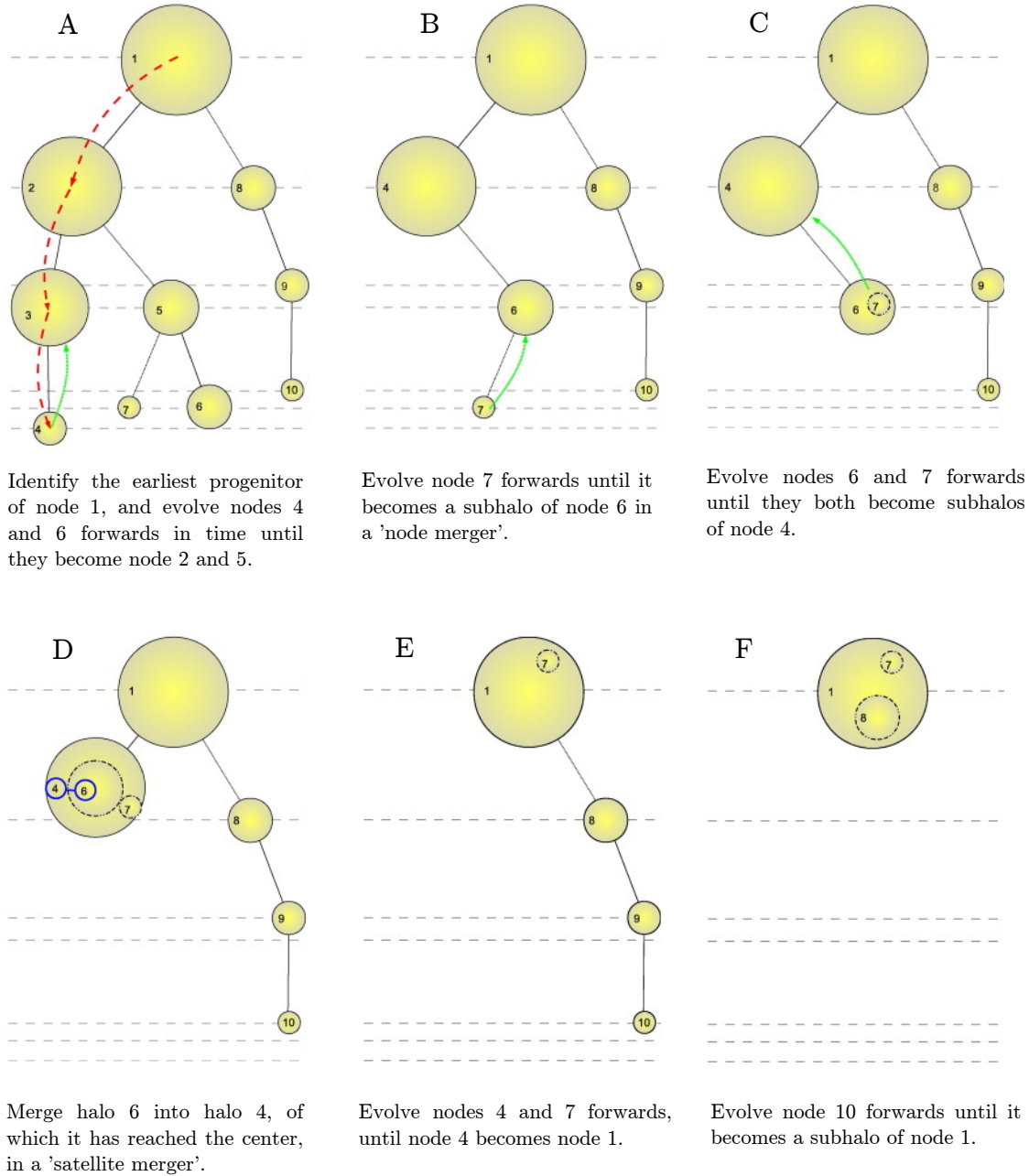


Figure 11.2: Illustration of the node promotion in Galacticus, reprinted from [96]. © Elsevier, reproduced with permission from Elsevier and the author; the explanations for what happens at each step are my own. Dashed lines represent different times, with time running upwards, and the circles representing nodes in the tree, with bigger radii corresponding to larger masses.

which treats the merger tree as a linked hierarchy of nodes, as illustrated in part A of figure 11.2. In addition to the dark matter halo, each node can contain a number of different components associated with the evolution of the baryonic material in the halo. For our purposes, the most important of these are the hot gas halo and the cold gas and stars contained in the galaxies. The galaxies are split into two components, a disk and a spheroid, each with their own reservoir of gas and population of stars.

Figure 11.2 illustrates the order in which Galacticus treats the evolution of the baryonic processes within the nodes. A detailed explanation of what happens at each stage is given in the figure. Galacticus begins with the "root node" of the tree, labeled "1" in the figure, which is present at the latest time included in the illustration. In order to determine the future evolution of this node, Galacticus first checks if there is any history of the node that should be taken into account. Since the node has evolved from another halo, the one labeled "2", this must be treated first. But this node has also descended from nodes at previous times, which therefore must be treated before node "2", and so on. The figure illustrates how Galacticus moves back through the node hierarchy and identifies the original progenitors of each node. It also identifies when the halo contained in one of the nodes becomes a subhalo of a larger halo. When the primary progenitor of a given node has been found, the physical processes – such as the initial formation and subsequent cooling of a hot gas halo, and the formation and evolution of a galaxy – can be evolved forwards in time according to a set of differential equations. In addition to following the individual evolution of nodes, Galacticus creates "pipes" which allow flow of heat or material between separate nodes. When two nodes merge, what happens depends on the past evolution of the nodes involved in the merger. After two nodes have merged, the resulting new node can be evolved forwards in time until the next merger or the final time of the simulation is reached. In the next sections, we give a few examples of how the baryonic processes taking place within the nodes are modeled, and specify what happens when nodes merge with each other.

11.3.2 Evolution of hot and cold gas

As described in chapter 3, gas starts to fall into the potential wells of the dark matter halos after recombination. In this process, it is assumed to be heated by shocks, which occur when the velocity of the accreting gas exceeds the speed of sound [98]. This creates a pressure which supports it against further collapse, forming a "hot gas halo", as illustrated in figure 11.3. The temperature of this gas depends on the mass, M , of the halo, and on its size, which can be characterized by the virial radius, r_{vir} , defined in chapter 5. The mass and size can be used to define a (equivalent) circular velocity of the halo at the virial radius, $V_H = \sqrt{GM/r_{\text{vir}}}$. In Galacticus, the hot gas halo is assumed to be isothermal, with a temperature determined by the equation of hydrostatic equilibrium, giving the virial temperature of the halo as

$$T_{\text{vir}} = \frac{1}{2} \frac{\mu m_H}{k} V_H^2, \quad (11.2)$$

where $\mu = 1/1.71$ is the mean molecular weight of the primordial gas, m_H is the mass of a hydrogen atom and k is Boltzmann's constant. The circular velocities typically lie in the interval

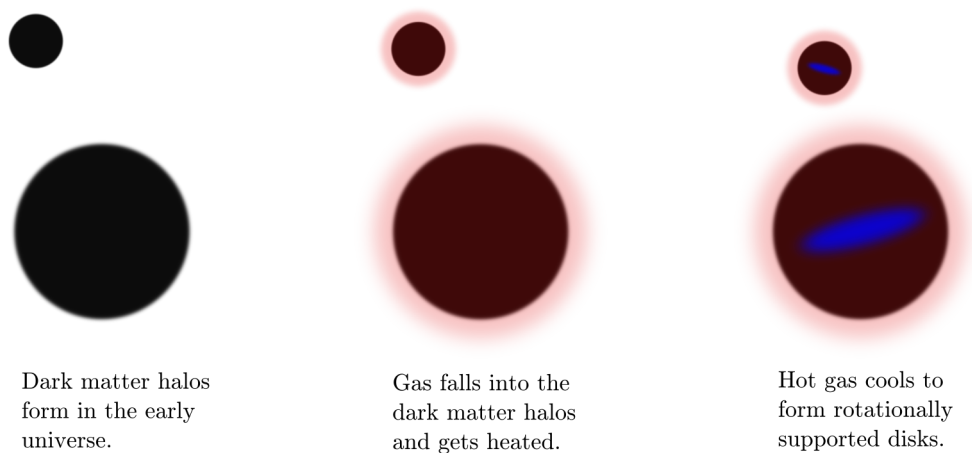


Figure 11.3: Illustration of the formation of hot gas halos in two dark matter halos, and the subsequent cooling of gas to form a disk.

$10 - 10^3$ km/s, which results in temperatures between $10^3 - 10^7$ K. The temperature determines the density and ionization state of the gas, conditions which, together with the metallicity and the state of the background universe, determines how fast the gas can cool. In the very early universe, inverse Compton scattering of CMB photons by electrons in the hot gas halo was an important cooling channel, whereas for relatively cold gas, rotational and vibrational excitations of molecular hydrogen through collisions, followed by decay, plays an important role. Under more normal circumstances, the most important cooling mechanisms relevant for galaxy formation are emission of photons from excited atoms after a collision with an atom or an electron, and bremsstrahlung radiation from electrons accelerated in an ionized plasma in massive clusters. How effective the cooling due to collisions is depends on the energy levels of the atoms of the gas, and therefore on its chemical composition. As a result of this, a higher metallicity results in more effective cooling [93].

As the gas cools, the pressure drops, and the cold gas falls to the center of the dark matter halo. Here it forms a disk, if it has sufficient angular momentum, as illustrated in the leftmost picture in figure 11.3. The amount of gas that has cooled can be described by a cooling radius, which propagates outwards until either all the gas has cooled, or the process is disrupted by a merger with another galaxy [93].

If the angular momentum of the contracting gas is insufficient to support the galactic disk, a *bar instability* forms, which transfers material from the disk to a spheroid component of the galaxy [97, chapter 13.10]. As cold gas settles in the disk or spheroid in the center of the halos, it begins to form stars, as will be discussed in the next section.

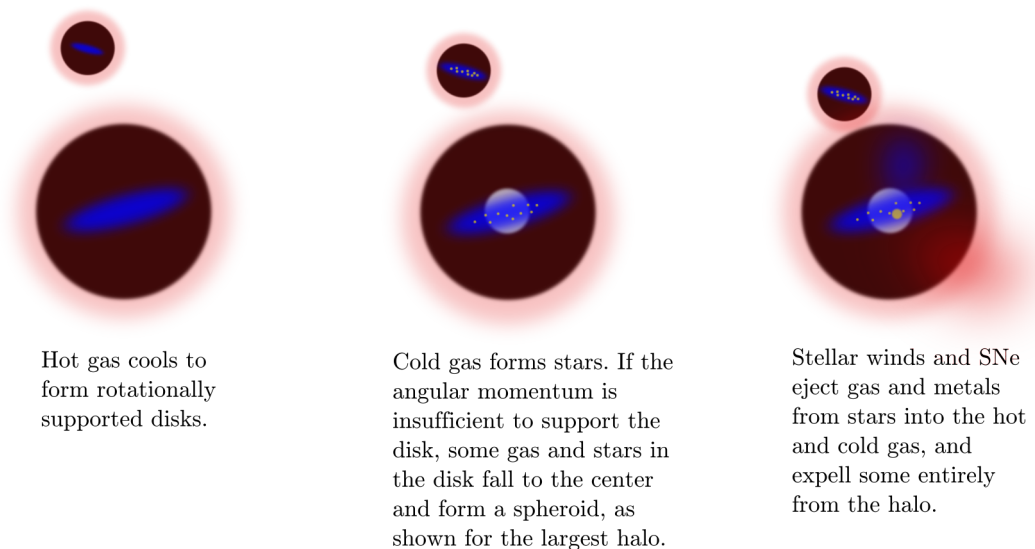


Figure 11.4: (Continued from figure 11.3) Illustration of the formation of stars in galaxies at the centers of halos, and feedback from stellar winds and supernovae.

11.3.3 Star formation and feedback

As a continuation of figure 11.3 from the previous section, figure 11.4 illustrates the formation of stars in the disk and spheroid of the galaxies. Denoting the timescale for star formation¹ by τ_* , the stellar mass formed per time interval is obtained from the mass of cold gas, M_{gas} , as $\Psi = \frac{M_{\text{gas}}}{\tau_*}$.

Galacticus follows the evolution of mass and stars in each component of the nodes. Consider, as an example, the total rate with which the stellar mass contained in the disk of a given node changes with time. In addition to the rate with which cold mass is turned into stars in the disk, Ψ_{disk} , one also needs to take into account the rate with which stellar winds and supernovae expel mass from the stellar population, \dot{R} , and the rate with which stars in the disk are transferred to the spheroid via a potential bar instability. Taking each of these processes into account, the total stellar mass of the disk evolves according to

$$\dot{M}_{\text{disk,stars}} = \Psi_{\text{disk}} - \dot{R} - \frac{M_{\text{disk,stars}}}{\tau_{\text{bar}}}, \quad (11.3)$$

where τ_{bar} is the timescale for the bar instability, which specifies how fast gas and stars are transferred from the disk to the spheroid due to insufficient angular momentum.

From similar considerations, equations for the differential evolution of the mass in stars in the spheroid as well as the mass in gas in both components can be deduced. Likewise, the abundances of metals in the gas and stars of each component can be followed, using the *yield* of the different

¹The timescale for star formation is calculated according to different prescriptions in the disk and spheroid, as described in [97, chapter 13.44].

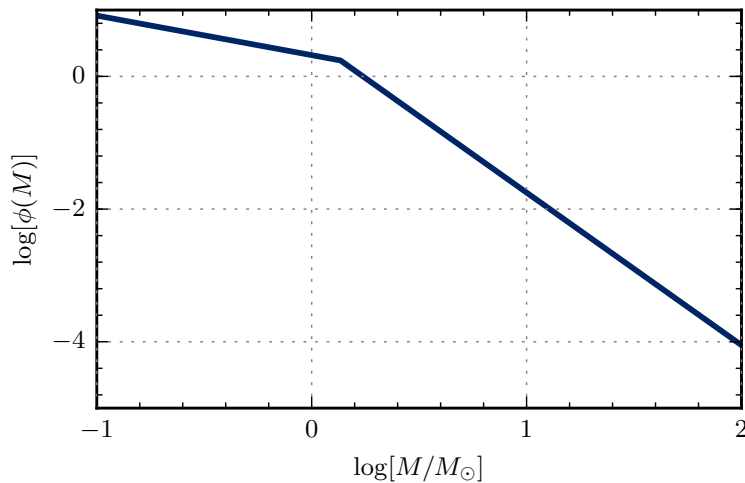


Figure 11.5: The Chabrier initial mass function.

metals, which specifies how much of each element is created as a function of time for a given stellar population [96]. By also adding equations for how the hot gas halo evolves due to accretion and subsequent cooling of gas, and further equation for any other potential component contained in the node, a set of coupled differential equations is obtained, which dictate how the node evolves with time.

The rate with which mass and metals are recycled from a stellar population evolves over time – for example, stellar winds are much stronger in stars evolving off the main sequence, and the release of mass and metals from supernovae only occur as the stars end their lives. However, following the detailed evolution of each stellar population is extremely computationally time consuming, and the time scales involved are much smaller than those with which we are concerned. Therefore, we use the "instantaneous recycling approximation" in Galacticus [97, chapter 13.45], in which the metals and mass recycled from stars are released instantaneously.

Initial mass function of stars

To predict, for example, how large a fraction of the mass in a stellar population is recycled, one needs to know how many stars of different masses are formed, because massive stars have stronger stellar winds, and only stars above a certain mass end their lives in a supernova [93]. The fraction of stars formed as a function of their mass is determined by the initial mass function (IMF) of a stellar population. As is the default in Galacticus, we use the same IMF, the *Chabrier* [99], independent of the physical conditions. The Chabrier IMF has a log-normal distribution for small stars, with a mass, M , smaller than $M_t = M_{\odot}$, and a power law for stars more massive than this. No stars smaller than $M_l = 0.1M_{\odot}$ or larger than $M_u = 125M_{\odot}$ are formed. The IMF is shown

in figure 11.5, and has the form:

$$\phi \propto \begin{cases} \frac{1}{M} \exp\left(-\frac{[\log(M/M_c)/\sigma_c]^2}{2}\right) & M_l < M < M_t \\ M^\alpha & M_t < M < M_u \\ 0 & \text{otherwise,} \end{cases} \quad (11.4)$$

where the parameters of the log-normal distribution are $M_c = 0.08$ and $\sigma_c = 0.69$, and the slope of the power law is $\alpha = -2.3$ [97, chapter 13.26].

In addition to the recycled fraction, the distribution of stars of different masses is also necessary for predicting the luminosity from a mass of formed stars. As this is one of the primary observables of galaxies, we will briefly explain how they are obtained below.

Star formation histories and luminosities of galaxies

The luminosity of a given galaxy can be calculated based on its history of star formation, by combining it with a so-called "stellar population synthesis model". Based on the amount of stars formed of a given mass and metallicity, the stellar population synthesis model predict the spectrum of light as a function of time since the stars were formed. Hereby, the entire luminosity of the galaxy can be calculated [93]. The population synthesis model used to calculate the spectra in Galacticus (described in [97, chapter 13.46]) comes from [100].

If requested to do so, Galacticus also saves the star formation histories for each galaxy, with time steps of 0.1 Gyr [97, Chapter 7.5]. As we will see in the next chapter, this will be useful for predicting the type Ia supernova rates.

11.3.4 Mergers

The last mode of node evolution that we will consider involves some of the most violent events in the histories of galaxies, which therefore play an essential part in predicting their evolution. The halo merger tree, which in Galacticus is translated into a hierarchy of nodes, describes how the individual halos are build up by merging with other halos. Such merging events have significant implications for the galaxies residing at the center of the halos.

A merging event consists of two parts: In the first part, which is called a "node merger", a halo enters another, larger halo, as illustrated figure 11.6. At this point, the particles that make up the small halo are still gravitationally bound to each other, and the galaxy at the center of the halo is unaffected; the small halo has simply become a subhalo, or a satellite, of the larger halo. When the node has become a satellite, it spirals inwards toward to the center of its host due to dynamical friction, i.e. the process in which the satellite is slowed down by gravitationally dragging along the surrounding material in the halo [93]. When the satellite eventually reaches the center, a "satellite merger" occur. In a satellite merger, the galaxy at the center of the satellite merge with the central galaxy of its host. The destiny of the merging galaxies depends on the ratio between their baryonic masses. If the satellite galaxy has a mass of more than 25% of the central galaxy in

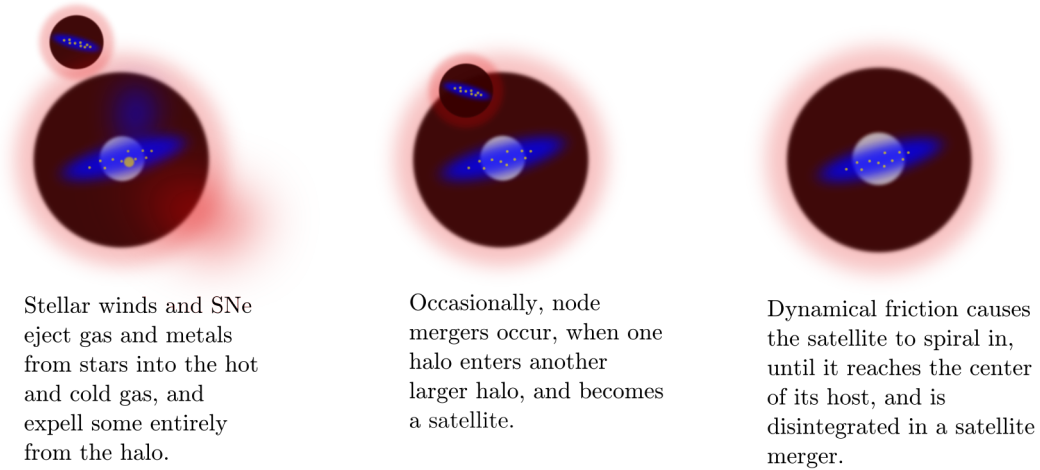


Figure 11.6: (Continued from figure 11.4) Illustration of a halo merger and a satellite merger.

the host halo, the merger is considered to be a major merger, which means that all the baryonic mass from both galaxies moves to the spheroid component of the central galaxy. Otherwise, the merger is a minor merger, and in this case, only the baryonic material of the satellite moves to the spheroid of the central galaxy [96]. In the case illustrated in figure 11.6, the event turned out to be a minor merger, which can be seen from the last panel as the disk of the central galaxy is intact.

11.4 Summary

In this chapter, we have traced the formation of galaxies through the merger tree of dark matter halos, and simple models for the baryonic processes of gas that fell into the halos after recombination. Simulating these models enables the creation of galaxy catalogs and star formation histories for the galaxies. In the next chapter, we will show how this can be used to predict their present day rate of type Ia supernovae.

Chapter 12

Type Ia supernovae

The rate of occurrence of type Ia supernovae (SNe Ia) are of great interest, as they allow probing the universe on much larger scale than any other standard candle. They are also important for the theory of galaxy formation, as they are needed to accurately predict the metallicity of different environments, and to model the feedback from a stellar population.

Type Ia supernovae are believed to have an entirely different origin than other types of supernovae. Most supernovae result from massive stars, which fail to expel a sufficiently large fraction of their mass towards the end of their lives for them to end up as a white dwarf. As a result, the core of the star undergoes a gravitational collapse as its nuclear fuel is depleted, releasing great amounts of energy, gas, and metals. Historically, supernovae have been characterized by the absorption lines of different elements in their spectra. According to this classification, type II supernovae are those showing the presence of hydrogen in their spectra, while type I supernovae do not. However, as it turned out, the supernovae resulting from the gravitational collapse of a star ending its life can either show hydrogen lines in its spectrum or not, depending on the exact circumstances. Such supernovae are nowadays referred to as core-collapse supernovae [101]. A certain subset of the type I supernovae, namely type Ia, is believed to have an entirely different origin, as we will discuss in this chapter.

In the context of galaxy formation, core collapse supernovae and type Ia supernovae play different roles, partly because they produce different metals, but also because they occur on different timescales. Core collapse supernovae are usually assumed to occur instantaneously following the formation of a population of stars, whereas type Ia supernovae have been found to occur in galaxies in which star formation ceased a long time ago.

In this chapter we present the problem concerning the unknown progenitors of the type Ia supernovae, and explain how the supernovae are implemented in the semi-analytical galaxy formation code *Galacticus*. We then introduce the delay time formalism for describing the rate of these supernovae as a function of the star formation history of galaxies, and explain how we use this to generate SN Ia rate catalogs for our analyzes.

12.1 The progenitor problem

Even though type Ia supernovae are of great interest and importance for cosmology, their origin is still very uncertain. The two main competing models for the progenitors of type Ia supernovae are the single degenerate (SD) model [102], where a white dwarf accretes mass from a companion star near the end of its life, and the double degenerate (DD) model [103, 104], where two white dwarfs merge after losing energy and angular momentum to gravitational waves. Since a progenitor to a type Ia supernova has never been observed pre-explosion, there is no strong observational evidence for either of these. Below, we give a short description of each of the two potential scenarios, following the review [105].

12.1.1 Single Degenerate ("SD") model

This scenario was first suggested in [102], inspired by the problem that supernovae occur in elliptical galaxies, even though only stars which are not massive enough to go supernova are still consuming nuclear fuel. They propose that a type I supernova could occur in a system consisting of a massive star that has become a carbon-oxygen white dwarf, and a relatively light companion star which has just reached the asymptotic giant branch, and is now transferring mass to the white dwarf. At some point, the white dwarf becomes too massive to be supported by the degeneracy pressure of its electrons. This point is known as the Chandrasekhar limit, and when it is exceeded, the white dwarf is assumed to explode in a supernova.

This scenario, as recognized in [102], is quite sensitive to the rate of accretion. If the accretion is too slow, the accreted hydrogen will ignite and explode on the surface, blowing away material. On the other hand, if the accretion rate is too high, the outer layers of the white dwarf will expand. Therefore, self-regulating mechanisms – such as winds created by the matter accreting on the white dwarf blowing away material from the common envelope [106] – is necessary for this scenario to be able to explain a significant number of supernovae.

In addition to these problems, it is hard to match the observed number of type Ia supernovae with the predicted rate based on this scenario, which comes from population synthesis models. A possible solution could be if a binary system could explode in a supernova even if its total mass was less than the Chandrasekhar mass, in a so-called "sub-Chandra" explosion [105].

12.1.2 Double Degenerate ("DD") model

In the double degenerate model, which was proposed in [103, 104], it is assumed that the progenitor systems of type Ia supernovae consist of two white dwarfs. Depending on their chemical compositions and masses, the merging plays out in different ways, but the least massive of the white dwarfs is typically predicted to be disrupted into a disk around its companion. At some point, enough material has been accreted from the disk that the primary white dwarf is pushed over the Chandrasekhar limit, causing the supernova explosion.

As the SD model, the DD model also has a hard time reproducing the rate of type Ia supernovae actually observed, as the number of binary white dwarf systems with a total mass greater than the Chandrasekhar mass predicted by stellar models is too low. However, it turns out that the *total* merger rate of white dwarfs is consistent with the observed type Ia supernova rate. Simulations have shown that it is possible to ignite a supernova in a merger between two white dwarfs whose total mass is sub-Chandra, for example through compression of helium accreted on the surface of the primary white dwarf [107], or a merger remnant consisting of a carbon core which is compressed to the point of ignition by a very dense accretion disk [108].

12.2 Type Ia supernovae in Galacticus

The implementation of type Ia supernovae in Galacticus builds on the method described in [109]. In this paper, the progenitors for type Ia supernovae are assumed to be the single degenerate (SD) systems described above in section 12.1.1. Using this model allows a calculation of the type Ia supernova rate on the basis of the star formation history and initial mass function (IMF) of the galaxies. However, as we saw, this model cannot produce the actual number of type Ia supernovae observed in the universe.

Therefore, rather than using the rates implemented in Galacticus, we use the stellar formation history of the galaxies to predict the rate of type Ia supernovae, to avoid assuming a specific model for their progenitors. According to [105], many different types of observations agree on the shape and the approximate rate of type Ia supernovae as a function of the time that has passed since a mass of stars were formed, as we will describe in the next section.

This might not be the most consistent way of getting the SN Ia rates in the galaxies – after all, these events are already implemented in Galacticus, and used for predicting metallicities and expel and heat gas. But we believe that we will get a more truthful distribution of supernovae by using the observed dependence on the star formation history than by using the theoretical prediction based on an uncertain assumption about the progenitor systems.

12.3 Star formation and the type Ia supernova rate

In 2005, Scannapieco and Bildsten suggested that the rate of type Ia supernovae could be described as a sum of two separate components, possibly stemming from two different types of progenitors [110]. One of the components was proposed to be proportional to the stellar mass of the galaxies, and the other component to be proportional to the current star formation rate. This two-component model was able to explain the occurrence of type Ia supernovae in galaxies that had long since ceased forming stars. Furthermore, it did a fairly good job at predicting the oxygen to iron abundance in the gas in galaxy clusters, which depends on the number of type Ia supernovae – the primary source of iron – relative to the number of core collapse supernovae, which primarily produce α -elements such as oxygen.

According to [105], the two-component model can alternatively be interpreted as a coarse time binning of a smooth function, which describes the distribution of time delays occurring between the time a mass of stars was formed and when these stars explode in a type Ia supernova. This is the model that we choose to use for our study.

Exactly how this distribution of delay times look depends on the progenitor systems for the type Ia supernovae. Therefore, observations of the SN Ia rate coupled with observations of the star formation history of a galaxy is a possible way of learning about the progenitors of type Ia supernovae. Our primary interest is in the empirical observations of where and when type Ia supernovae occur, which will allow us to accurately model their occurrences based on the semi-analytical modeling described in the previous chapter. But in order to get an understanding of the origin of the delay time distribution (DTD), we will briefly discuss the predictions for the DTD due to the SD and DD models.

12.3.1 Predictions about the DTD

A detailed derivation of the DTD predicted by each of the two scenarios is given in [111]. Here, a few simple arguments will instead be given for the expected form in each case, following [105]. One of the features that will be ignored here and throughout, is the initial delay before any supernovae occur, since at least one of the stars in the binary system must have evolved through its main sequence and become a white dwarf. This is not relevant for our purposes, since the lifetime of the most massive stars that end their lives as white dwarfs is only about 40 Myr.

In the SD model, the DTD is expected to drop off after a few Gyr, when the donor stars evolving off the main sequence is no longer massive enough to feed the (likewise less and less massive) white dwarfs enough to push them over the Chandrasekhar mass. This drop has not been observed.

In DD models, the primary timescale is set by the time it takes for the two white dwarfs to reduce their separation, a , so that they can merge. This is done by getting rid of rotational energy by gravitational wave emission, and the time required for this scales as $t \propto a^4$ (ignoring the dependence on the white dwarf masses). The initial distribution of separation distances in binaries is well described by $dN/da \propto a^{-1}$, and so, the merger rate can be estimated as

$$\frac{dN}{dt} = \frac{dN}{da} \frac{da}{dt} \propto t^{-1}. \quad (12.1)$$

As we will see, this turns out to be in good agreement with observations of the DTD.

12.3.2 From star formation histories to supernova rates

The delay time distribution¹, $\Psi_{\text{DTD}}(\tau)$, predicts the number of type Ia supernovae that will result from a unit mass of stars, which was formed a time τ ago. Therefore, the rate of type Ia supernovae

¹ In [105], Ψ is used for the delay time distribution. However, as we have seen in the previous chapter, in the Galacticus documentation, [96, 97], Ψ is used for the star formation rate. In the thesis, we have chosen to keep the notation from Galacticus for the star formation rate, and hence uses Ψ_{DTD} for the delay time distribution.

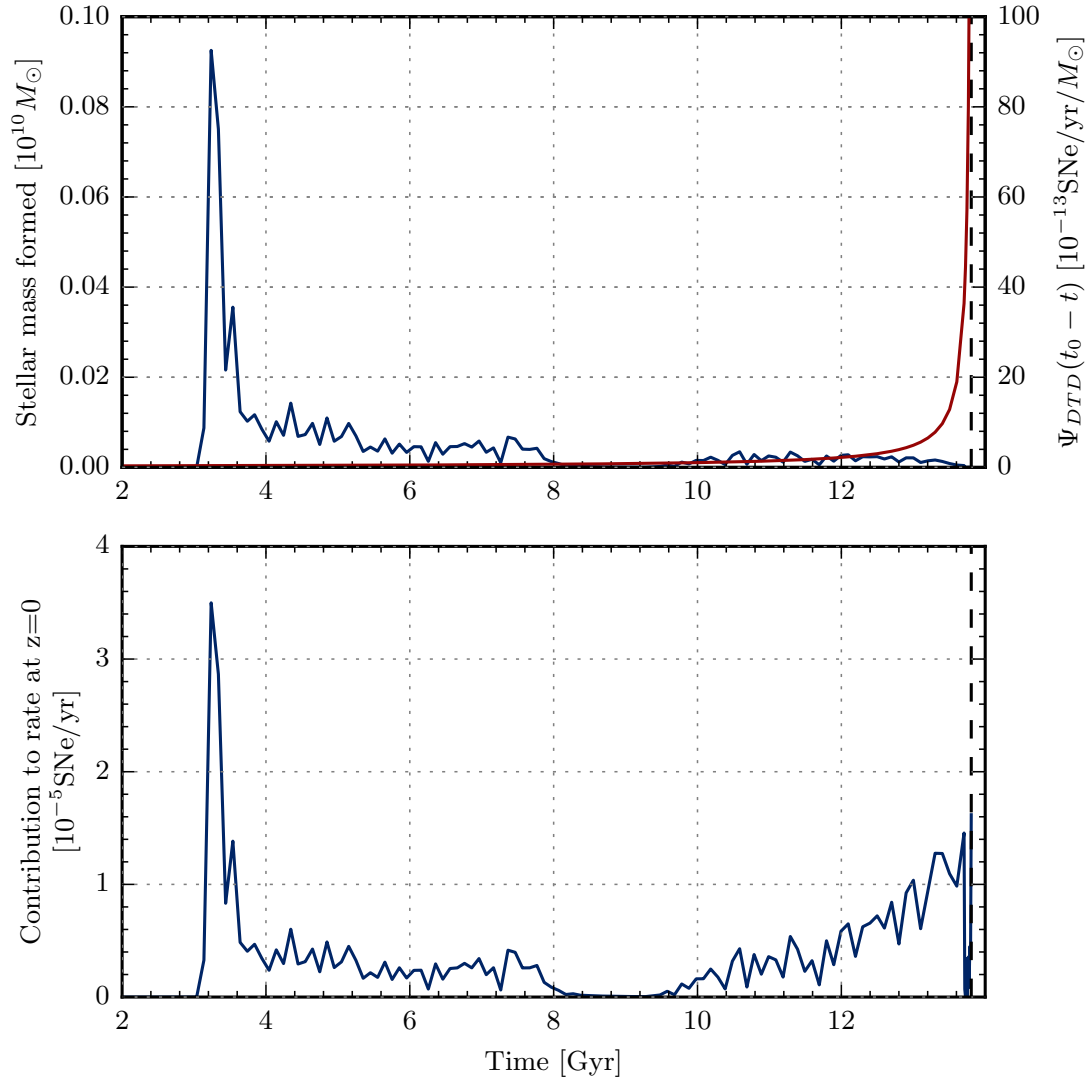


Figure 12.1: **Top:** Example of a star formation history; the stellar mass formed at each time is shown on the left axis (full blue line) as a function of time t . This is plotted together with the delay time distribution (red line and right axis). The black, dashed line marks $t = t_0$, the present age of the universe. **Bottom:** Contribution to the present day type Ia supernova rate from the stars formed at each time, obtained by multiplying the star formation history and delay time distribution shown above. By integrating this function, the total present day supernova rate for the galaxy is found, as described in equation 12.2.

in a given galaxy at time t , $r_{\text{Ia}}(t)$, can be obtained by convolving the star formation history (SFH), Ψ , by the DTD, i.e.,

$$r_{\text{Ia}}(t) = \int_0^t \Psi(t - \tau) \Psi_{\text{DTD}}(\tau) d\tau. \quad (12.2)$$

This is illustrated in figure 12.1. In the top panel, an example star formation history is shown, along with the delay time distribution. In the bottom panel of the figure, it is shown how many supernovae per year is predicted to result at $z = 0$ from that specific star formation history, equivalent to the integrand of equation 12.2. The total rate of type Ia supernovae $z = 0$ is obtained by integrating this function.

12.3.3 The observed DTD

In order to measure the delay time distribution from observations, one possibility is to take advantage of the fact that massive clusters have a very simple star formation history, with most of their stars having been formed within a short time ~ 100 Myr around $z \sim 3$. Writing the star formation history for a specific cluster as a delta-function around the time of star formation, $\Psi(t) = M_{\text{formed}}(t_f) \delta(t - t_f)$, where $M_{\text{formed}}(t_f)$ denotes the entire stellar mass formed at t_f , the present day rate of type Ia supernovae in the cluster is found from equation 12.2 as

$$r_{\text{Ia}}(t) = \int_0^t M_{\text{formed}}(t_f) \delta(t - \tau - t_f) \Psi_{\text{DTD}}(\tau) d\tau \quad (12.3)$$

$$= M_{\text{formed}}(t_f) \Psi_{\text{DTD}}(t - t_f). \quad (12.4)$$

By using the surviving mass fraction after a time t , $m(t)$, this can be expressed via the observed stellar mass, since $M_{\text{formed}}(t_f) \cdot m(t - t_f) = M_{\text{observed}}(t)$. Using this, we get an expression for the delay time distribution in terms of observable quantities²

$$\Psi_{\text{DTD}}(t - t_f) = \frac{r_{\text{Ia}}(t) \cdot m(t - t_f)}{M_{\text{observed}}(t)}. \quad (12.5)$$

Observing massive clusters at different redshifts, which is equivalent to observing them at different delay times after their peak of star formation around $z = 3$, thus provides a way to directly measure the DTD [105].

Another way to measure the DTD, is by comparing the total observed type Ia supernova rate in the local universe to the best predictions for the total star formation history in the same region. This was first tried in [112] and later in [113], finding a good fit with a DTD of the form predicted by the DD model. There are several other methods as well, such as comparing the SN Ia rates in different types of galaxies with different characteristic ages, or actually reconstructing the SFH

²Actually, neither the stellar mass nor the surviving mass fraction are directly observable, but both can be obtained from stellar population synthesis models.

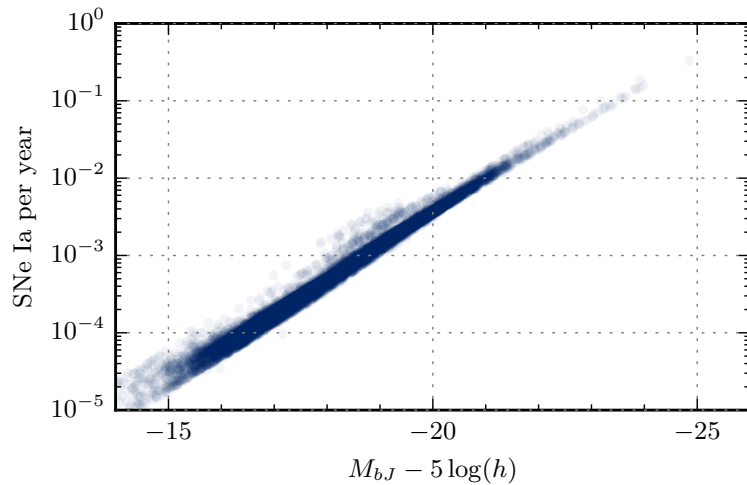


Figure 12.2: We find that the logarithm of the type Ia supernova rates, as modeled after the star formation histories using the delay time distribution, is proportional to the absolute magnitude of the galaxies. This is the same trend as deduced from the analysis of host galaxies of type Ia supernovae in the SDSS survey, as shown in figure 12 of [114].

of individual galaxies and finding the DTD that best predicts their current SN Ia rates. These different methods predict DTDs that all agree with each other in both form and normalization. At delay times above 1 Gyr, a good fit is obtained with [105]

$$\Psi_{\text{DTD}}(t) = 4 \times 10^{-13} \text{ SNe yr}^{-1} M_{\odot}^{-1} \left(\frac{t}{1 \text{ Gyr}} \right)^{-1}. \quad (12.6)$$

At delay times below 1 Gyr, the results are still quite uncertain.

By using this result, we are now able to predict type Ia supernova rates in the galaxy catalogs produced by Galacticus.

12.4 Construction of SNe Ia catalogs

As mentioned in the previous chapter, Galacticus allows us to save the history of star formation in each of the galaxies it follows. An example of such a star formation history was shown in figure 12.1. Using these star formation histories, we calculate the present day rate of type Ia supernovae for each galaxy in the $z = 0$ catalog produced by Galacticus. In figure 12.2, the resulting rates are shown as a function of the absolute magnitude of the galaxies in the b_J -band, showing that the logarithm of the present day rate of type Ia in the galaxies grows proportionally to the absolute magnitude of the galaxies. This is in agreement with the result presented in [114], where the characteristics of host galaxies of type Ia supernovae in the SDSS survey are examined, and it is found that the type Ia supernovae do not tend to occur in galaxies of a specific type or color, but with a frequency mainly determined by the luminosities of the galaxies.

The total, volumetric supernova rate obtained for the main simulation that will be used for our analysis, as will be described in the next chapter, turns out to be $1.1 \times 10^{-4} \text{ SNe yr}^{-1} \text{ h}^3 \text{ Mpc}^{-3}$. This is roughly a factor of 4 higher than the rate obtained in [115], but in very good agreement with the (somewhat more uncertain) rates obtained in [61, 116]. In the next chapter, we will use type Ia rate catalogs obtained using the methods described in this chapter to investigate whether their distribution allows for precise determination of the local velocity field. If this is the case, this could become a useful probe of cosmological parameters in the near future, with the large number of type Ia supernovae that will be observed in the upcoming LSST sky survey.

Chapter 13

Measuring the velocity field from type Ia supernovae in an LSST-like sky survey

In this chapter, we present analyzes of the velocity field based on the type Ia supernova rate catalogs generated as described in the previous chapters. The chapter is an adapted version of the paper [4]¹.

[4] Io Odderskov and Steen Hannestad, *Measuring the velocity field from type Ia supernovae in an LSST-like sky survey*, e-print arXiv:1608.04446.

Submitted to JCAP.

13.1 Introduction

In the near future, the Large Synoptic Survey Telescope (LSST) will carry out observations of millions of type Ia supernovae [117]. As the best standard candles at cosmological distances, the lightcurves of these supernovae will provide precise luminosity distances to millions of galaxies throughout the universe. For some sub-sample of these, the spectroscopic redshift will be measured for the host galaxy. Together, the supernova luminosity distances and spectroscopic redshifts of their host galaxies will lead to an unprecedented opportunity for describing the velocity structure of the universe. Such observations can for example be used to measure the expansion history, and provide precise measurements of the Hubble constant, greatly improving the already extremely successful measurements that have been done in the past [12–14, 35].

We investigate the potential for a sky survey with the geometry of the LSST main survey for measuring the angular power spectrum of the radial peculiar velocity field from type Ia supernovae. The basic idea is the same as presented in [89], but we use a more realistic distribution of supernovae for our mock surveys, as well as the actual geometry of the LSST sky survey. This allows us to

¹The results for the supernova rates, and consequently for the measured velocity fields, deviate slightly from those found in [4]. This is due to a small mistake in the calculation of the supernova rates used in the paper, which has been corrected for the results presented here. However, the changes are insignificant, and do not alter any of the conclusions.

study the problems that arise due to incomplete sky coverage and the non-uniform distribution of supernovae in the sky. We use methods developed for analysis of the CMB to correct for the mixing of different multipoles with each other, which is caused by large, unobserved areas in the survey geometry. And we smooth the velocity field to remove features on scales comparable to the size of the largest holes in the distribution of supernovae within the survey. In order to get a realistic prediction for where type Ia supernovae occur, we run a large N-body simulation and populate it with type Ia supernovae based on the star formation history in the individual halos which we obtain with the code Galacticus code, as described in chapter 11.

The chapter is structured as follows: The simulations and mock supernova catalogs are described in section 13.2, and the selection of observers and mock observations are described in section 13.3. In section 13.4, we describe how the angular power spectrum is measured, and how it is affected by the smoothing process and by the correction for the coupling of multipoles caused by the missing sky coverage. We present our results in section 13.5 and conclude in section 13.6.

13.2 Mock supernova catalogs

In this section, we describe the simulations used for the study. We show the results for the galaxy populations and supernova rates in a set of small test simulation, which have been used to test the galaxy catalogs against observations, and to choose the resolution for the large simulation on which we base our analysis of the velocity field.

13.2.1 Simulations

The large scale structure of the universe is best captured by N-body simulations, which therefore form the basis for our analysis. The simulations are based on cosmological parameters in agreement with those determined from the CMB by the Planck collaboration [32]. We use a modified version of the GADGET-2 code [26, 77], with initial conditions generated using a code written by J. Brandbyge [29] based on transfer functions computed using CAMB² [34]. Specifically, the transfer functions are calculated with $(\Omega_b, \Omega_{CDM}) = (0.048, 0.26)$, whereas only cold dark matter is used in the N-body simulations. A flat universe is assumed, and $(h, \sigma_8) = (0.68, 0.84)$. The simulations are run from a redshift of $z = 50$ until $z = 0$.

The main simulation is run in a periodic box of side length 512 Mpc/h. In order to determine the necessary resolution to resolve the galaxies in which type Ia supernovae occur, we also run a set of smaller simulations in boxes of side length 64 Mpc/h with varying mass resolutions, as summarized in table 13.1. As will be discussed in section 13.2.2, we find that a sufficient resolution for our main simulation is obtained with 1600^3 particles in the box. The temporal resolution is found not to make any significant difference for the galaxy catalogs. We choose to write snapshots at 45 different times, linearly separated in scale factor from the beginning of the simulation to the present age of the universe.

²<http://camb.info/>

	N_{part}	Box size [Mpc/h]	$M_{\text{min}} [10^{10} M_{\odot}/h]$	N_{snaps}
Test	128 ³	64	21	45
	174 ³	64	8	45
	200 ³	64	6	30
	200 ³	64	6	45
	200 ³	64	6	60
	224 ³	64	4	45
	312 ³	64	1	45
Main	1600 ³	512	6	45

Table 13.1: Table over the spatial and temporal resolutions of the simulations. According to the ROCKSTAR user manual [31], the halo finder can be trusted down to halos comprised of 20 DM particles. We show which mass this corresponds to in each of the simulations.

13.2.2 Mock galaxy and supernova catalogs

Galaxies are identified in the N-body simulations using the methods described in chapter 11. Halos and halo merger trees are created with the ROCKSTAR [30] and Consistent Trees [95] codes. Based on the merger trees, the Galacticus code [96] uses semi-analytical methods for modeling the processes of galaxy and star formation.

In order to test the galaxy catalogs produced with Galacticus, we compare them with observations of the galaxy luminosity function, Φ_{LF} , and stellar mass function, Φ_{SMF} . The luminosity function, i.e. the number of galaxies per volume per luminosity interval or, equivalently, the number density of galaxies per unit absolute magnitude, is one of the most fundamental observables in the context of galaxy populations. It has been found that the Schechter function gives a good fit to the galaxy luminosity function [118].³

We compare the luminosity function of galaxies in the $z = 0$ -catalogs produced by Galacticus to the luminosity function of galaxies in the 2dF galaxy survey. Specifically, we compare to the fit to the luminosity function in the b_J -band, as determined in [119, table 2],

$$\Phi_{\text{LF}}(M_{b_J}) = 0.4 \ln(10) \Phi_{\text{LF}}^* \left[10^{-0.4(M_{b_J} - M_{b_J}^*)} \right]^{\alpha+1} \exp \left[-10^{-0.4(M_{b_J} - M_{b_J}^*)} \right], \quad (13.2)$$

³ The luminosity function of galaxies looks simplest expressed in luminosities:

$$\Phi_{\text{LF}}(L)dL = \Phi_{\text{LF}}^*/L^*(L/L^*)^\alpha \exp(-L/L^*)dL, \quad (13.1)$$

where L^* is a characteristic galaxy luminosity, which determines where the power-law cuts off, and the exponential takes over, and Φ_{LF}^* gives the normalization of the function. However, it is usually expressed in magnitudes rather than luminosities. As described in chapter 6, the absolute magnitude corresponding to a given luminosity can be found as $M = -2.5 \log(L/L_{\text{ref}})$. If $\Phi_{\text{LF}}(L)dL$ denotes the number density of galaxies in the luminosity range $[L, L + dL]$, we can equate this with the number density of galaxies in the magnitude range $[M, M - dM]$, and define the luminosity function in terms of magnitudes, $\Phi_{\text{LF}}(M)$, such that $\Phi_{\text{LF}}(L)dL = \Phi_{\text{LF}}(M)d(-M)$. Isolating $\Phi_{\text{LF}}(M)$, carrying out the differentiation, and inserting $\frac{L}{L^*} = 10^{-0.4(M - M^*)}$ and 13.1, one finds the expression given in equation 13.2.

where M_{b_J} denotes the absolute magnitude of the galaxies in the b_J band, and $\Phi_{\text{LF}}^* = 0.0161 \text{ h}^3 \text{ Mpc}^{-3}$, $M_{b_J}^* = -19.66$, and $\alpha = -1.21$. This luminosity function has been corrected for the redshifting of light with the expansion, as well as for the galaxy evolution, and in these respects is therefore directly comparable to the luminosity function at $z = 0$ from Galacticus. Note, however, that the luminosities we obtain from Galacticus have not been corrected for the extinction of light by gas in the galaxies.

Another property of a galaxy population, which is especially important in the context of type Ia supernovae, is the stellar mass contained in the galaxies. We use the estimate of the stellar mass function, i.e. the number density of galaxies as a function of their stellar mass M_* , obtained in [120], in which a Schechter-function was fit to the stellar masses obtained from galaxies in the Sloan Digital Sky Survey. In the paper, the stellar masses of the galaxies are measured by using the templates from [121]. These templates are created using stellar population synthesis models, with the primary purpose of allowing observed spectra to be shifted between different bands, but as they need to make a physical interpretation of the data in terms of the stellar mass and star formation history of the galaxy, these are also provided by the templates. The fit to the stellar mass function obtained in [120] is

$$\Phi_{\text{SMF}}(M_*) = \Phi_{\text{SMF}}^* M_*^* \exp \left[-\frac{M_*}{M_*^*} \right] \left[\frac{M_*}{M_*^*} \right]^\alpha \frac{M_*}{h^2}, \quad (13.3)$$

with $\Phi_{\text{SMF}}^* = 0.0083 \text{ h}^3 / \text{Mpc}^3$, $M_*^* = 10^{10.525} \text{ M}_\odot / h^2$, and $\alpha = -1.155$.

In the top of figure 13.1, the luminosity functions and stellar mass functions of the galaxies identified by Galacticus in the five small test simulations of different spatial resolutions are shown. We examine in which galaxies most of the supernovae occur, by calculating the present day type Ia supernova rate in each galaxy using the method described in chapter 12. This is shown for one of the simulations in figure 13.2, which shows histograms over the absolute magnitudes and stellar masses of the galaxies, each weighted by its present day type Ia supernova rate. We find that type Ia supernovae tend to occur in galaxies with $M_{b_J} - 5 \log h < -16$ and a stellar mass greater than 10^8 M_\odot . As can be seen in figure 13.1, such galaxies are well resolved in the simulation which has a minimal halo mass of $6 \times 10^{10} \text{ M}_\odot / h$, corresponding to a mass resolution of 1600^3 particles in the box of side length $512 \text{ Mpc} / h$. In the bottom of figure 13.1, the comparison of simulations with different temporal resolutions is shown, revealing that this does not have any significant effect. We choose a temporal resolution of 45 snapshots, linearly spaced in scale factor from the beginning of the simulation at $z = 50$ to $z = 0$ for the simulation for the main analysis.

There appear to be too many galaxies with a high luminosity and a large stellar mass. The luminosity function has not been corrected for extinction of light by gas in the galaxies, which could partly explain the discrepancy between the measured and the predicted number of very luminous galaxies. As can be seen from figure 13.2, we find that the majority of type Ia supernovae comes from galaxies with an absolute magnitude in the b_J -band given by $M_{b_J} - 5 \log h > -21$ and a stellar mass below 10^{11} M_\odot . Therefore, we do not expect the over-representation of massive, luminous galaxies to have a significant effect on our results. .

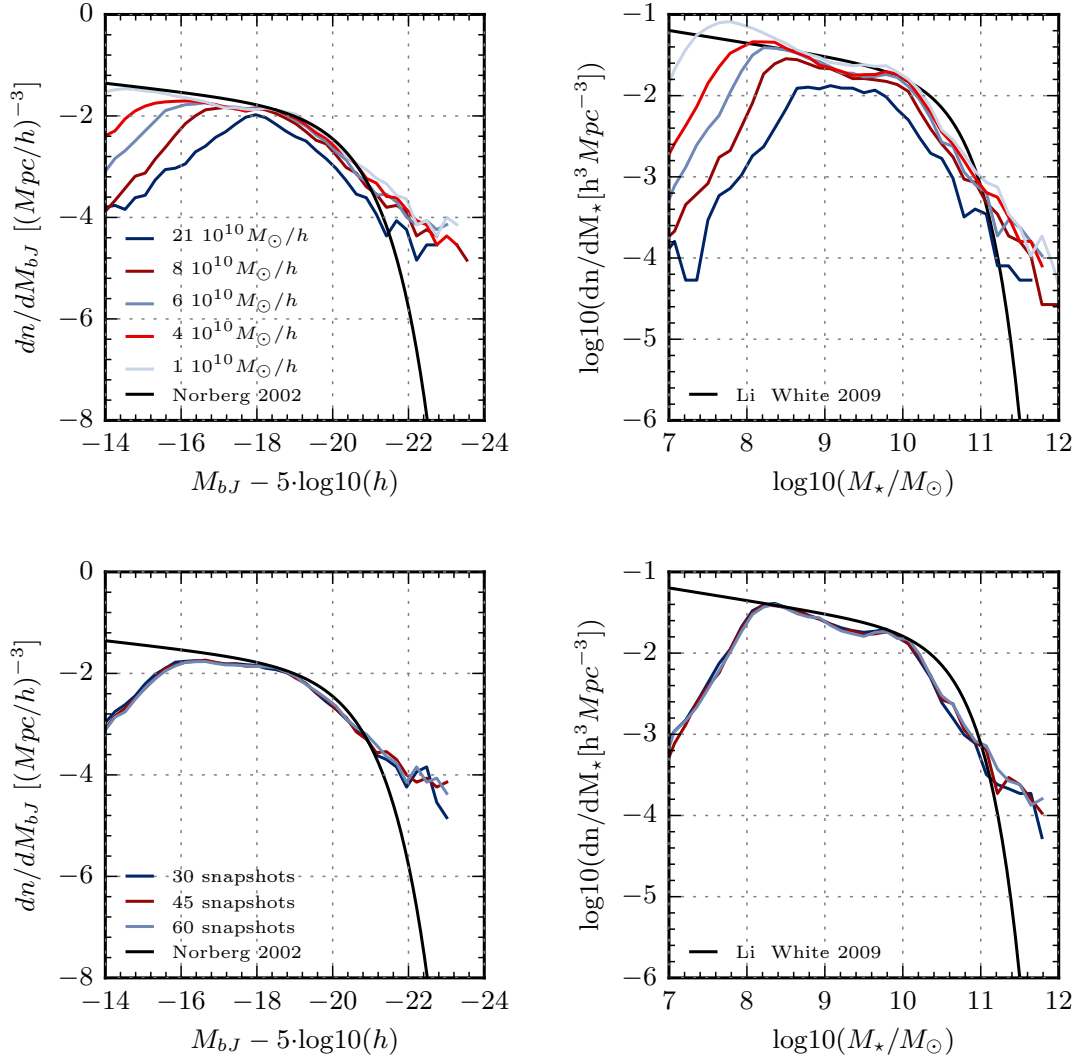


Figure 13.1: In order to determine the necessary resolution in mass and time for the N-body simulation, we compare the luminosity function and stellar mass function in the test simulations to observations. Specifically, we compare to the luminosity function of 2dF galaxies [119], and to the stellar mass function of SDSS galaxies [120]. The luminosity functions are shown on the **left panel**, and the stellar mass functions on the **right panel**. In the **top panel**, the simulations of different mass resolutions are compared. The resolutions are shown in the legend of the figure to the left, as the approximate mass of the least massive halo that can be identified in the given simulation (consisting of 20 particles). It is evident that increasing the resolution of the simulation affects the formation of small galaxies. In the **bottom panel**, the simulations of different temporal resolution are compared. This is found to make a negligible difference.

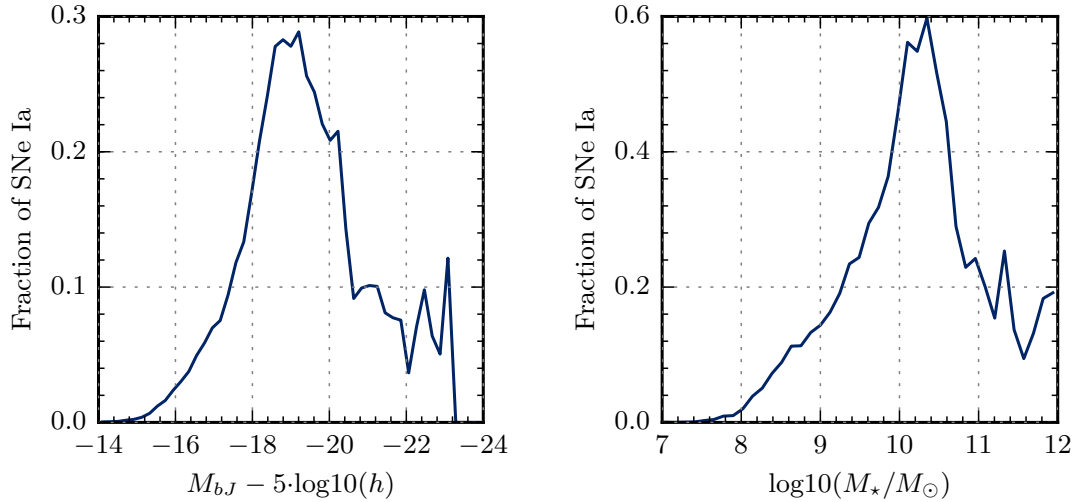


Figure 13.2: The frequency of supernovae as a function of galactic magnitude (**left**) and stellar mass (**right**), in a simulation of box size 64 Mpc/h. It is seen that most of the supernovae occur in galaxies with $M_{bJ} - 5 \log h > -21$, and a stellar mass less than $10^{11} M_\odot$. The total type Ia supernova rate in the box is $9.5 \times 10^{-5} \text{ SNe yr}^{-1} \text{ h}^3 \text{ Mpc}^{-3}$.

13.3 Mock observers and observations

For the purpose of testing the effect of the observer environment on the observed velocity field, we use two different sets of observers. One is selected as galaxies similar to the Milky Way, i.e. galaxies in which the majority of the stellar mass is found in the disk, and which are located in a dark matter halo with a mass in the range $10^{14} - 5 \times 10^{15} M_\odot$, which is similar to the mass of the Virgo Super Cluster. The other set of observers consists of positions distributed randomly throughout the simulation volume.

The box is taken to be periodic, and each of the observers identify supernovae out to a maximal distance equal to half the box size, that is 256 Mpc/h, corresponding to a redshift of $z = 0.087$.

In addition to the analysis based on the type Ia supernova rates produced from the star formation histories, we also perform an analysis based on the halo catalog at $z = 0$, where we choose the observed halos with a probability proportional to their mass. In the reference analysis, we bin the observations in redshift, but we also carry out an analysis where we bin in comoving distance. For all these analyzes, we use a survey geometry corresponding to that of the LSST main survey. In order to check the effects of the reconstruction of the full power spectrum from the partially observed sky, we also carry out an analysis where the full sky is observed. The different analyzes are summarized in table 13.2, where a naming scheme is also introduced. The distributions of observers and observed objects are illustrated in figure 13.3.

The separation of the surveyed volume into separate distance bins is illustrated in figure 13.4. The

Name	Observers	Observations	Binning	Geometry
Ref	MW like galaxies	SN Ia rates	z	LSST
Full	MW like galaxies	SN Ia rates	z	Full
RndPos	Random positions	SN Ia rates	z	LSST
Hmw	MW like galaxies	Halo masses	z	LSST
Binr	MW like galaxies	SN Ia rates	r	LSST

Table 13.2: Choices for the observers and the observed objects, also introducing a naming scheme for the different analyzes.

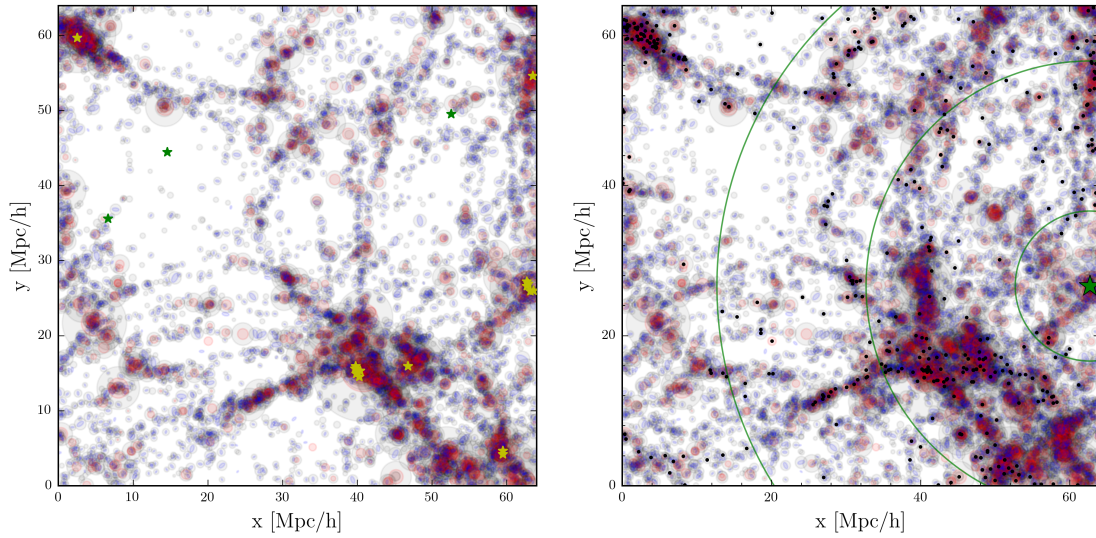


Figure 13.3: **Left:** An illustration of the dark matter halos (transparent black circles), the elliptical galaxies (red circles) and the disk galaxies (blue disks), along with two different sets of observers: The yellow stars mark observers in disk galaxies, located in halos of a mass similar to that of the Virgo Super Cluster, and the green star marks the same number of observers, distributed randomly in the box. The sizes of the halos and galaxies are proportional to the cubic root of their masses, with the disks plotted 5 times greater than the elliptical galaxies and 10 times greater than the dark matter halos. **Right:** An illustration of the observations (black dots) performed by the observer located at the green star, distributed in bins separated by the green circles.

observations are distributed in the bins according to their measured redshift, which is converted to a comoving distance assuming that it is purely cosmological, i.e. stemming from the expansion of the universe. This introduces an error in the binning of observed objects. The significance of this error is studied by including an analysis in which the observed objects are distributed in bins according to their true comoving distance rather than their measured redshifts.

When the shells in which we want to measure the velocity field has been selected, a pixelation scheme needs to be specified for each shell. We use the HEALPix pixelation scheme [122], in which the number of pixels on the sphere is $N_{\text{pix}} = 12 \cdot n_{\text{side}}^2$, and the parameter n_{side} has to be chosen as an integer power of 2. An example of the pixelation is shown in figure 13.5, which shows the

average number of supernovae per year in each pixel in a shell at 140 – 160 Mpc/h, for one of the observers. This also serves to show the geometry of the survey.

The number of supernovae observed by each observer is calculated from the total rate of type Ia supernovae in the region he observes, assuming he observes every supernova within a period of 10 years. As the average rate of type Ia supernovae in the main simulation is $1.1 \times 10^{-4} \text{ SNe yr}^{-1} \text{ h}^3 \text{ Mpc}^{-3}$, as mentioned in chapter 12, this corresponds to approximately 35 000 supernovae within the survey volume and in the distance range 40 – 256 Mpc/h.

The surveyed volume is separated in to shells at different redshifts. Since the volumes of shells increase with redshift for a given bin width, different resolutions can be obtained in different shells. We find that with a mean of approximately 5 observations per pixel, there are relatively few empty pixels in the survey. To reach as high a pixel-resolution as possible, we divide the survey into three regimes with n_{side} equal to 4, 8, and 16 respectively, as illustrated in figure 13.4, allowing us to resolve significantly higher multipoles in the outermost than in the innermost bins.

13.4 The angular velocity power spectrum

In each shell, the radial peculiar velocities define a function on the sphere, which can be expanded in spherical harmonics:

$$v_r(\hat{\mathbf{r}}) = \sum_{l=0}^{\infty} \sum_{m=-l}^l a_{lm} Y_{lm}(\hat{\mathbf{r}}), \quad (13.4)$$

where $\hat{\mathbf{r}}$ is a unit vector identifying a point on the sphere. There are $2l + 1$ modes for each l , and the average power corresponding to a given value of l is therefore

$$C_l = \frac{1}{2l + 1} \sum_m |a_{lm}|^2. \quad (13.5)$$

To obtain this power spectrum, we use the Healpy version of the HEALPix package, developed to carry out harmonic analyzes of the CMB⁴. This uses the assumption that there is insignificant power in modes with $l > l_{\text{max}}$, as will be the case for the smoothed velocity fields, so that the first sum in e.g. 13.4 can be terminated at $l = l_{\text{max}}$:

$$v_r(\hat{\mathbf{r}}) = \sum_{l=0}^{l_{\text{max}}} \sum_{m=-l}^l a_{lm} Y_{lm}(\hat{\mathbf{r}}).$$

The pixelation scheme is then used to define N_{pix} locations in which the field is sampled, and the sampled values are used to estimate the coefficients of the expansion as

$$\hat{a}_{lm} = \frac{4\pi}{N_{\text{pix}}} \sum_{p=0}^{N_{\text{pix}}-1} Y_{lm}^*(\hat{\mathbf{r}}_p) v_r(\hat{\mathbf{r}}_p),$$

⁴See <http://healpix.sourceforge.net> for a discussion of the HEALPix conventions.

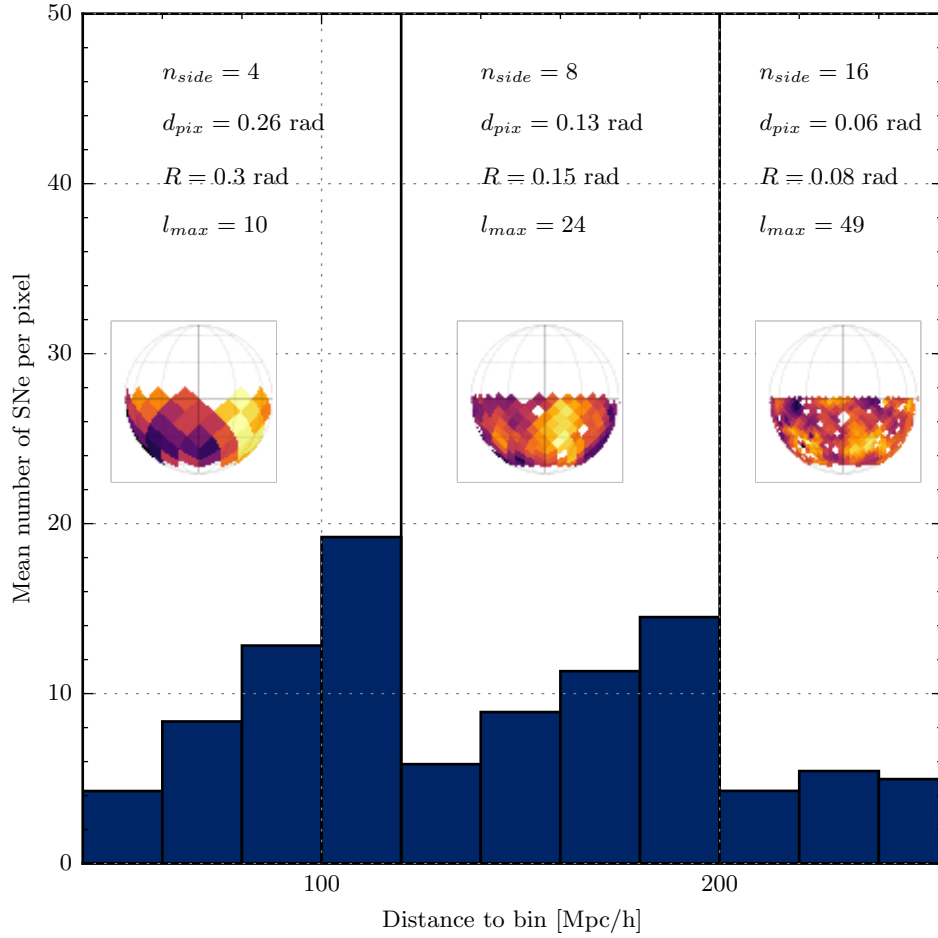


Figure 13.4: The average number of supernovae per pixel in each of the three resolution-regimes. The inset shows an example of a velocity field in a bin from each regime, as an illustration of the pixelation. In each regime, the velocity field is described by its values in $12 \cdot n_{side}^2$ pixels, with each pixel having a size of d_{pix} . It is smoothed with a Gaussian of FWHM given by R , which determines the highest multipole moments that can be determined in each regime, l_{max} .

where $\hat{\mathbf{r}}_p$ is the direction to the pixel denoted by p . From these estimated coefficients, the power spectrum can be obtained from equation 13.5.

Since we are interested in the *fluctuations* in the peculiar velocity field, and since the dipole cannot be reliably estimated due to the survey geometry, we use the option in HEALPix to remove the best-fit monopole and dipole before calculating the rest of the power spectrum.

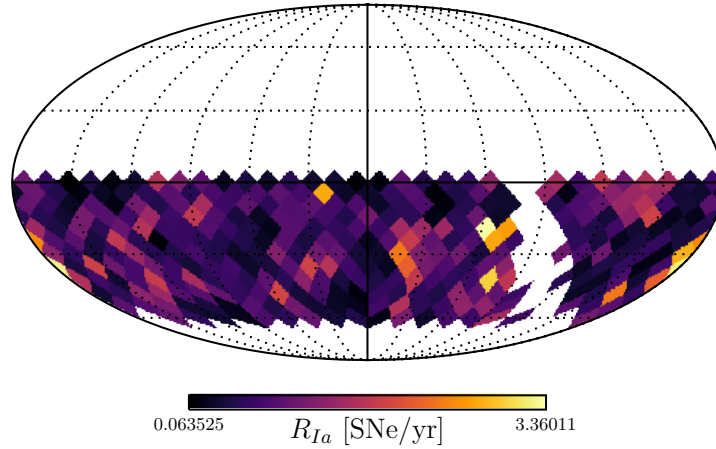


Figure 13.5: The type Ia supernova rate in each pixel in a shell at 140 Mpc/h – 160 Mpc/h, using the HEALPix pixelation scheme with $n_{\text{side}} = 8$. Only the part of the sky that will be covered with the LSST main survey is shown – the white stripe at the right is the galactic plane.

13.4.1 Smoothing of the velocity field

Due to the survey geometry, the first multipoles of the expansion cannot be reliably estimated in the survey. At the other end of the spectrum, the resolution, determined by the largest hole in the sky cover or the pixel size, sets an upper limit to the multipoles that can be determined. In order to reduce noise from sub-resolution variations, we use the Healpix smoothing-function to smooth the field with a Gaussian beam of FWHM as specified in figure 13.4. To illustrate the effect of smoothing, we show in figure 13.6 the power spectrum for one of the central bins (140 – 160 Mpc/h), after it has been smoothed with four different smoothing scales of respectively 0.1 rad, 0.15 rad, 0.2 rad, and 0.3 rad. The figure also shows the map of radial velocities for an example observer before and after smoothing.

13.4.2 Correcting for mode-coupling due to incomplete sky coverage

We use the MASTER correction procedure, described in [123], to correct for the missing sky coverage in the LSST survey geometry. Here, we describe the general idea, and sketch the mathematics behind the method. For a full derivation, see the paper.

Given a function defined on the entire sphere, such as the radial velocity field v_r , and a window function W which describes where the function has been sampled (in this case the survey geometry of the LSST main survey), we can expand the part of the function that has been observed in

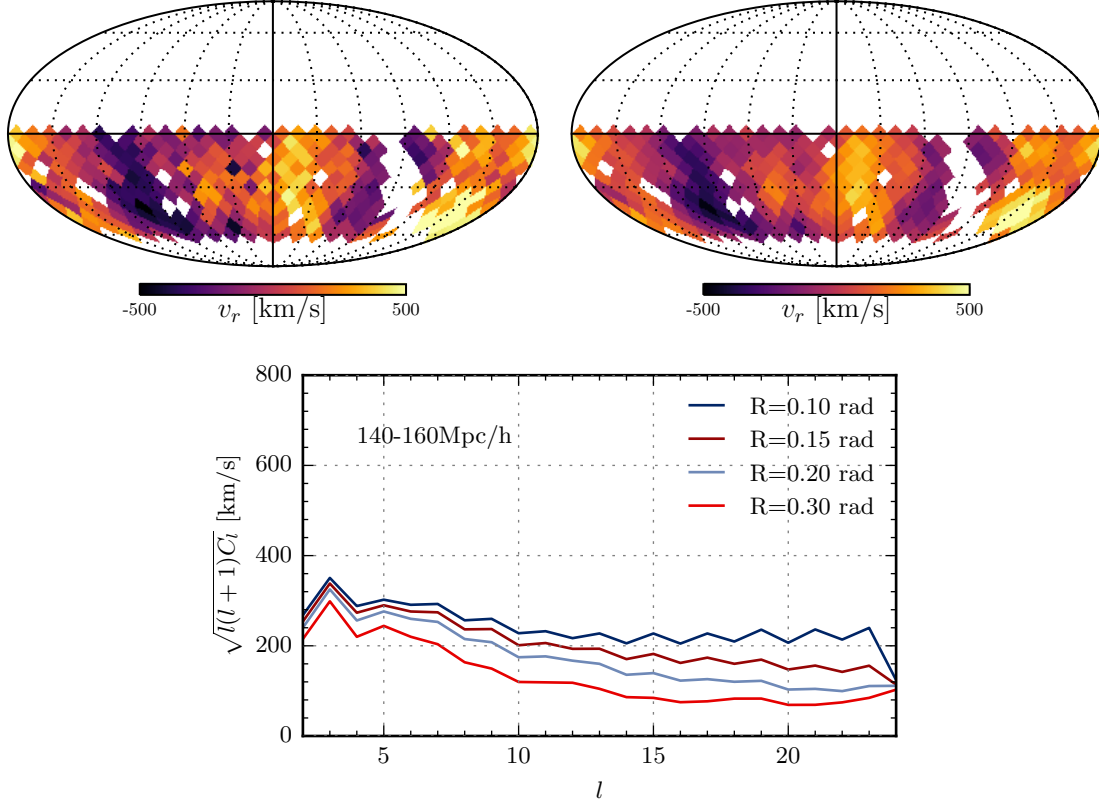


Figure 13.6: **Top:** Velocity field at 140 – 160 Mpc/h before (**left**) and after (**right**) smoothing with a Gaussian of FWHM $R = 0.15$ rad. **Bottom:** The mean power spectrum among the observers from a velocity field smoothed at the four different scales shown in the legend.

spherical harmonics, Y_{lm} , as

$$\tilde{a}_{lm} = \int d\hat{\mathbf{r}} v_r(\hat{\mathbf{r}}) W(\hat{\mathbf{r}}) Y_{lm}^*(\hat{\mathbf{r}}) \quad (13.6)$$

$$= \sum_{l'm'} a_{l'm'} \int d\hat{\mathbf{r}} Y_{l'm'}(\hat{\mathbf{r}}) W(\hat{\mathbf{r}}) Y_{lm}^*(\hat{\mathbf{r}}). \quad (13.7)$$

In the second line, the expansion of the full function in spherical harmonics as given in equation 13.4 has been inserted. The integral in the second line describes how the different spherical harmonics couple to each other through the window function. By also expanding the window function in spherical harmonics, $W(\hat{\mathbf{r}}) = \sum_{lm} w_{lm} Y_{lm}(\hat{\mathbf{r}})$, this can be expressed as

$$\int d\hat{\mathbf{r}} Y_{l'm'}(\hat{\mathbf{r}}) W(\hat{\mathbf{r}}) Y_{lm}^*(\hat{\mathbf{r}}) = \sum_{l_3 m_3} w_{l_3 m_3} \int d\hat{\mathbf{r}} Y_{l_1 m_1}(\hat{\mathbf{r}}) Y_{l_3 m_3}(\hat{\mathbf{r}}) Y_{l_2 m_2}^*(\hat{\mathbf{r}}). \quad (13.8)$$

The integral in the last expression describes the coupling between a set of spherical harmonics, and this can be expressed in terms of Clebsch-Gordan coefficients.

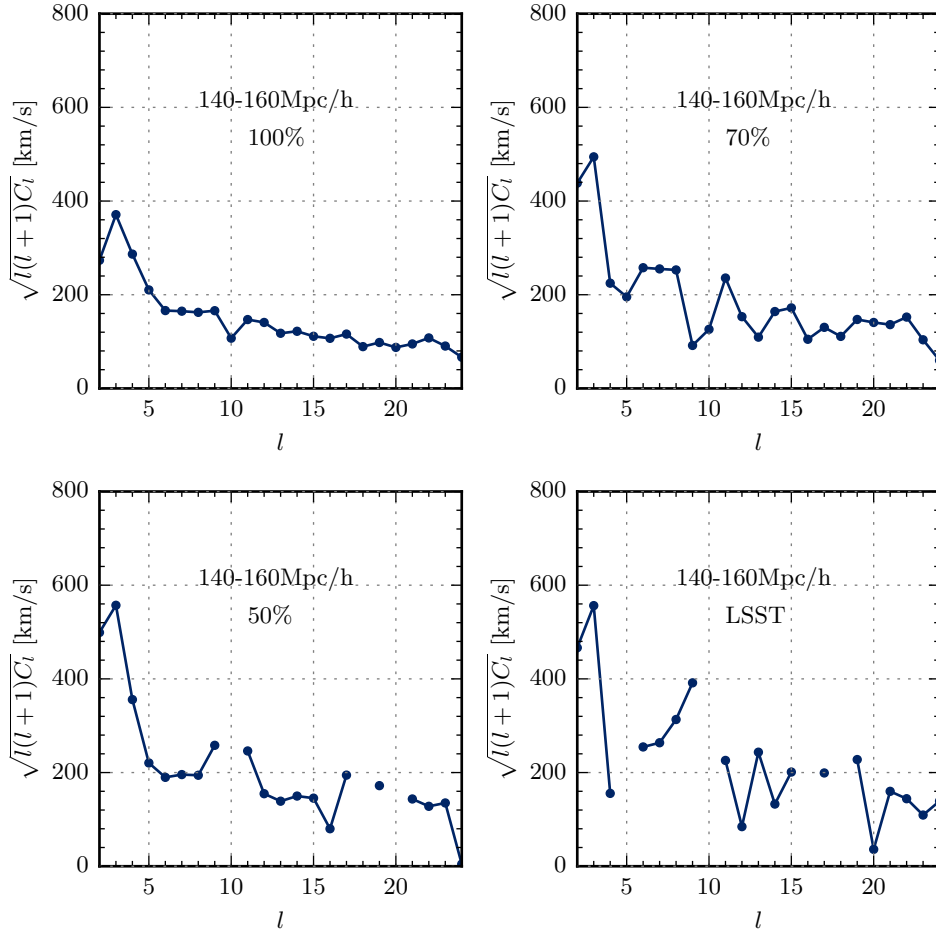


Figure 13.7: The angular power spectrum for a specific observer, based on four different survey geometries: observation of the full sky (**top left**), excluding a cap around the north pole so that only 70% of the sky is observed (**top right**), excluding the entire northern hemisphere (**bottom left**), and using the survey geometry of the LSST survey (**bottom right**). As the unobserved part of the sky grows, the correction procedure starts to fail at a number of l -values, resulting in negative (and unphysical) values for C_l . These are not plotted.

The coefficients of the multipole expansion of the observed part of the function, as given in equation 13.7, define the so-called pseudo power spectrum:

$$\tilde{C}_l \equiv \frac{1}{2l+1} \sum_{m=-l}^l |\tilde{a}_{lm}|^2. \quad (13.9)$$

Ideally, we would like to be able to reproduce the power spectrum of the full sky, the C_l 's defined in equation 13.5, from the pseudo power spectrum and the coupling of modes introduced by the window function. However, this is not possible, since the available information tells us nothing

about the unobserved part of the sky. But by assuming that the fluctuations of the field we are describing follows a Gaussian distribution, we can learn something about this underlying distribution. If the fluctuations of the field are pulled from a Gaussian, the a_{lm} 's must be so as well, and since the monopole is zero, $\langle a_{lm} \rangle = 0$, the variance and covariance of the coefficients can be calculated as $\langle a_{lm} a_{l'm'} \rangle = \delta_{ll'} \delta_{mm'} \langle C_l \rangle$. Here, $\langle C_l \rangle$ is the true variance of a_{lm} , or equivalently, the ensemble average of C_l for all the fluctuation fields corresponding to a given cosmological model. By taking the ensemble average of equation 13.9, inserting the expressions from equations 13.7 and 13.8, and using the orthogonality relations of the Clebsh-Gordan coefficients and the diagonality of $\langle C_l \rangle$, one can show that the ensemble averages of the true and pseudo power spectra are related by

$$\langle \tilde{C}_{l_1} \rangle = \sum_{l_2} M_{l_1 l_2} \langle C_{l_2} \rangle. \quad (13.10)$$

Here, $M_{l_1 l_2}$ is the so-called MASTER matrix, given as a sum over Clebsh-Gordan coefficients and the power spectrum for of window function, \mathcal{W}_l , as

$$M_{l_1 l_2} = \frac{2l_2 + 1}{4\pi} \sum_{l_3} (2l_3 + 1) \mathcal{W}_{l_3} \begin{pmatrix} l_1 & l_2 & l_3 \\ 0 & 0 & 0 \end{pmatrix}^2, \quad (13.11)$$

where the matrix is the Wigner-symbol for the Clebsh-Gordan coefficients.

In figure 13.7, we show how well the MASTER correction procedure works. The figure shows the measured angular velocity power spectrum in a shell at 140 – 160 Mpc/h for an example observer. The power spectrum has been determined using four different survey geometries: the first one covering the full sky (in which case no correction procedure is necessary), the second and third covering respectively 70% and 50% of the sky, and the last one corresponding to the geometry of the LSST main survey. For the three partial surveys, the MASTER method has been used to correct for the missing sky coverage. It is seen that the larger the unobserved part of the sky, the less reliable the multipole expansion becomes. And for a number of multipoles, the recovered power is found to be negative (and unphysical), a result of the MASTER matrix being close to singular when a large portion of the sky is unobserved. However, as we will see in the next section, the mean of the recovered power spectra among all the observers is found to agree well with the spectra measured from the full sky, as the derivation of the MASTER method predicts.

13.5 Results and discussion

In figure 13.8 we display the results of the multipole analysis of the radial velocity field for the reference analysis, i.e. the analysis that most closely corresponds to the observations carried out by observers in Milky Way-like galaxies, and for the survey with full sky coverage. The mean of the power spectrum among the observers for all bins and all l -values in each of the two cases is displayed as a contour plot. The peak of the power spectrum moves to higher l for increasing redshift. This is as expected, as a given length scale corresponds to increasing values of l , as

the distance to the shells increase⁵. It is apparent that there is some artifact around $l = 3$, corresponding to the octopole of the expansion, for the reference analysis. This is caused by the correction procedure, and is therefore a result of the survey geometry, as can be seen by comparing with the power spectrum obtained from the full sky analysis, where this does not occur.

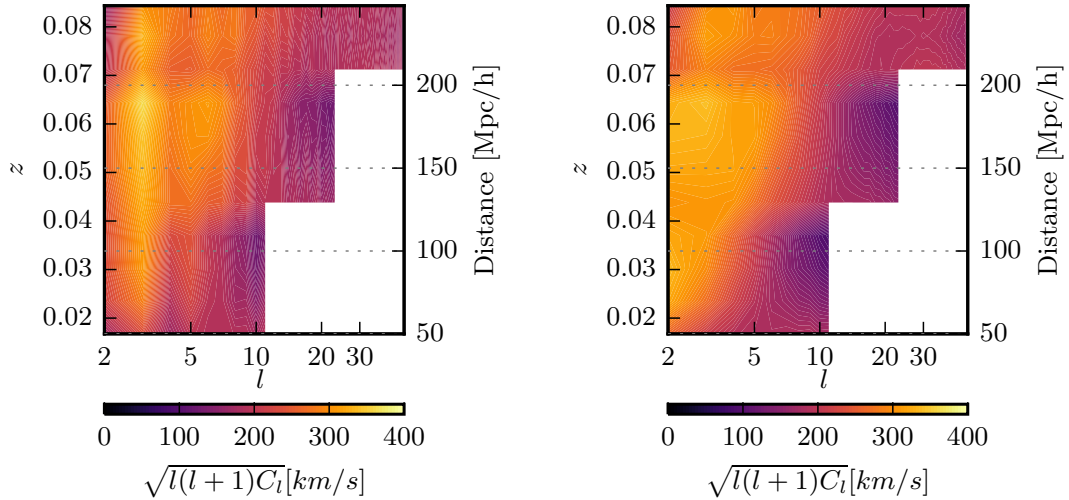


Figure 13.8: Contour plots showing the mean angular power as a function of both z and l in the reference scenario (**left**) and in the case of full sky coverage (**right**). Note that the l -axis is logarithmic. The peak at $l = 3$ in the reference scenario is an artifact caused by the survey geometry, which prevents reliable estimates to be made of the lowest multipoles. This can be seen by comparison with the full sky power spectrum, for which the peak does not appear.

In the previous section, we described the MASTER correction procedure, and used it to recover the power spectrum from a single observer. In figure 13.9, the correction procedure is tested on the total set of 1000 reference observers. This is done by comparing the mean and spread in the power spectra measured with full sky coverage for all the observers, with the mean and spread among the power spectra measured by the same observers when the LSST survey geometry is used, and the MASTER method is used to correct for missing sky coverage. Good agreement is found between the mean of the angular power spectra among the observers for the two cases, as predicted in the derivation sketched in section 13.4.2. There is a large increase in the spread in the recovered power spectra, as compared to that measured from the full sky. This is expected, since the recovered power spectra are constructed from a much smaller amount of information.

In figure 13.10, we compare the mean and spread of the power spectrum from the reference analysis to those obtained by varying three different aspects of the analysis, as explained in section 13.3 and summarized in table 13.2. The differences in the mean for each of the studied cases

⁵The physical scale corresponding to a given value of l can be estimated by remembering that each spherical harmonic oscillates l times over the sphere, so the wavelength of an oscillation at a shell at distance r can be obtained as $\lambda = 2\pi r/l$.

from the reference power spectrum are shown in figure 13.11. This shows how different aspects of the analysis affect the measurements of the power spectra. The biggest difference occurs for the analysis based on the halo catalogs, where the supernovae are chosen among the halos with a probability proportional to the halo masses (Hmw). In this analysis, the power is underestimated for large scales (small values of l), and overestimated for small scales (large values of l), with the transition happening around fluctuations of a wavelength of $\lambda \sim 95 \text{ Mpc/h}$. The positions of the observers do not make any significant difference, implying that the velocity power spectrum is insensitive to effects from the environment. The error associated with the binning procedure is largest at small l -values and large scales, and tends to zero around l -values corresponding to fluctuations with a wavelength of about $\lambda \sim 50 \text{ Mpc/h}$.

We have not considered the error stemming from the uncertainty in the measurements of type Ia supernova luminosities and redshifts of galaxies, only the uncertainty from the distribution of supernovae and the survey geometry, which is referred to as the "geometric error" in [89], and cosmic variance. According to figure 2 in [89], geometric errors dominate for multipoles with $l \lesssim 10$. By comparing our results for the uncertainty in the measured power spectrum to figure 3 in [89] for $l \lesssim 10$, we conclude that our results confirm their finding of the precision with which the angular velocity power spectrum can be determined, and therefore, their conclusions are backed by this study. This implies that their result from the likelihood analysis applies for the distribution of supernovae and survey geometry considered in this study as well. As they find that the angular velocity power spectrum can be used to determine σ_8 with 3-5% accuracy at 95% confidence, we expect the velocity field from type Ia supernovae to become an independent probe of this and other parameters associated with the matter distribution in the near future. We will explore this further in a future paper.

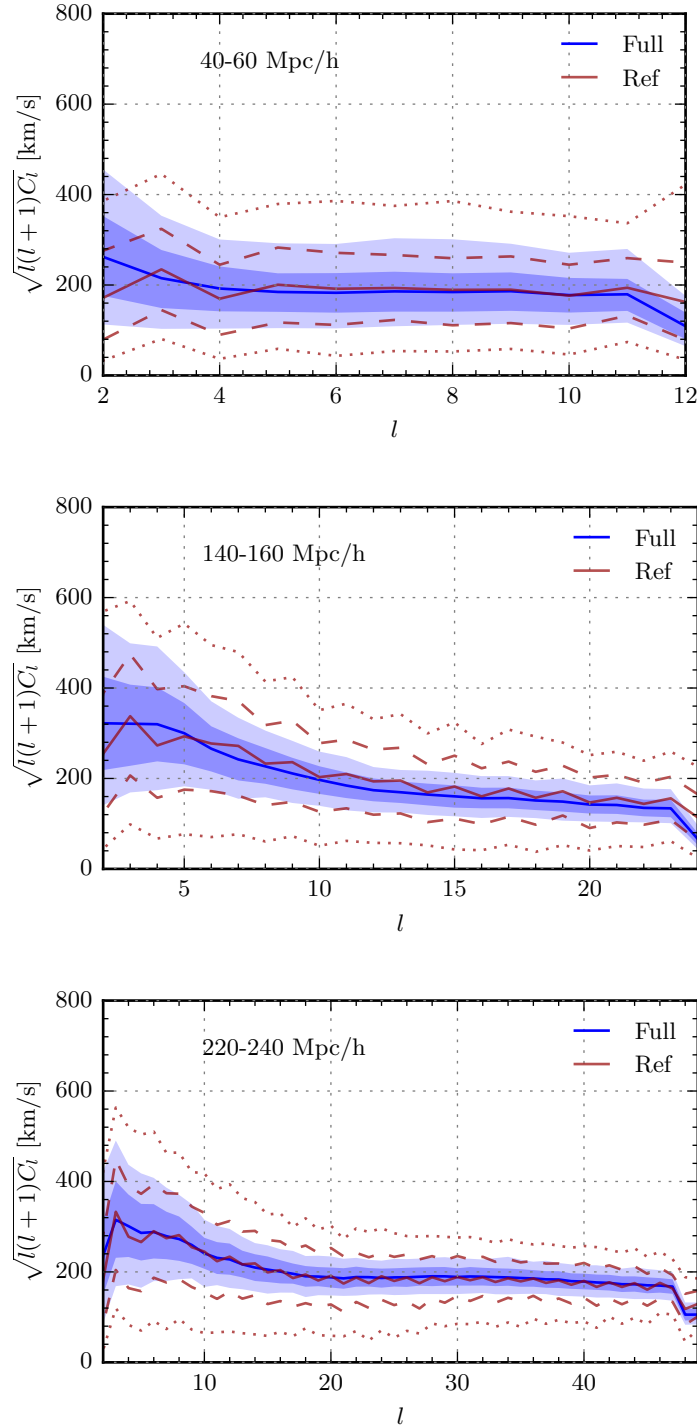


Figure 13.9: In this figure, the correction procedure is tested on the total set of 1000 reference observers. This is done by comparing the mean and spread of the velocity power spectrum determined from a survey with full sky coverage (blue) with that obtained using the LSST survey geometry, and using the correction matrix to recover the power spectrum (red). The full lines show the mean among all the observers, while the 68% and 95% confidence areas are shown in blue shading and dashed lines. The spectra are shown for a bin at 40 – 60 Mpc/h (**top**), a bin at 140 – 160 Mpc/h (**middle**) and a bin at 220 – 240 Mpc/h (**bottom**). In mean, the correction procedure does a pretty good job. However, it results in a big increase in the spread in the power spectra among the observers.

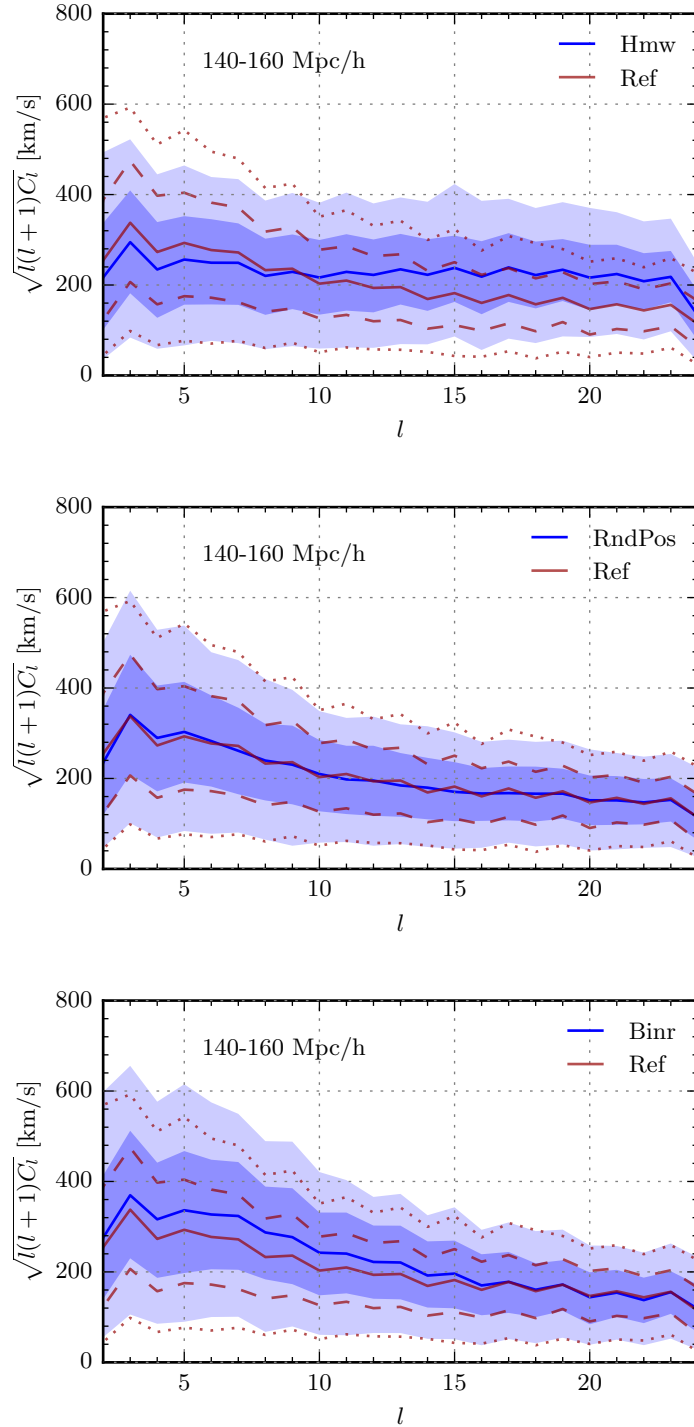


Figure 13.10: The angular power spectra in a bin at 140 – 160 Mpc/h, showing how the measured velocity power spectrum depends on three different aspects of the analysis. In each case, the mean, 68%, and 95% confidence intervals among the observers are shown with a blue line and blue shadings, respectively, and the result for the reference analysis is shown with red lines for comparison. **Top:** Analysis based on a mass weighted selection of supernovae from a halo catalog. **Middle:** Analysis based on observers distributed randomly throughout the simulation volume. **Bottom:** Analysis in which the observations are binned in distance rather than redshift.

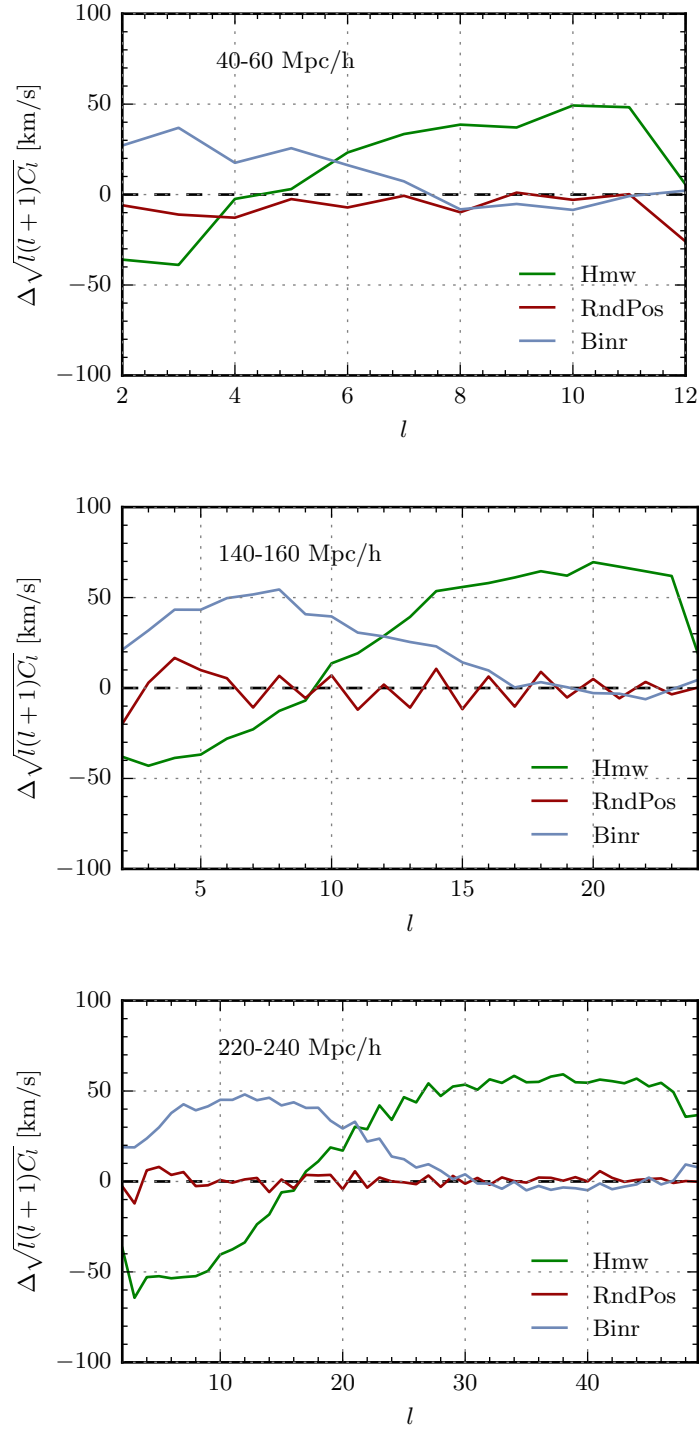


Figure 13.11: The mean deviation from the reference analysis, in bins at respectively 40 – 60 Mpc/h (**top**), 140 – 160 Mpc/h (**middle**), and 220 – 240 Mpc/h (**bottom**). The observations based on the halo catalog underpredicts the power at large scales, and overpredicts the power at small scales, whereas binning in distance rather than redshift results in an increased power on large scales. The position of the observer does not seem to affect the power spectrum in any significant way.

13.6 Conclusions

We have studied the potential for measuring the power spectrum of radial peculiar velocities from type Ia supernovae in an LSST-like sky survey. The analysis shows that we can reasonably correct for the effects of missing sky cover due to the survey geometry, though with a penalty in the form of a large increase in the uncertainty of the measured spectrum. By carrying out the analysis for observers in different environments, we have found that the observer position does not cause any significant bias in the measured velocity power spectrum. On the other hand, we have seen that the procedure used for selecting the supernovae from which the velocity field is measured has a relatively large effect, implying that analyzes based on inaccurate distributions of supernovae will produce somewhat biased results. Likewise, the choice for how the measurements are binned can have a significant effect on the results.

As discussed in chapter 10, the method studied here can be used to measure parameters associated with the matter distribution. By comparing our results with those obtained in [89], we conclude that the velocity field from type Ia supernovae will be able to provide estimates of σ_8 with a precision comparable to what can be obtained from measurements of the galaxy power spectrum or weak lensing (see for example [124, 125]). As the most recent value determined from the CMB points to a much higher value of this parameter than analysis of weak lensing alignment of galaxies [126, 127], this might become valuable as a complimentary way to measure this parameter in the near future.

Part IV

Outlook and conclusions

Chapter 14

Outlook and conclusions

14.1 Parameter forecast with the angular power spectrum of radial peculiar velocities

Building on the catalogs and methods described in the previous chapters, we plan to carry out a forecast, predicting how well the angular power spectrum of peculiar velocities can be used to measure cosmological parameters. As we have seen in chapter 10, the 3D power spectrum of peculiar velocities is related to the matter power spectrum through the Hubble parameter and the growth rate, i.e.

$$P_v(k) = H^2 f^2 k^{-2} P_m(k). \quad (14.1)$$

Equation 10.1 for the Fourier components of the velocity field can be used to calculate the correlation function between radial peculiar velocities of galaxies at some distance x . After some manipulation, this reveals that the coefficients of the angular peculiar velocity field are related to the 3D velocity power spectrum as [15, 128]

$$C_l = \frac{4\pi}{2l+1} (l\mathcal{B}_{l-1} + (l+1)\mathcal{B}_{l+1}), \quad \text{where} \quad \mathcal{B}_l = 4\pi \int \frac{k^2 dk}{(2\pi)^3} P_v(k) j_l(kx)^2, \quad (14.2)$$

with j_l being the l th spherical Bessel function. Equations 14.1 and 14.2 show how the coefficients of the angular power spectrum of radial peculiar velocities are related to the matter power spectrum and the growth rate in linear theory. And since the growth rate is a function of Ω_m , and the amplitude of the matter power spectrum is determined by σ_8 , a measurement of the angular velocity power spectrum will allow estimation of these two parameters.

To obtain accurate predictions for the uncertainty in the measured parameters, and to avoid bias, it is important to take account of the correlations of the power measured in different redshift bins and for different multipoles. As we saw in the last chapter, the missing sky coverage induces a coupling between the different l -modes of the measured velocity field. The coupling is strongest for adjacent l -values, which will therefore be most correlated. This effect can be somewhat reduced by binning the power spectrum in l .

The noise in the measured power spectra stems primarily from the luminosity scatter of the type Ia supernovae, which is many times greater than the uncertainty in the spectroscopically measured redshifts and the angular positions of the galaxies. This can be modeled as in [89], by adding a normally distributed noise to the magnitudes of the observed supernovae. By generating many realizations of this noise, and calculating the power spectra on the cut sky just as was done for the peculiar velocities in the previous chapter, the average noise power spectrum can be obtained. According to [123], by subtracting this from the pseudo power spectra measured by the individual observers, and subsequently applying the binning operator as well as correcting for missing sky coverage and smoothing effects, unbiased estimates for the noise-corrected and binned full-sky power spectra are obtained. These estimates for the power in different l -bins and in different redshift shells will constitute the data that our parameters will be estimated from.

The covariance matrix needs to be estimated from a different simulation than the one our parameter forecast is based on, to mimic the situation from actual observations. It can be measured by acquiring several realizations of the noise-corrected and binned full-sky power spectra, and measuring the covariances among them [123, 129]. In our case, these realizations are obtained from differently located observers in the extra N-body simulation, thereby including the contributions to the covariance matrix from cosmic variance, binning in redshift, and the finite thickness of the shells, as well as the coupling between the different multipoles induced by the missing sky cover.

14.2 Summary and conclusions

This thesis has considered effects of cosmic structure formation and the resulting peculiar velocities of galaxies. We started out describing the basic model for the evolution of the universe and structures within it, and then saw how this can be used for a numerical treatment of the physical processes involved. These tools were then applied to the problem of the discrepancy between local and global estimates of the Hubble constant, which lead to the conclusion that it is extremely unlikely for the local value to deviate from the global value as much as required to reconcile recent estimates of the expansion rate with each other.

We then considered how well peculiar velocities measured from type Ia supernovae in upcoming surveys can be used for measurements of the angular power spectrum of radial, peculiar velocities. For this purpose, we populated a large N-body simulation with type Ia supernovae based on the star formation rates obtained from a code for semi-analytical modeling of galaxy formation. Based on this study, we concluded that the angular velocity power spectrum can be recovered to an accuracy that likely permits fairly accurate estimates of Ω_m and σ_8 . This subject will be further investigated in the near future.

Bibliography

- [1] Io Odderskov, Steen Hannestad, and Troels Haugbølle. “On the local variation of the Hubble constant”. In: *J. Cosmol. Astropart. Phys.* (2014). ISSN: 1475-7516. DOI: 10.1088/1475-7516/2014/10/028. URL: <http://dx.doi.org/10.1088/1475-7516/2014/10/028>.
- [2] Io Odderskov, Marco Baldi, and Luca Amendola. “The effect of interacting dark energy on local measurements of the Hubble constant”. In: *J. Cosmol. Astropart. Phys.* 2016.05 (May 2016), pp. 035–035. DOI: 10.1088/1475-7516/2016/05/035. URL: <http://dx.doi.org/10.1088/1475-7516/2016/05/035>.
- [3] I. Odderskov, S. M. Koksang, and S. Hannestad. “The Local Value of H_0 in an Inhomogeneous Universe”. In: *JCAP* 02(2016)001 (Jan. 2016), p. 02001. DOI: 10.1088/1475-7516/2016/02/001. eprint: 1601.07356.
- [4] Io Odderskov and Steen Hannestad. “Measuring the velocity field from type Ia supernovae in an LSST-like sky survey”. In: *ArXiv e-prints* (Aug. 2016). eprint: 1608.04446.
- [5] “The Nobel Prize in Physics 2011 - Advanced Information”. *Nobelprize.org. Nobel Media AB 2014. Web. 28 Aug 2016.* http://www.nobelprize.org/nobel_prizes/physics/laureates/2011/advanced.html.
- [6] G. Gamow. “Expanding Universe and the Origin of Elements”. In: *Phys. Rev.* 70.7-8 (Oct. 1946), pp. 572–573. DOI: 10.1103/physrev.70.572.2. URL: <http://dx.doi.org/10.1103/PhysRev.70.572.2>.
- [7] Ralph A. Alpher and Robert C. Herman. “Remarks on the Evolution of the Expanding Universe”. In: *Phys. Rev.* 75.7 (Apr. 1949), pp. 1089–1095. DOI: 10.1103/physrev.75.1089. URL: <http://dx.doi.org/10.1103/PhysRev.75.1089>.
- [8] “Press Release: The 1978 Nobel Prize in Physics”. *Nobelprize.org. Nobel Media AB 2014. Web. 31 Aug 2016.* http://www.nobelprize.org/nobel_prizes/physics/laureates/1978/press.html.
- [9] Alan H. Guth. “Inflationary universe: A possible solution to the horizon and flatness problems”. In: *Physical Review D* 23.2 (Jan. 1981), pp. 347–356. DOI: 10.1103/physrevd.23.347. URL: <http://dx.doi.org/10.1103/PhysRevD.23.347>.

- [10] "The Nobel Prize in Physics 2006 - Advanced Information". *Nobelprize.org. Nobel Media AB 2014. Web. 28 Aug 2016.* http://www.nobelprize.org/nobel_prizes/physics/laureates/2006/advanced.html.
- [11] F. Zwicky. "On the Masses of Nebulae and of Clusters of Nebulae". In: *ApJ* 86 (Oct. 1937), p. 217. DOI: 10.1086/143864. URL: <http://dx.doi.org/10.1086/143864>.
- [12] Adam G. Riess et al. "Observational Evidence from Supernovae for an Accelerating Universe and a Cosmological Constant". In: *Astron.J.* 116:1009-1038,1998 (*Astron.J.*116:1009-1038,1998). DOI: 10.1086/300499. eprint: astro-ph/9805201.
- [13] Brian P. Schmidt et al. "The High-Z Supernova Search: Measuring Cosmic Deceleration and Global Curvature of the Universe Using Type Ia Supernovae". In: *Astrophys.J.* 507 (1998), pp. 46–63. DOI: 10.1086/306308. eprint: astro-ph/9805200.
- [14] S. Perlmutter et al. "Measurements of Omega and Lambda from 42 High-Redshift Supernovae". In: *Astrophys.J.* 517:565-586,1999 (*Astrophys.J.*517:565-586,1999). DOI: 10.1086/307221. eprint: astro-ph/9812133.
- [15] Scott Dodelson. *Modern Cosmology*. Academic Press, 2003. ISBN: 0122191412. URL: <http://www.amazon.com/Modern-Cosmology-Scott-Dodelson/dp/0122191412>.
- [16] E. Hubble. "A relation between distance and radial velocity among extra-galactic nebulae". In: *Proceedings of the National Academy of Sciences* 15.3 (Mar. 1929), pp. 168–173. DOI: 10.1073/pnas.15.3.168. URL: <http://dx.doi.org/10.1073/pnas.15.3.168>.
- [17] H. S. Leavitt and E. C. Pickering. "Periods of 25 Variable Stars in the Small Magellanic Cloud." In: *Harvard College Observatory Circular* 173 (Mar. 1912), pp. 1–3.
- [18] Barbara Ryden. *Introduction to Cosmology*. Addison-Wesley, 2002. ISBN: 0805389121. URL: <http://www.amazon.com/Introduction-Cosmology-Barbara-Ryden/dp/0805389121>.
- [19] Marc Davis and Adi Nusser. "Re-examination of Large Scale Structure and Cosmic Flows". In: *Proceedings of IAU Symposium* (Oct. 2014). eprint: 1410.7622.
- [20] Lam Hui and Patrick B. Greene. "Correlated Fluctuations in Luminosity Distance and the (Surprising) Importance of Peculiar Motion in Supernova Surveys". In: *Phys.Rev.D* 73:123526,2006 (*Phys.Rev.D*73:123526,2006). DOI: 10.1103/PhysRevD.73.123526. eprint: astro-ph/0512159.
- [21] Phillip James Edwin Peebles. *Principles of Physical Cosmology*. Princeton University Press, 1993.
- [22] James Binney and Scott Tremaine. *Galactic Dynamics: (Second Edition) (Princeton Series in Astrophysics)*. Princeton University Press, 2008. ISBN: 0691130272. URL: <http://www.amazon.com/Galactic-Dynamics-Edition-Princeton-Astrophysics/dp/0691130272>.
- [23] O. Lahav et al. "Dynamical effects of the cosmological constant". In: *Monthly Notices of the Royal Astronomical Society* 251.1 (July 1991), pp. 128–136. ISSN: 1365-2966. DOI: 10.1093/mnras/251.1.128. URL: <http://dx.doi.org/10.1093/mnras/251.1.128>.

- [24] Phillip James Edwin Peebles. *The Large-Scale Structure of the Universe*. PRINCETON UNIV PR, 1980. 440 Seiten. ISBN: 0691082405. URL: http://www.ebook.de/de/product/3637029/phillip_james_edwin_peebles_the_large_scale_structure_of_the_universe.html.
- [25] Michael A. Strauss and Jeffrey A. Willick. “The density and peculiar velocity fields of nearby galaxies”. In: *Physics Reports* 261:5-6 (Oct. 1995), pp. 271–431. ISSN: 0370-1573. DOI: 10.1016/0370-1573(95)00013-7. URL: [http://dx.doi.org/10.1016/0370-1573\(95\)00013-7](http://dx.doi.org/10.1016/0370-1573(95)00013-7).
- [26] Volker Springel. “The cosmological simulation code GADGET-2”. In: *Mon.Not.Roy.Astron.Soc.* 364 (2005), pp. 1105–1134. eprint: astro-ph/0505010. URL: <http://arxiv.org/abs/astro-ph/0505010>.
- [27] Antony Lewis. *CAMB Notes*. Apr. 2014. URL: cosmologist.info/notes/CAMB.pdf.
- [28] Uros Seljak and Matias Zaldarriaga. “A Line of Sight Approach to Cosmic Microwave Background Anisotropies”. In: *Astrophys.J.* 469:437-444,1996 (Astrophys.J.469:437-444,1996). eprint: astro-ph/9603033.
- [29] Jacob Brandbyge. “Quantitative Cosmology - Massive Neutrinos in non-linear Structure Formation”. PhD thesis. Department of Physics and Astronomy, Faculty of Science, Aarhus University, Denmark, 2010. URL: http://phys.au.dk/fileadmin/site_files/publikationer/phd/Jacob_Brandbyge.pdf.
- [30] Peter S. Behroozi, Risa H. Wechsler, and Hao-Yi Wu. “The Rockstar Phase-Space Temporal Halo Finder and the Velocity Offsets of Cluster Cores”. In: *ApJ* (2011), pp. 762, 109. eprint: 1110.4372. URL: <http://arxiv.org/pdf/1110.4372v3.pdf>.
- [31] Peter Behroozi. *The Rockstar Halo Finder*. 2011-2013.
- [32] P. A. R. Ade et al. “Planck 2013 results. XVI. Cosmological parameters”. In: *Astronomy & Astrophysics* 571 (Oct. 2014). Ed. by Jan Tauber, A16. DOI: 10.1051/0004-6361/201321591. URL: <http://dx.doi.org/10.1051/0004-6361/201321591>.
- [33] Adam G. Riess et al. “A 3% Solution: Determination of the Hubble Constant with the Hubble Space Telescope and Wide Field Camera 3”. In: *ApJ*, (2011). eprint: 1103.2976. URL: <http://arxiv.org/abs/1103.2976>.
- [34] Antony Lewis and Sarah Bridle. “Cosmological parameters from CMB and other data: A Monte Carlo approach”. In: *Phys. Rev. D* (2002). ISSN: 1089-4918. DOI: 10.1103/physrevd.66.103511. URL: <http://dx.doi.org/10.1103/PhysRevD.66.103511>.
- [35] Adam G. Riess et al. “A 2.4% Determination of the Local Value of the Hubble Constant”. In: *ApJ* 826.1 (July 2016), p. 56. DOI: 10.3847/0004-637x/826/1/56. URL: <http://dx.doi.org/10.3847/0004-637X/826/1/56>.

- [36] N. Aghanim et al. “Planck intermediate results. XLVI. Reduction of large-scale systematic effects in HFI polarization maps and estimation of the reionization optical depth”. In: *ArXiv e-prints* (May 2016). eprint: 1605.02985.
- [37] N. Aghanim et al. “Planck 2016 intermediate results. LI. Features in the cosmic microwave background temperature power spectrum and shifts in cosmological parameters”. In: *ArXiv e-prints* (Aug. 2016). eprint: 1608.02487.
- [38] Adam G. Riess et al. “A Redetermination of the Hubble Constant with the Hubble Space Telescope from a Differential Distance Ladder”. In: *Astrophys.J.* 699:539-563,2009 (May 2009). eprint: 0905.0695.
- [39] G. Efstathiou. “H0 revisited”. In: *Monthly Notices of the Royal Astronomical Society* 440.2 (Mar. 2014), pp. 1138–1152. DOI: 10.1093/mnras/stu278. URL: <http://dx.doi.org/10.1093/mnras/stu278>.
- [40] Chris Clarkson et al. “What is the distance to the CMB?” In: *J. Cosmol. Astropart. Phys.* 2014.11 (Nov. 2014), pp. 036–036. DOI: 10.1088/1475-7516/2014/11/036. URL: <http://dx.doi.org/10.1088/1475-7516/2014/11/036>.
- [41] Valerio Marra et al. “Cosmic variance and the measurement of the local Hubble parameter”. In: *Phys. Rev. Lett.* 110, (Mar. 2013), p. 241305. eprint: 1303.3121. URL: <http://arxiv.org/abs/1303.3121>.
- [42] R. Wojtak et al. “Cosmic variance of the local Hubble flow in large-scale cosmological simulations”. In: *Monthly Notices of the Royal Astronomical Society* 438.2 (Dec. 2013), pp. 1805–1812. DOI: 10.1093/mnras/stt2321. URL: <http://dx.doi.org/10.1093/mnras/stt2321>.
- [43] Troels Haugbolle et al. “The Velocity Field of the Local Universe from Measurements of Type Ia Supernovae”. In: *The Astrophysical Journal* (2007). ISSN: 1538-4357. DOI: 10.1086/513600. URL: <http://dx.doi.org/10.1086/513600>.
- [44] Yin-Zhe Ma and Jun Pan. “An estimation of local bulk flow with the maximum-likelihood method”. In: 2014, (Nov. 2013), MNRAS, 437, 1996. eprint: 1311.6888.
- [45] U. Feindt et al. “Measuring cosmic bulk flows with Type Ia Supernovae from the Nearby Supernova Factory”. In: *Cosmology of A&A* (Oct. 2013). eprint: 1310.4184.
- [46] Stephen J. Turnbull et al. “Cosmic flows in the nearby universe from Type Ia supernovae”. In: *Monthly Notices of the Royal Astronomical Society* 420.1 (Dec. 2011), pp. 447–454. DOI: 10.1111/j.1365-2966.2011.20050.x. URL: <http://dx.doi.org/10.1111/j.1365-2966.2011.20050.x>.
- [47] Tamara M. Davis et al. “The effect of peculiar velocities on supernova cosmology”. In: *ApJ* 741.1 (Oct. 2011), p. 67. DOI: 10.1088/0004-637x/741/1/67. URL: <http://dx.doi.org/10.1088/0004-637x/741/1/67>.

- [48] Anja Weyant et al. “An Unbiased Method of Modeling the Local Peculiar Velocity Field with Type Ia Supernovae”. In: *ApJ* 732.2 (Apr. 2011), p. 65. DOI: 10.1088/0004-637x/732/2/65. URL: <http://dx.doi.org/10.1088/0004-637x/732/2/65>.
- [49] K. Perrett et al. “Evolution in the Volumetric Type Ia Supernova Rate from the Supernova Legacy Survey”. In: *The Astronomical Journal* 144.2 (July 2012), p. 59. DOI: 10.1088/0004-6256/144/2/59. URL: <http://dx.doi.org/10.1088/0004-6256/144/2/59>.
- [50] Steven A. Rodney et al. “Type Ia Supernova Rate Measurements to Redshift 2.5 from CANDELS : Searching for Prompt Explosions in the Early Universe”. In: *The Astronomical Journal* 148.1 (June 2014), p. 13. DOI: 10.1088/0004-6256/148/1/13. URL: <http://dx.doi.org/10.1088/0004-6256/148/1/13>.
- [51] Malcolm Hicken et al. “CfA3: 185 Type Ia Supernova Light Curves from the CfA”. In: *Astrophys.J.* 700:331-357,2009 (Jan. 2009). DOI: 10.1088/0004-637x/700/1/331. eprint: 0901.4787.
- [52] David J. Bacon et al. “Cosmology with Doppler Lensing”. In: *MNRAS* 443 (Jan. 2014), pp. 1900–1915. DOI: 10.1093/mnras/stu1270. eprint: 1401.3694.
- [53] Stephen R. Green and Robert M. Wald. “Newtonian and Relativistic Cosmologies”. In: *Phys.Rev.D* 85:063512,2012 (Nov. 2011). DOI: 10.1103/PhysRevD.85.063512. eprint: 1111.2997.
- [54] S. M. Kocsbang and S. Hannestad. “Methods for studying the accuracy of light propagation in N-body simulations”. In: *Phys. Rev. D* 91, (Jan. 2015), p. 043508. DOI: 10.1103/PhysRevD.91.043508. eprint: 1501.01413.
- [55] S. M. Kocsbang and S. Hannestad. “Studying the precision of ray tracing techniques with Szekeres models”. In: *Phys. Rev. D* 92, (June 2015), p. 023532. DOI: 10.1103/PhysRevD.92.023532. eprint: 1506.09127.
- [56] Krzysztof Bolejko et al. “Anti-lensing: the bright side of voids”. In: *Phys. Rev. Lett.* 110, (Sept. 2012), p. 021302. DOI: 10.1103/PhysRevLett.110.021302. eprint: 1209.3142.
- [57] Camille Bonvin. “Effect of Peculiar Motion in Weak Lensing”. In: *Phys.Rev.D* 78:123530,2008 (Oct. 2008). DOI: 10.1103/PhysRevD.78.123530. eprint: 0810.0180.
- [58] Camille Bonvin, Ruth Durrer, and M. Alice Gasparini. “Fluctuations of the luminosity distance”. In: *Phys.Rev.D* 73:023523,2006 (Phys.Rev.D73:023523,2006). DOI: 10.1103/PhysRevD.73.023523. eprint: astro-ph/0511183.
- [59] Timothy Clifton and Joe Zuntz. “Hubble Diagram Dispersion From Large-Scale Structure”. In: *Mon. Not. R. Astron. Soc.* 400 (Feb. 2009), p. 2185. DOI: 10.1111/j.1365-2966.2009.15616.x. eprint: 0902.0726.

- [60] Saurabh Jha, Adam G. Riess, and Robert P. Kirshner. “Improved Distances to Type Ia Supernovae with Multicolor Light Curve Shapes: MLCS2k2”. In: *Astrophys.J.* 659:122-148,2007 (Astrophys.J.659:122-148,2007). DOI: 10.1086/512054. eprint: astro-ph/0612666.
- [61] James D. Neill, Michael J. Hudson, and Alex Conley. “The Peculiar Velocities of Local Type Ia Supernovae and Their Impact on Cosmology”. In: *The Astrophysical Journal* (2007). ISSN: 1538-4357. DOI: 10.1086/518808. URL: <http://dx.doi.org/10.1086/518808>.
- [62] Idit Zehavi et al. “A Local Hubble Bubble from Type Ia Supernovae?” In: *ApJ* 503.2 (Aug. 1998), pp. 483–491. DOI: 10.1086/306015. URL: <http://dx.doi.org/10.1086/306015>.
- [63] Ryan C. Keenan, Amy J. Barger, and Lennox L. Cowie. “Evidence for a 300 Mpc Scale Under-density in the Local Galaxy Distribution”. In: *Keenan et al.* 2013, (Apr. 2013), ApJ, 775, 62. DOI: 10.1088/0004-637X/775/1/62. eprint: 1304.2884.
- [64] M. Gregg et al. “Measuring the Hubble Flow Hubble Constant with Cepheids in the Coma Cluster”. In: *American Astronomical Society Meeting Abstracts #220*. Vol. 220. American Astronomical Society Meeting Abstracts. May 2012, p. 332.06.
- [65] L. M. Macri et al. “Cepheids in the Coma Cluster”. In: *American Astronomical Society Meeting Abstracts #221*. 2013.
- [66] Marco Baldi. “Time-dependent couplings in the dark sector: from background evolution to non-linear structure formation”. In: *Monthly Notices of the Royal Astronomical Society* (2010). ISSN: 0035-8711. DOI: 10.1111/j.1365-2966.2010.17758.x. URL: <http://dx.doi.org/10.1111/j.1365-2966.2010.17758.x>.
- [67] Marco Baldi. “The codecs project: a publicly available suite of cosmological N-body simulations for interacting dark energy models”. In: *Monthly Notices of the Royal Astronomical Society* 422.2 (Mar. 2012), pp. 1028–1044. DOI: 10.1111/j.1365-2966.2012.20675.x. URL: <http://dx.doi.org/10.1111/j.1365-2966.2012.20675.x>.
- [68] Christoph Wetterich. “The cosmological model for an asymptotically vanishing time-dependent cosmological “constant””. In: *Astron.Astrophys.* 301:321-328,1995 (Astron.Astrophys.301:321-328,1995). eprint: hep-th/9408025.
- [69] Luca Amendola. “Coupled quintessence”. In: *Phys. Rev. D* 62.4 (July 2000). ISSN: 1089-4918. DOI: 10.1103/physrevd.62.043511. URL: <http://dx.doi.org/10.1103/PhysRevD.62.043511>.
- [70] Marco Baldi. “Clarifying the effects of interacting dark energy on linear and non-linear structure formation processes”. In: *Monthly Notices of the Royal Astronomical Society* (2011). ISSN: 0035-8711. DOI: 10.1111/j.1365-2966.2011.18263.x. URL: <http://dx.doi.org/10.1111/j.1365-2966.2011.18263.x>.
- [71] L. Amendola. “Linear and nonlinear perturbations in dark energy models”. In: *prd* 69.10, 103524 (2004), p. 103524. DOI: 10.1103/PhysRevD.69.103524. eprint: astro-ph/0311175.

- [72] Luca Amendola, Marco Baldi, and Christof Wetterich. “Quintessence cosmologies with a growing matter component”. In: *Phys. Rev. D* 78.2 (July 2008). ISSN: 1550-2368. DOI: 10.1103/physrevd.78.023015. URL: <http://dx.doi.org/10.1103/PhysRevD.78.023015>.
- [73] Marco Baldi et al. “Hydrodynamical N -body simulations of coupled dark energy cosmologies”. In: *Monthly Notices of the Royal Astronomical Society* (2010). ISSN: 1365-2966. DOI: 10.1111/j.1365-2966.2009.15987.x. URL: <http://dx.doi.org/10.1111/j.1365-2966.2009.15987.x>.
- [74] Marco Baldi. “Early massive clusters and the bouncing coupled dark energy”. In: *Monthly Notices of the Royal Astronomical Society* (2011). ISSN: 0035-8711. DOI: 10.1111/j.1365-2966.2011.20048.x. URL: <http://dx.doi.org/10.1111/j.1365-2966.2011.20048.x>.
- [75] Y. B. Zel’dovich. “Gravitational instability: An approximate theory for large density perturbations.” In: *Astronomy & Astrophysics* (1970).
- [76] E. Komatsu et al. “Seven-year Wilkinson microwave anisotropy probe (WMAP) observations: Cosmological Interpretation”. In: *The Astrophysical Journal Supplement Series* 192.2 (Jan. 2011), p. 18. ISSN: 1538-4365. DOI: 10.1088/0067-0049/192/2/18. URL: <http://dx.doi.org/10.1088/0067-0049/192/2/18>.
- [77] Volker Springel et al. “Populating a cluster of galaxies - I. Results at $z=0$ ”. In: *Monthly Notices of the Royal Astronomical Society* (2001). ISSN: 1365-2966. DOI: 10.1046/j.1365-8711.2001.04912.x. URL: <http://dx.doi.org/10.1046/j.1365-8711.2001.04912.x>.
- [78] Hong Guo et al. “Redshift-Space Clustering of SDSS Galaxies — Luminosity Dependence, Halo Occupation Distribution, and Velocity Bias”. In: *Mon. Not. R. Astron. Soc.* 453.4 (Sept. 2015), pp. 4369–4384. DOI: 10.1093/mnras/stv1966. URL: <http://dx.doi.org/10.1093/mnras/stv1966>.
- [79] W. L. Freedman et al. “Final Results from the Hubble Space Telescope Key Project to Measure the Hubble Constant”. In: *ApJ* 553 (May 2001), pp. 47–72. DOI: 10.1086/320638. eprint: [astro-ph/0012376](http://arxiv.org/abs/astro-ph/0012376).
- [80] J. R. Mould et al. “The Hubble Space Telescope Key Project on the Extragalactic Distance Scale. XXVIII. Combining the Constraints on the Hubble Constant”. In: *apj* (2000). DOI: 10.1086/308304. eprint: [astro-ph/9909260](http://arxiv.org/abs/astro-ph/9909260).
- [81] Federico Marulli, Marco Baldi, and Lauro Moscardini. “Clustering and redshift-space distortions in interacting dark energy cosmologies”. In: *Mon. Not. R. Astron. Soc.* 420 (Oct. 2011). DOI: 10.1111/j.1365-2966.2011.20199.x. eprint: [1110.3045](http://arxiv.org/abs/1110.3045).
- [82] P. Coles and B. Jones. “A lognormal model for the cosmological mass distribution”. In: *mnras* (1991).
- [83] Jounghun Lee and Marco Baldi. “Can Coupled Dark Energy Speed Up the Bullet Cluster?” In: *Astrophys.J.* 747 (Oct. 2011), p. 45. DOI: 10.1088/0004-637X/747/1/45. eprint: [1110.0015](http://arxiv.org/abs/1110.0015).

- [84] Fabio Fontanot et al. “Semi-analytic galaxy formation in coupled dark energy cosmologies”. In: *Mon. Not. R. Astron. Soc.* 452.1 (July 2015), pp. 978–985. DOI: 10.1093/mnras/stv1345. URL: <http://dx.doi.org/10.1093/mnras/stv1345>.
- [85] G. La Vacca et al. “Do WMAP data favor neutrino mass and a coupling between Cold Dark Matter and Dark Energy?” In: *J. Cosmol. Astropart. Phys.* 2009.04 (Apr. 2009), pp. 007–007. ISSN: 1475-7516. DOI: 10.1088/1475-7516/2009/04/007. URL: <http://dx.doi.org/10.1088/1475-7516/2009/04/007>.
- [86] N. Sugiura, N. Sugiyama, and M. Sasaki. “Anisotropies in Luminosity Distance”. In: *Progress of Theoretical Physics* 101.4 (Apr. 1999), pp. 903–922. DOI: 10.1143/ptp.101.903. URL: <http://dx.doi.org/10.1143/PTP.101.903>.
- [87] Camille Bonvin, Ruth Durrer, and Martin Kunz. “Dipole of the Luminosity Distance: A Direct Measure of $H(z)$ ”. In: *Phys. Rev. Lett.* 96.19 (May 2006). DOI: 10.1103/physrevlett.96.191302. URL: <http://dx.doi.org/10.1103/PhysRevLett.96.191302>.
- [88] Christopher Gordon, Kate Land, and Anze Slosar. “Cosmological Constraints from Type Ia Supernovae Peculiar Velocity Measurements”. In: *Phys.Rev.Lett.* 99:081301,2007 (May 2007). DOI: 10.1103/PhysRevLett.99.081301. eprint: 0705.1718.
- [89] Steen Hannestad, Troels Haugboelle, and Bjarne Thomsen. “Precision measurements of large scale structure with future type Ia supernova surveys”. In: *JCAP* (2007). eprint: 0705.0979.
- [90] Richard Watkins and Hume A. Feldman. “Power Spectrum Shape from Peculiar Velocity Data”. In: *Mon.Not.Roy.Astron.Soc.* 379:343-348,2007 (Mon.Not.Roy.Astron.Soc.379:343-348,2007). DOI: 10.1111/j.1365-2966.2007.11970.x. eprint: astro-ph/0702751.
- [91] Vid Iršič and Anže Slosar. “Data compression of measurements of peculiar velocities of Supernovae Ia”. In: *Phys.Rev.D* 83:123501,2011 (May 2011). DOI: 10.1103/PhysRevD.83.123501. eprint: 1105.3285.
- [92] S. D. M. White and M. J. Rees. “Core condensation in heavy halos: a two-stage theory for galaxy formation and clustering”. In: *Monthly Notices of the Royal Astronomical Society* 183.3 (July 1978), pp. 341–358. DOI: 10.1093/mnras/183.3.341. URL: <http://dx.doi.org/10.1093/mnras/183.3.341>.
- [93] C M Baugh. “A primer on hierarchical galaxy formation: the semi-analytical approach”. In: *Reports on Progress in Physics* (2006). ISSN: 1361-6633. DOI: 10.1088/0034-4885/69/12/r02. URL: <http://dx.doi.org/10.1088/0034-4885/69/12/R02>.
- [94] Benjamin P. Moster et al. “Constraints on the relationship between stellar mass and halo mass at low and high redshift”. In: *The Astrophysical Journal* (2010). ISSN: 1538-4357. DOI: 10.1088/0004-637x/710/2/903. URL: <http://dx.doi.org/10.1088/0004-637X/710/2/903>.

- [95] Peter S. Behroozi et al. “Gravitationally Consistent Halo Catalogs and Merger Trees for Precision Cosmology”. In: *The Astrophysical Journal* (2012). ISSN: 1538-4357. DOI: 10.1088/0004-637x/763/1/18. URL: <http://dx.doi.org/10.1088/0004-637X/763/1/18>.
- [96] Andrew J. Benson. “Galacticus: A semi-analytic model of galaxy formation”. In: *New Astronomy* (2012). ISSN: 1384-1076. DOI: 10.1016/j.newast.2011.07.004. URL: <http://dx.doi.org/10.1016/j.newast.2011.07.004>.
- [97] Andrew Benson. *Galacticus v0.9.4 manual*.
- [98] Andrew J. Benson. “Galaxy formation theory”. In: *Physics Reports* 495.2-3 (Oct. 2010), pp. 33–86. DOI: 10.1016/j.physrep.2010.06.001. URL: <http://dx.doi.org/10.1016/j.physrep.2010.06.001>.
- [99] G. Chabrier. “The Galactic disk mass-budget : I. stellar mass-function and density”. In: *Astrophys.J.* 554:1274-1281,2001 (Astrophys.J.554:1274-1281,2001). DOI: 10.1086/321401. eprint: astro-ph/0107018.
- [100] Charlie Conroy, James E. Gunn, and Martin White. “The propagation of uncertainties in stellar population synthesis modeling. I. The relevance of uncertain aspects of stellar evolution and the initial mass function to the derived physical properties of galaxies”. In: *ApJ* 699.1 (June 2009), pp. 486–506. DOI: 10.1088/0004-637x/699/1/486. URL: <http://dx.doi.org/10.1088/0004-637X/699/1/486>.
- [101] Bradley M. Peterson Barbara Ryden. *Foundations of Astrophysics*. ADDISON WESLEY PUB CO INC, 2011. 596 Seiten. ISBN: 0321748050.
- [102] John Whelan and Jr. Iben Icko. “Binaries and Supernovae of Type I”. In: *ApJ* 186 (Dec. 1973), p. 1007. DOI: 10.1086/152565. URL: <http://dx.doi.org/10.1086/152565>.
- [103] R. F. Webbink. “Double white dwarfs as progenitors of R Coronae Borealis stars and Type I supernovae”. In: *ApJ* 277 (Feb. 1984), p. 355. DOI: 10.1086/161701. URL: <http://dx.doi.org/10.1086/161701>.
- [104] Jr. Iben I. and A. V. Tutukov. “Supernovae of type I as end products of the evolution of binaries with components of moderate initial mass (M not greater than about 9 solar masses)”. In: *ApJS* 54 (Feb. 1984), p. 335. DOI: 10.1086/190932. URL: <http://dx.doi.org/10.1086/190932>.
- [105] D. Maoz and F. Mannucci. “Type-Ia Supernova Rates and the Progenitor Problem: A Review”. In: *Publications of the Astronomical Society of Australia* 29.04 (2012), pp. 447–465. DOI: 10.1071/as11052. URL: <http://dx.doi.org/10.1071/AS11052>.
- [106] Izumi Hachisu, Mariko Kato, and Ken’ ichi Nomoto. “A Wide Symbiotic Channel to Type Ia Supernovae”. In: *ApJ* 522.1 (Sept. 1999), pp. 487–503. DOI: 10.1086/307608. URL: <http://dx.doi.org/10.1086/307608>.

- [107] James Guillochon et al. “Surface Detonations in Double Degenerate Binary Systems Triggered by Accretion Stream Instabilities”. In: *ApJ* 709.1 (Jan. 2010), pp. L64–L69. DOI: 10.1088/2041-8205/709/1/L64. URL: <http://dx.doi.org/10.1088/2041-8205/709/1/L64>.
- [108] Marten H. van Kerkwijk, Philip Chang, and Stephen Justham. “Sub-Chandrasekhar White Dwarf Mergers as the Progenitors of Type Ia Supernovae”. In: *Astroph.J. Letters* 722 (June 2010), pp. 157–161. DOI: 10.1088/2041-8205/722/2/L157. eprint: 1006.4391.
- [109] Masahiro Nagashima et al. “The metal enrichment of the intracluster medium in hierarchical galaxy formation models”. In: *Monthly Notices of the Royal Astronomical Society* (2005). ISSN: 1365-2966. DOI: 10.1111/j.1365-2966.2005.08766.x. URL: <http://dx.doi.org/10.1111/j.1365-2966.2005.08766.x>.
- [110] Evan Scannapieco and Lars Bildsten. “The Type Ia Supernova Rate”. In: *The Astrophysical Journal* (2005). ISSN: 1538-4357. DOI: 10.1086/452632. URL: <http://dx.doi.org/10.1086/452632>.
- [111] Laura Greggio. “The rates of Type Ia Supernovae. I. Analytical Formulations”. In: *Astron.Astrophys.* 441:1055-1078,2005 (Astron.Astrophys.441:1055-1078,2005). DOI: 10.1051/0004-6361:20052926. eprint: astro-ph/0504376.
- [112] A. Gal-Yam and D. Maoz. “The redshift distribution of type Ia supernovae: constraints on progenitors and cosmic star formation history”. In: *Monthly Notices of the Royal Astronomical Society* 347.3 (Jan. 2004), pp. 942–950. DOI: 10.1111/j.1365-2966.2004.07237.x. URL: <http://dx.doi.org/10.1111/j.1365-2966.2004.07237.x>.
- [113] O. Graur et al. “Supernovae in the Subaru Deep Field: the rate and delay-time distribution of Type Ia supernovae out to redshift 2”. In: *Monthly Notices of the Royal Astronomical Society* 417.2 (Sept. 2011), pp. 916–940. DOI: 10.1111/j.1365-2966.2011.19287.x. URL: <http://dx.doi.org/10.1111/j.1365-2966.2011.19287.x>.
- [114] Naoki Yasuda and Masataka Fukugita. “Luminosity Functions of Type Ia Supernovae and their Host Galaxies from the Sloan Digital Sky Survey”. In: *The Astronomical Journal* 139.1 (Nov. 2009), pp. 39–52. DOI: 10.1088/0004-6256/139/1/39. URL: <http://dx.doi.org/10.1088/0004-6256/139/1/39>.
- [115] Benjamin Dilday et al. “A Measurement of the Rate of type-Ia Supernovae at Redshift $z \approx 0.1$ from the First Season of the SDSS-II Supernova Survey”. In: *Astrophys.J.* 682:262-282,2008 (Jan. 2008). DOI: 10.1086/587733. eprint: 0801.3297.
- [116] M. Sullivan et al. “Rates and Properties of Type Ia Supernovae as a Function of Mass and Star Formation in Their Host Galaxies”. In: *The Astrophysical Journal* (2006). ISSN: 1538-4357. DOI: 10.1086/506137. URL: <http://dx.doi.org/10.1086/506137>.
- [117] LSST Science Collaboration. “LSST Science Book, Version 2.0”. In: *ArXiv e-prints* (2009). eprint: 0912.0201.
- [118] P. Schechter. “An analytic expression for the luminosity function for galaxies.” In: *ApJ* 203 (Jan. 1976), p. 297. DOI: 10.1086/154079. URL: <http://dx.doi.org/10.1086/154079>.

- [119] P. Norberg et al. “The 2dF Galaxy Redshift Survey: The b_J -band galaxy luminosity function and survey selection function”. In: *Mon.Not.Roy.Astron.Soc.* 336:907,2002 (Mon.Not.Roy.Astron.Soc.336:907,2002). DOI: 10.1046/j.1365-8711.2002.05831.x. eprint: astro-ph/0111011.
- [120] Cheng Li and Simon D. M. White. “The distribution of stellar mass in the low-redshift Universe”. In: *Monthly Notices of the Royal Astronomical Society* 398.4 (Oct. 2009), pp. 2177–2187. DOI: 10.1111/j.1365-2966.2009.15268.x. URL: <http://dx.doi.org/10.1111/j.1365-2966.2009.15268.x>.
- [121] Michael R. Blanton and Sam Roweis. “K-Corrections and Filter Transformations in the Ultraviolet, Optical, and Near-Infrared”. In: *Astron J* 133.2 (Jan. 2007), pp. 734–754. DOI: 10.1086/510127. URL: <http://dx.doi.org/10.1086/510127>.
- [122] K. M. Gorski et al. “HEALPix: A Framework for High Resolution Discretization and Fast Analysis of Data Distributed on the Sphere”. In: *The Astrophysical Journal* (2005). ISSN: 1538-4357. DOI: 10.1086/427976. URL: <http://dx.doi.org/10.1086/427976>.
- [123] Eric Hivon et al. “MASTER of the Cosmic Microwave Background Anisotropy Power Spectrum: A Fast Method for Statistical Analysis of Large and Complex Cosmic Microwave Background Data Sets”. In: *The Astrophysical Journal* (2002). ISSN: 1538-4357. DOI: 10.1086/338126. URL: <http://dx.doi.org/10.1086/338126>.
- [124] Tommaso Giannantonio et al. “Constraining primordial non-Gaussianity with future galaxy surveys”. In: *Monthly Notices of the Royal Astronomical Society* 422.4 (Apr. 2012), pp. 2854–2877. DOI: 10.1111/j.1365-2966.2012.20604.x. URL: <http://dx.doi.org/10.1111/j.1365-2966.2012.20604.x>.
- [125] Eric M. Huff et al. “Cosmic shear without shape noise”. In: *ArXiv e-prints* (Nov. 2013). eprint: 1311.1489.
- [126] R. Adam et al. “Planck 2015 results. I. Overview of products and scientific results”. In: *ArXiv e-prints* (Feb. 2015). eprint: 1502.01582.
- [127] C. Heymans et al. “CFHTLenS tomographic weak lensing cosmological parameter constraints: Mitigating the impact of intrinsic galaxy alignments”. In: *Monthly Notices of the Royal Astronomical Society* 432.3 (May 2013), pp. 2433–2453. DOI: 10.1093/mnras/stt601. URL: <http://dx.doi.org/10.1093/mnras/stt601>.
- [128] C. Hernandez-Monteagudo et al. “Correlation properties of the kinematic Sunyaev-Zel’dovich effect and implications for Dark Energy”. In: *Astrophys.J.* 643:598-615,2006 (Astrophys.J.643:598-615,2006). DOI: 10.1086/503190. eprint: astro-ph/0511061.
- [129] M. L. Brown, P. G. Castro, and A. N. Taylor. “CMB temperature and polarisation pseudo-Cl estimators and covariances”. In: *Mon.Not.Roy.Astron.Soc.* 360 (2005), pp. 1262–1280. DOI: 10.1111/j.1365-2966.2005.09111.x. eprint: astro-ph/0410394.